

NO-A190 856

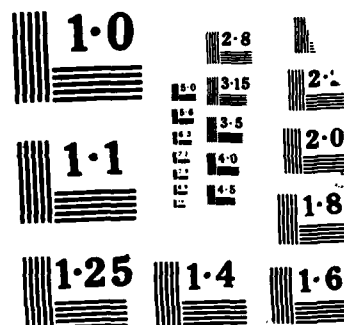
THE STRUCTURE OF SONIC UNDEREXPANDED TURBULENT AIR JETS 1/2
IN STILL AIR(U) MICHIGAN UNIV ANN ARBOR DEPT OF
AEROSPACE ENGINEERING S G CHUECH ET AL. SEP 87

UNCLASSIFIED

NO0014-85-K-0604

F/G 20/4

44



**THE STRUCTURE OF SONIC UNDEREXPANDED
TURBULENT AIR JETS IN STILL AIR**

by

S. G. Chuech, M.-C. Lai and G. M. Faeth
Department of Aerospace Engineering
The University of Michigan
Ann Arbor, Michigan 48109-2140

Interim Report

Grant No. N00014-85-K-0604
Office of Naval Research
800 North Quincy Street
Arlington, Virginia 22217



October 1987

Accession For		
NTIS GRA&I	<input checked="checked" type="checkbox"/>	
DTIC TAB	<input type="checkbox"/>	
Unannounced	<input type="checkbox"/>	
Justification		
By		
Distribution/		
Availability Codes		
and/or		
Special		
A-1		

Unclassified

SECURITY CLASSIFICATION OF THIS PAGE

REPORT DOCUMENTATION PAGE

Form Approved
OMB No. 0704-0188

1a. REPORT SECURITY CLASSIFICATION Unclassified			1b. RESTRICTIVE MARKINGS		
2a. SECURITY CLASSIFICATION AUTHORITY			3. DISTRIBUTION/AVAILABILITY OF REPORT Approved for public release; distribution is unlimited.		
2b. DECLASSIFICATION/DOWNGRADING SCHEDULE			5. MONITORING ORGANIZATION REPORT NUMBER(S)		
4. PERFORMING ORGANIZATION REPORT NUMBER(S)			7a. NAME OF MONITORING ORGANIZATION Office of Naval Research		
6a. NAME OF PERFORMING ORGANIZATION The University of Michigan		6b. OFFICE SYMBOL (if applicable)	7b. ADDRESS (City, State, and ZIP Code) 800 North Quincy Street Arlington, Virginia 22217		
6c. ADDRESS (City, State, and ZIP Code) Department of Aerospace Engineering Ann Arbor, MI 48109-2140			9. PROCUREMENT INSTRUMENT IDENTIFICATION NUMBER		
8a. NAME OF FUNDING/SPONSORING ORGANIZATION		8b. OFFICE SYMBOL (if applicable)	10. SOURCE OF FUNDING NUMBERS		
8c. ADDRESS (City, State, and ZIP Code)		PROGRAM ELEMENT NO.	PROJECT NO.	TASK NO.	WORK UNIT ACCESSION NO.
11. TITLE (Include Security Classification) (U) The Structure of Sonic Underexpanded Turbulent Air Jets in Still Air					
12. PERSONAL AUTHOR(S) S. G. Chuech, M.-C. Lai and G. M. Faeth					
13a. TYPE OF REPORT Interim Report		13b. TIME COVERED FROM 7/15/85 TO 8/15/87		14. DATE OF REPORT (Year, Month, Day) September, 1987	
				15. PAGE COUNT 105 + xii	
16. SUPPLEMENTARY NOTATION					
17. COSATI CODES			18. SUBJECT TERMS (Continue on reverse if necessary and identify by block number)		
FIELD	GROUP	SUB-GROUP	Underexpanded jets; Compressible flow; Turbulence		
			Turbulent jets; Laser-induced fluorescence; modeling		
19. ABSTRACT (Continue on reverse if necessary and identify by block number)					
<p>Turbulent subsonic, sonic and underexpanded round air jets, in still air, were studied both theoretically and experimentally. The following measurements were made: shock-wave structure of the underexpanded jets, using flash and continuous Schlieren photography; mean and fluctuating concentrations and mean static pressures, using laser-induced fluorescence; and mean and fluctuating streamwise velocities, using laser-Doppler anemometry. Analysis included: solution of the parabolized Navier-Stokes equations of motion; and use of effective adapted-jet exit conditions, to avoid the complexities of treating the shock-containing near field region of underexpanded jets. In both cases, turbulence properties were found using a k-ϵ turbulence model.</p> <p>The structure of the near-field region of the underexpanded jets was influenced by compressibility and turbulence levels at the jet exit. Mixing rates were reduced by compressibility when convective Mach numbers were greater than 0.5, in agreement with observations of</p>					
20. DISTRIBUTION/AVAILABILITY OF ABSTRACT <input checked="" type="checkbox"/> UNCLASSIFIED/UNLIMITED <input checked="" type="checkbox"/> SAME AS RPT <input type="checkbox"/> DTIC USERS			21. ABSTRACT SECURITY CLASSIFICATION Unclassified		
22a. NAME OF RESPONSIBLE INDIVIDUAL			22b. TELEPHONE (Include Area Code)		22c. OFFICE SYMBOL

Papamoschou and Roshko (1986); while increased turbulence levels at the jet exit increased mixing rates, which is a well-recognized effect for subsonic jets. The present parabolized Navier-Stokes method was successful for treating slug-flow exit conditions, but must be extended to treat effects of turbulent jet exit conditions. The effective adapted-jet approach was capable of treating various jet exit conditions; however, this approach provides no information concerning the shock-containing near-field region.

TABLE OF CONTENTS

	<u>Page</u>
ABSTRACT	ii
LIST OF TABLES	v
LIST OF FIGURES	vi
NOMENCLATURE	ix
ACKNOWLEDGEMENTS	xii
 1. INTRODUCTION	 1
1.1 General Introduction	1
1.2 Related Studies	14
1.3 Specific Objectives	18
 2. EXPERIMENTAL METHODS	 19
2.1 Apparatus	19
2.2 Instrumentation	22
2.3 Test Conditions	37
 3. THEORETICAL METHODS: ADAPTED JETS	 41
3.1 Description of Analysis	41
3.2 Governing Equations	45
3.3 Scalar Properties	49
3.4 Boundary and Initial Conditions	50
3.5 Numerical Computations	51
 4. THEORETICAL METHODS: UNDEREXPANDED JETS	 51
4.1 Parabolized Navier-Stokes Method	51
4.2 Approximate Methods	54
 5. RESULTS AND DISCUSSION	 58
5.1 Subsonic Jets	58
5.2 Sonic Jet	67
5.3 Supersonic Jets: Slug Flow	74
5.4 Underexpanded Jets: Fully-Developed Flow	79
 6. CONCLUSIONS	 94
REFERENCES	95

LIST OF TABLES

<u>Table</u>		<u>Page</u>
1	Summary of LDA Components	24
2	Summary of LIF Components	28
3	Test Conditions for Flow Visualization	39
4	Test Conditions for Structure Measurements	40
5	Test Conditions for Related Measurements	42
6	Summary of Parameters in Governing Equations	47

LIST OF FIGURES

<u>Figure</u>	<u>Caption</u>	<u>Page</u>
1	Pressure distribution in a converging nozzle for adapted and underexpanded flows.	2
2	Schematic of near-field region of a slightly underexpanded turbulent sonic jet.	4
3	Typical continuous Schlieren photograph of near-field region of a slightly underexpanded jet (underexpansion ratio of 1.64).	5
4	Typical spark Schlieren photograph of near-field region of a slightly underexpanded jet (underexpansion ratio of 1.64).	6
5	Sketch of near-field, transition, and far-field regions of a slightly underexpanded turbulent sonic jet.	7
6	Typical continuous Schlieren photograph of the whole flow field of a slightly underexpanded jet (underexpansion ratio of 1.64).	9
7	Schematic of near-field region of a highly underexpanded turbulent sonic jet.	10
8	Typical continuous Schlieren photograph of near-field region of a highly underexpanded jet (underexpansion ratio of 4.20).	11
9	Typical spark Schlieren photograph of near-field region of a highly underexpanded jet (underexpansion ratio of 4.20).	12
10	Typical continuous Schlieren photograph of the whole flow field of a highly underexpanded jet (underexpansion ratio of 2.58).	13
11	Sketch of the nozzle and traversing system.	20
12	Sketch of the LDA system.	23
13	Sketch of the LIF system.	27
14	Original and filtered LIF spectrum: from Lai and Faeth (1987).	32
15	Calibration of LIF intensity with mixture fraction.	34

<u>Figure</u>	<u>Caption</u>	<u>Page</u>
16	Power spectral density of mixing concentration fluctuations at the centerline of a subsonic jet.	36
17	Calibration of LIF intensity with pressure.	38
18	Turbulent mixing rates for constant-pressure mixing layers as a function of convective Mach number.	48
19	A typical example of the coflow effect on solutions of the SCIPVIS program.	55
20	Schematic of equivalent divergent-nozzle expansion of an underexpanded jet.	57
21	The initial conditions for the subsonic jet: radial profiles of mean and fluctuating quantities at $x/d = 0.2$.	60
22	Axial variation of mean and fluctuating quantities in the subsonic jet.	61
23	Radial variation of mean and fluctuating quantities in the subsonic jet at $x/d = 5$.	64
24	Radial variation of mean and fluctuating quantities in the subsonic jet at $x/d = 10$.	65
25	Radial variation of mean and fluctuating quantities in the subsonic jet at $x/d = 20$.	66
26	The initial conditions for the sonic jet: radial profiles of mean and fluctuating quantities at $x/d = 0.2$.	68
27	Axial variation of mean and fluctuating quantities in the sonic jet.	69
28	Radial variation of mean and fluctuating quantities in the sonic jet at $x/d = 5$.	71
29	Radial variation of mean and fluctuating quantities in the sonic jet at $x/d = 10$.	72
30	Radial variation of mean and fluctuating quantities in the sonic jet at $x/d = 20$.	73

<u>Figure</u>	<u>Caption</u>	<u>Page</u>
31	Axial variation of mean velocities and concentrations in underexpanded gas jets ($p_e/p_\infty = 1.9$, $M_e = 1.0$).	75
32	Axial variation of mean static pressures in the underexpanded jet ($p_e/p_\infty = 1.45$, $M_e = 2.0$).	77
33	Axial variation of mean velocities in an adapted supersonic jet ($p_e/p_\infty = 1.0$, $M_e = 2.2$).	78
34	The initial conditions for the underexpanded jet: radial profiles of mean and fluctuating velocities at $x/d = 0.2$.	80
35	Continuous Schlieren photograph of near-field region of an underexpanded jet (underexpansion ratio of 1.2).	81
36	Continuous Schlieren photograph of near-field region of an underexpanded jet (underexpansion ratio of 1.4).	83
37	Axial variation of mean static pressures in adapted and underexpanded jets.	84
38	Axial variation of mean and fluctuating quantities in the underexpanded jets.	86
39	Radial variation of mean and fluctuating velocities in the underexpanded jet at $x/d = 5$.	88
40	Radial variation of mean and fluctuating quantities in the underexpanded jet at $x/d = 10$.	89
41	Radial variation of mean and fluctuating quantities in the underexpanded jet at $x/d = 20$.	90
42	Mach disk diameters and locations for sonic underexpanded jets.	91
43	Shock-cell wavelength for sonic underexpanded jets.	93

NOMENCLATURE

<u>Symbol</u>	<u>Description</u>
a	acceleration of gravity
C_i	constants in turbulence model
C_p	specific heat at constant pressure
d	jet exit diameter
d_{eq}	equivalent jet exit diameter
D	Mach disk diameter
f	mixture fraction
Fr	Froude number
g	square of mixture fraction fluctuations
H	stagnation enthalpy
K	turbulence kinetic energy
$K(M_c)$	compressibility correction
$K(T)$	temperature-dependent part of LIF output
L	standoff distance of Mach disk
M	Mach number
M_c	convective Mach number
N_i	number density of species i
p	pressure
Pr	Prandtl number

r	radial distance
r_{∞}	edge of flow
R	universal gas constant
Re	injector Reynolds number
S	average shock spacing
Sc	Schmidt number
S_{ϕ}	source term
T	temperature
u	axial velocity
v	radial velocity
w	initial diameter of barrel shock
W_i, W	species and mixture molecular weights
x	axial distance from injector exit plane
Y_i	mass fraction of species i
γ	specific heat ratio
ϵ	rate of dissipation of turbulence kinetic energy
$\mu_{eff, \phi}$	effective turbulent transport coefficient
μ_t	turbulent viscosity
ν	frequency, kinematic viscosity
ρ	density
σ_i	turbulent Prandtl/Schmidt number

ϕ generic property

Subscripts

c centerline value

e jet exit condition

eq equivalent jet exit condition

o stagnation condition

∞ ambient condition

Superscripts

* choked condition

$(\bar{}),(\bar{})'$ time-averaged mean and root-mean-squared fluctuating quantity

$()'$ fluctuation with respect to time average

ACKNOWLEDGEMENTS

The authors would like to thank T.-Y. Sun for his help during the early stages of the research, and S. Bauerle for preparing the manuscript. C. Iott, of the Gas Dynamics Laboratories of the University of Michigan provided valuable assistance with flow visualization during this study. Thanks are also due to R. G. Wilmoth, NASA Langley Research Center, for providing the SCIPVIS program for the analysis of underexpanded jets, and for helpful discussions concerning its use.

The financial support of the Office of Naval Research, Grant Number N00014-85-K-0148, under the Technical Management of M. K. Ellingsworth, and N00014-85-K-0604, under the Technical Management of G. D. Roy, R. S. Miller and L. A. Parnell, is also gratefully acknowledged.

INTRODUCTION

1.1 General Introduction

There are three fundamental steady-flow regimes when a compressible gas is discharged from a passage into a region having a given pressure, as follows: (1) adapted jets, where the passage exit and ambient pressures are the same; (2) nonadapted underexpanded jets, where the passage exit pressure is higher than the ambient pressure; and (3) nonadapted overexpanded jets, where passage exit pressures are lower than the ambient pressure (Shapiro, 1954). The nonadapted steady flows only occur when the Mach number at the passage exit is sonic or supersonic, so that the pressure disturbances from the ambient region cannot propagate into the passage to equalize the passage exit and ambient pressures. Instead, pressure equalization is achieved in a multidimensional external expansion or compression region near the passage exit, which involves supersonic velocities and the appearance of shock and expansion waves. The objective of this investigation was to complete an experimental study of the structure and mixing properties of one class of turbulent nonadapted jets, namely: underexpanded free jets in a still environment, where the flow is sonic at the passage exit. Underexpanded jets of this type can be produced by compressible flows in converging nozzles or constant-area passages (Shapiro, 1954). Predictions were also undertaken, both to assist interpretation of the measurements and to initiate evaluation of methods for analyzing the process.

Sonic underexpanded free jets appear in a number of practical applications, e.g., combustion in SCRAMJET engines, gas-mixing systems in the process industries, oil-well blowouts, and breaks in high-pressure systems, among others. In addition, sonic underexpanded jets are often used for processes involving the injection of gases into liquids, to achieve stable injector operation (Chen and Faeth, 1982, 1983). Information concerning underexpanded gas jets in gases is needed to gain a better understanding of the structure and mixing properties of these important multiphase flows, and the mechanism by which underexpansion stabilizes the flow.

The general behavior of sonic underexpanded free jets can be pictured as the flow between two large reservoirs. This process is sketched in Fig. 1, following Shapiro (1954). In order to simplify the discussion, the connecting passage is taken to be a converging, frictionless nozzle. Static pressures along the axis of the flow are plotted for various pressures in the upstream reservoir, p_0 , with a constant pressure p_∞ , in the downstream reservoir. In all cases, the flow accelerates as the pressure drops in the passage, with the maximum velocity and Mach number within the passage reached at its exit. When the pressure difference between the two reservoirs is small, the velocity at the exit of the passage is subsonic and the pressure at the passage exit is equal to the ambient pressure, yielding an adapted jet. As the upstream pressure is increased, velocities and Mach numbers at the passage exit increase, eventually reaching sonic velocity, yielding a sonic adapted jet (the upstream reservoir pressure at this

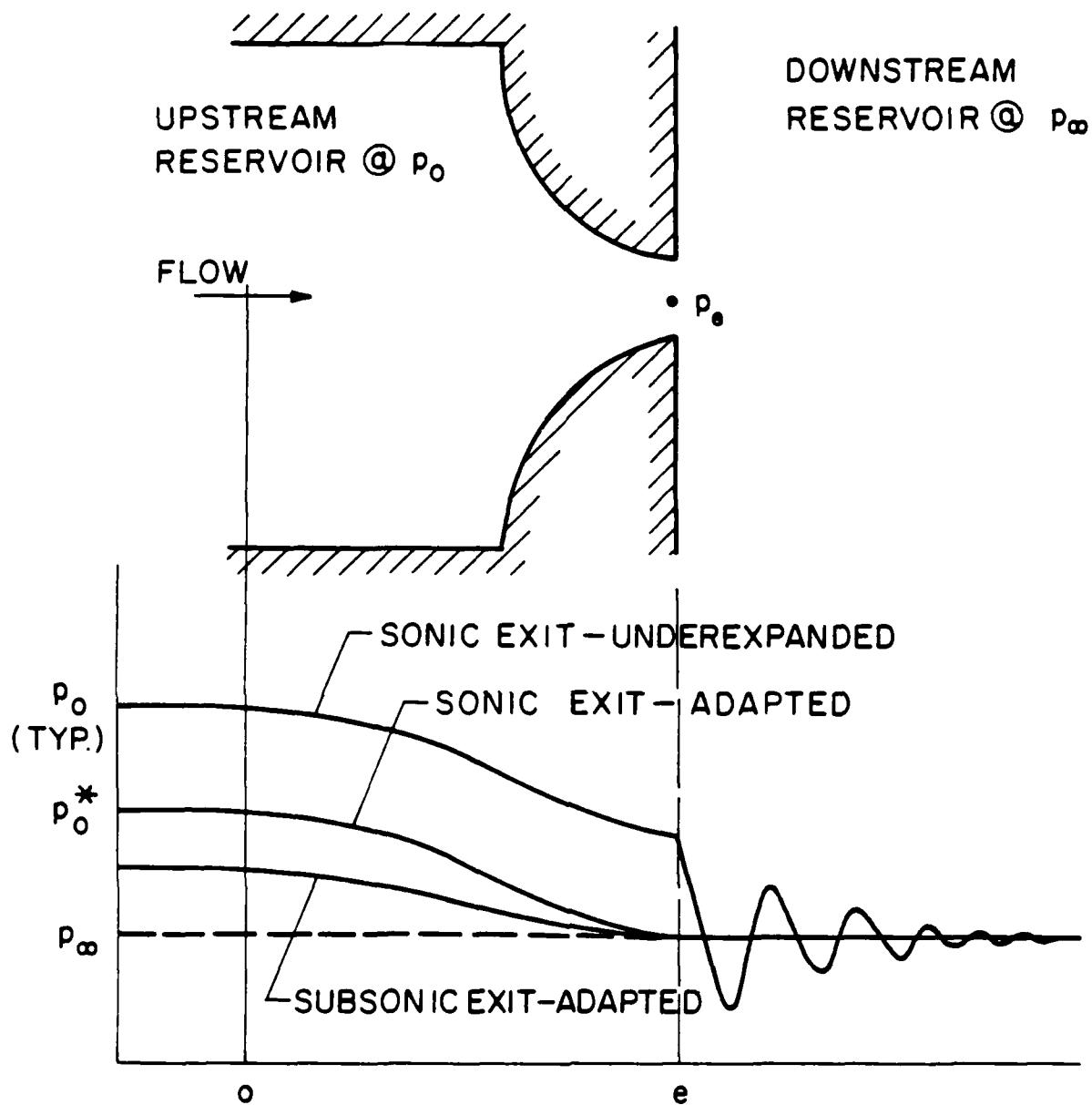


Fig. 1 Pressure distribution in a converging nozzle for adapted and underexpanded flows.

condition is denoted p_o^* in Fig. 1). When the upstream reservoir pressure is increased beyond p_o^* , the flow remains sonic at the passage exit. However, pressure disturbances cannot propagate upstream in a sonic flow; therefore, the pressure at the passage exit, p_e , increases above the pressure in the downstream reservoir, since the pressure ratio, p_e/p_o , needed to achieve sonic conditions for frictionless flow is a constant (Shapiro, 1954). This yields an underexpanded sonic jet at the passage exit: the ambient pressure is finally reached through an external expansion process which involves pressure fluctuations along the axis, roughly as sketched in Fig. 1.

The nature of the external expansion process near the passage exit is illustrated in Fig. 2. The external expansion region is sketched in the figure, assuming a slightly underexpanded sonic jet with a uniform flow at the passage exit. Expansion to the ambient pressure is initiated by a Prandtl-Meyer expansion fan, centered at the periphery of the passage exit. As the pressure drops in the expansion fan, the flow accelerates and becomes supersonic. The expansion waves reflect from the constant-pressure boundary of the flow as compression waves (not shown in Fig. 2) which steepen and intersect to form an intercepting shock. The intercepting shock propagates toward the centerline, where it is reflected as an oblique shock. The pressure behind the oblique shock is higher than the ambient pressure, similar to conditions at the jet exit; therefore, another expansion fan is formed when the reflected shock reaches the edge of the flow, leading to additional shock structures (shock cells), qualitatively similar to the first (Adamson and Nicholls, 1959). Near the edge of the flow, however, a jet mixing layer develops, where the flow finally adjusts to the still ambient environment. Growth of this viscous mixing layer constricts and weakens the shock-cell pattern, causing it to disappear when the sonic line within the mixing layer reaches the axis. The alternate intersection of expansion and shock waves at the axis, in conjunction with the growing mixing layer, causes the decaying oscillatory pressure variation sketched in Fig. 1.

The features of slightly underexpanded sonic jets can be seen in the Schlieren photographs appearing in Figs. 3 and 4. These photographs were obtained during the present investigation for sonic flow at the jet exit and an underexpansion ratio (defined as p_e/p_∞) of 1.64. Figure 3 is a continuous Schlieren photograph which highlights the shock-wave structure of the flow. The repetitive shock-cell pattern near the jet exit can be seen as well as the progressive reduction in the dimensions of the shock cells with increasing distance from the injector. Figure 4 is a short-duration (ca. 0.1 μ s) spark Schlieren photograph, which highlights the development of the mixing layer (the turbulent mixing layer appears as a mottled area due to density fluctuations). The shock cell structure, however, can still be seen on the photograph.

Figure 5 is a sketch of the entire flow field near the exit of a slightly underexpanded sonic free jet. Similar to Fig. 2, the flow at the exit of the passage is assumed to be uniform,

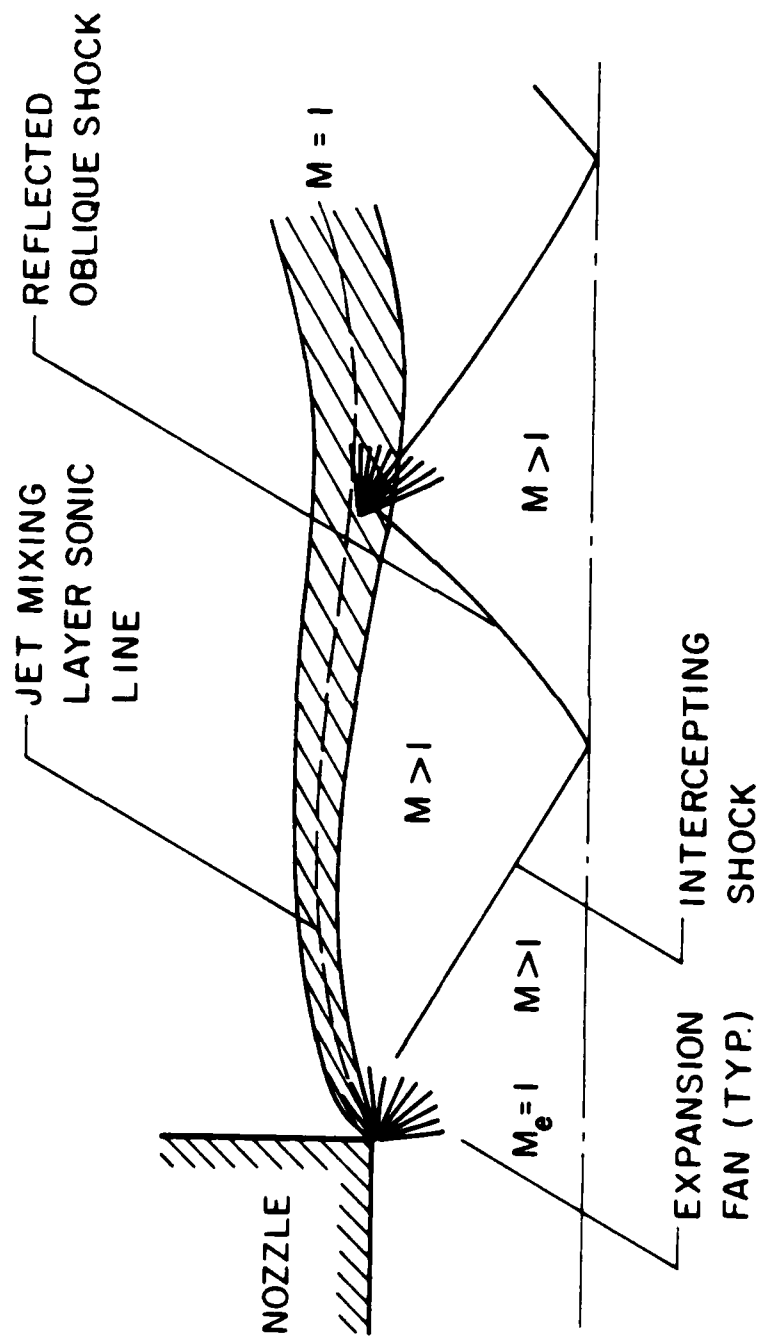


Fig. 2 Schematic of near-field region of a slightly underexpanded turbulent sonic jet.



Fig. 3 Typical continuous Schlieren photograph of near-field region of a slightly underexpanded jet (underexpansion ratio of 1.64).

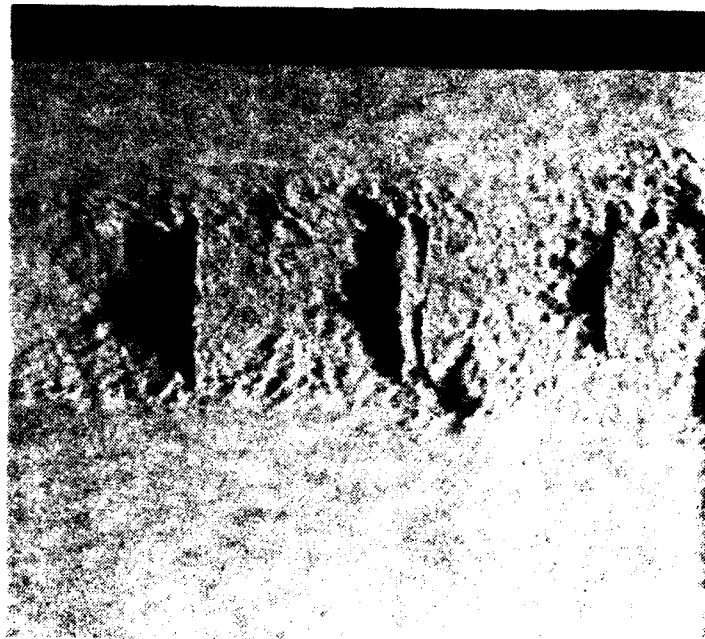


Fig. 4 Typical spark Schlieren photograph of near-field region of a slightly underexpanded jet (underexpansion ratio of 1.64).

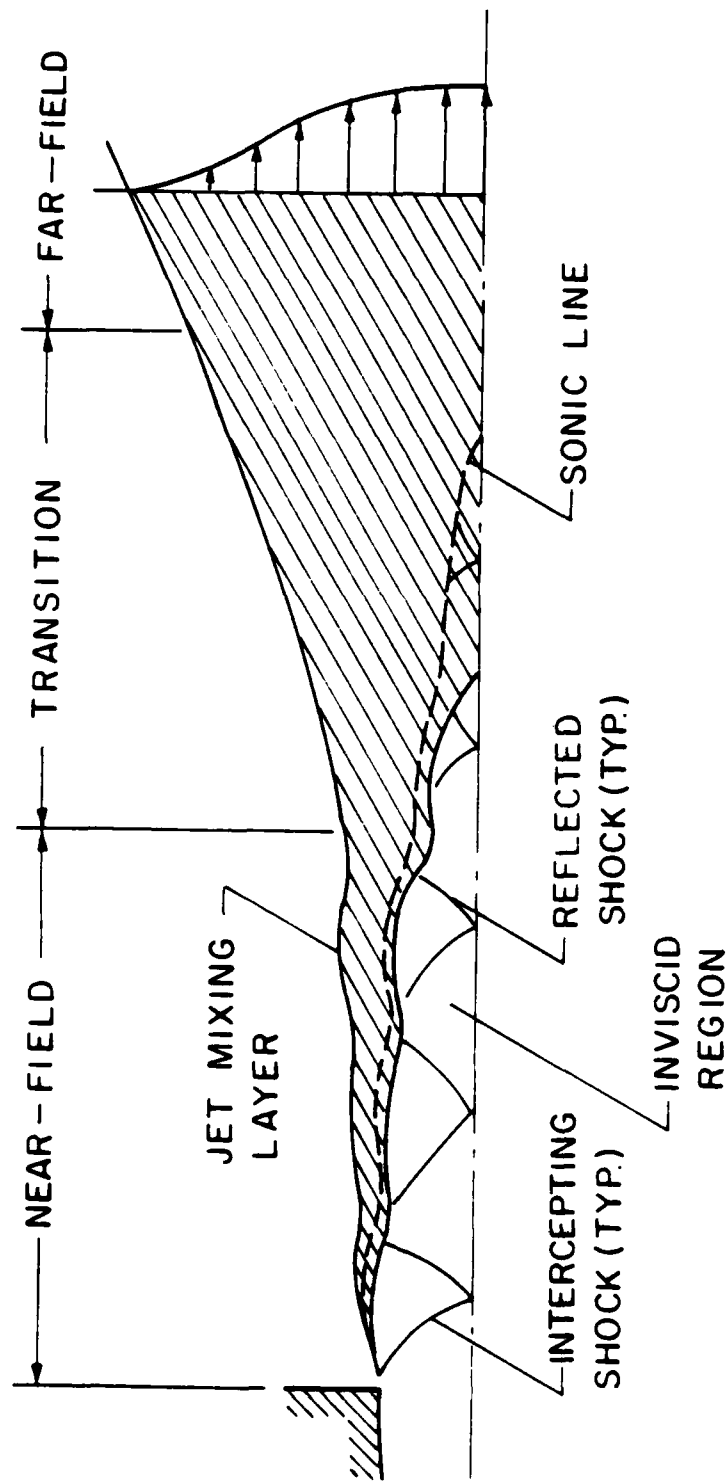


Fig. 5 Sketch of near-field, transition, and far-field regions of a slightly under-expanded turbulent sonic jet.

yielding a shock-containing inviscid region, where static pressures vary near the core of the flow. This region is surrounded by the growing mixing layer which contains the sonic line. Once the sonic line reaches the axis, the flow becomes a subsonic free jet having nearly constant static pressures. The various processes in this flow can be broken down into three regions (Dash and Wolf, 1984), as follows: the near-field region, where inviscid shock cells dominate the flow; the transition region, where viscous processes become more important as the flow at the axis passes through the sonic velocity; and the far-field region, which is a conventional subsonic, constant-pressure mixing process. This evolution of the shock-wave pattern can be seen in the continuous Schlieren photograph appearing in Fig. 6. This photograph was obtained for the same conditions as Figs. 3 and 4, e.g., a sonic jet with an underexpansion ratio of 1.64. In this case, several shock cells can be seen in the near-field region.

When the underexpansion ratio increases, the strength of the shock waves in the near-field region increase as well. Eventually, a condition is reached where normal shock waves (called Mach disks) appear in the flow field as pictured in Fig. 7. The Mach disks appear since they provide the only mechanism which can sustain the higher pressure ratios needed to match the ambient pressure when the reflected shock reaches the edge of the flow (Abbett, 1971; Adamson and Nicholls, 1959; Crist et al., 1966). The intercepting shock, the Mach disk, and the reflected shock all meet at a triple point. The flow behind the Mach disk is subsonic, while the flow behind the reflected shock is supersonic. Between these two regions a second mixing layer forms (the Mach disk mixing layer) which originates from the triple point (Dash and Wolf, 1984). Similar to conditions where Mach disks do not appear, the reflected shock reaches the edge of the flow where it is reflected as an expansion fan to repeat the process again. Viscous effects in the jet and Mach disk mixing layers cause the wave pattern to weaken, passing through a regime where only oblique shocks are observed to finally a subsonic constant-pressure jet, similar to the flow pictured in Fig. 5.

The structure and evolution of the flow for a highly underexpanded sonic jet can be seen in the Schlieren photographs appearing in Figs. 8-10. These photographs were obtained during the present investigation: Figs. 8 and 9 are continuous and spark Schlieren photographs of the near-field region of a jet having an underexpansion ratio of 4.20; and Fig. 10 is a continuous Schlieren photograph of the entire shock-containing region for an underexpansion ratio of 2.58. In all these cases, a Mach disk is present in the first shock cell, while the remaining shock cells only contain oblique shock waves. The spark Schlieren photograph of Fig. 9 shows the development of the jet mixing layer, for highly underexpanded jets, similar to Fig. 4 for slightly underexpanded jets. The Mach-disk shear layer, however, is obscured since it is surrounded by the jet mixing layer for the present axisymmetric flows.

It is clear that sonic underexpanded free jets involve a rich variety of fluid flow processes. Of particular interest is the interaction between turbulence in the mixing layers and the shock wave pattern, since this interaction controls the extent of the shock-containing



Fig. 6 Typical continuous Schlieren photograph of the whole flow field of a slightly underexpanded jet (underexpansion ratio of 1.64).

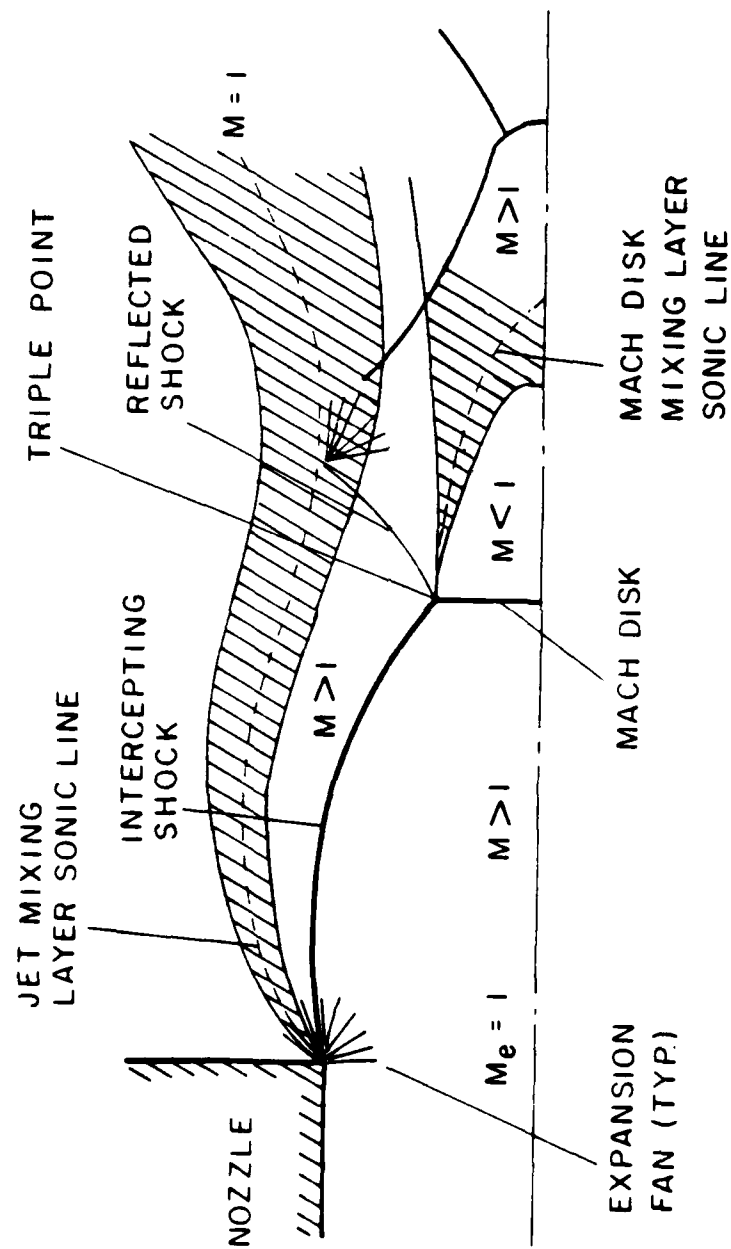


Fig. 7 Schematic of near-field region of a highly underexpanded turbulent sonic jet.

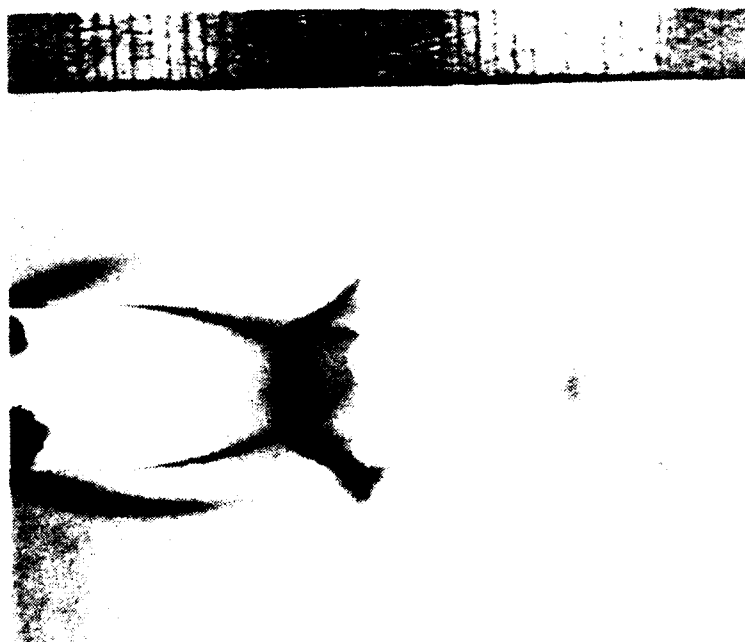


Fig. 8 Typical continuous Schlieren photograph of near-field region of a highly underexpanded jet (underexpansion ratio of 4.20).



Fig. 9 Typical spark Schlieren photograph of near-field region of a highly underexpanded jet (underexpansion ratio of 4.20).

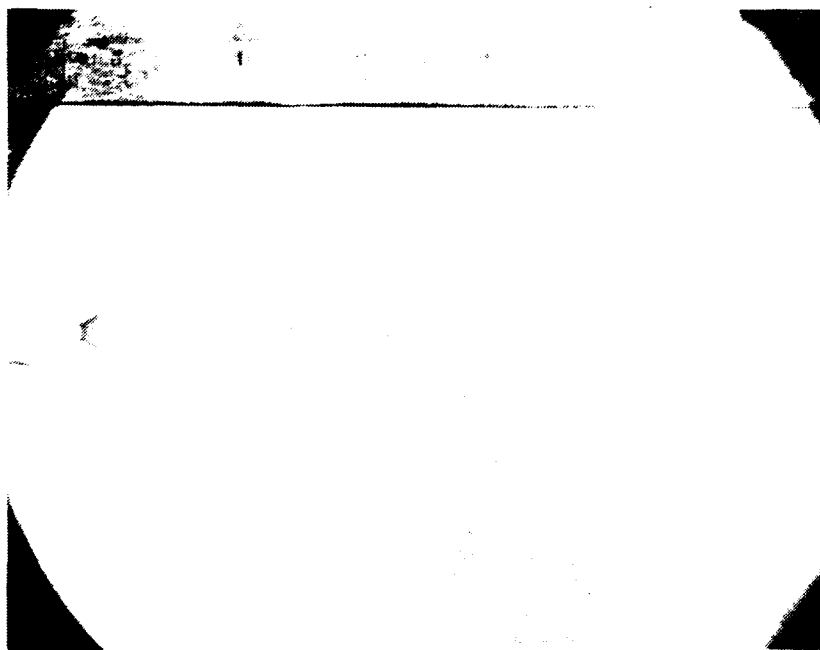


Fig. 10 Typical continuous Schlieren photograph of the whole flow field of a highly underexpanded jet (underexpansion ratio of 2.58).

portion of the flow. The objective of the present investigation was to examine this shock-wave containing near-field region of sonic underexpanded jets both theoretically and experimentally. The near-field region of subsonic and sonic adapted jets was also examined, in order to provide baselines for predictions and measurements of the underexpanded jets.

1.2 Related Studies

Past studies related to underexpanded turbulent jets will be briefly discussed in the following. Subsonic and supersonic jets will be considered in turn: the former since they provide a baseline for studying effects of variable density phenomena in turbulent flows, while minimizing effects of compressibility; the latter since they are directly related to the objectives and methods of the present investigation.

Subsonic Jets. Numerous theoretical and experimental studies of subsonic jets have been reported, see Hinze (1975), Schlichting (1979) and Wygnanski and Fiedler (1969) for reviews of early work in the field.

Initial measurements of velocities in turbulent supersonic jets used pitot probes and hot wires; for example, Corrsin and Uberoi (1951), Wygnanski and Fiedler (1969), Ribeiro and Whitelaw (1974) and Antonia et al. (1975). These measurements demonstrated that velocity distributions exhibit self-similarity a few diameters downstream of the jet exit. More recently, the nonintrusive laser Doppler anemometer (LDA) has been used to measure velocities in adapted jets; for example, Kotsovinos (1975), Shaughnessy and Morton (1977) and Lau et al. (1979). Kotsovinos (1979) and Lau et al. (1979) showed that probability density functions of velocity near the edge of jets in still environments exhibit negative velocities a significant fraction of the time. This implies errors in earlier probe measurements, due to their inability to resolve directional ambiguity.

The scalar field produced by adapted jets has also received attention. Initial measurements used probes and have been reviewed by Long (1963) and Field et al. (1967). Corrsin and Uberoi (1950, 1951) report early measurements of mean and fluctuating temperatures in heated round jets, using hot-wire probes. One of the most comprehensive studies of scalar mixing using hot wires is that of Antonia et al. (1975), where higher moments of velocity and temperature fluctuations, and their cross-correlations, were measured.

Rosensweig et al. (1961) and Becker et al. (1967) completed early studies of scalar mixing in turbulent jets, using Mie scattering from seeding particles in the jet flow. This technique is easy to implement since Mie scattering signals are strong, allowing use of incoherent light sources, but the method has deficiencies due to excessive shot noise resulting from limitations in feasible levels of seeding densities. Once lasers became available, interest shifted from particle (Mie) scattering to molecular scattering techniques, where the large number of molecules within even a very small optical measuring volume very much reduces

problems of shot noise. Popular laser scattering methods include: Rayleigh scattering (Graham et al., 1974; Dyer, 1979; Yee et al., 1983; Escoda and Long, 1983; Pitts and Kashiwagi, 1984; and Schefer and Dibble, 1986); and Raman scattering (Smith and Giedt, 1974; Lapp, 1974; Robben, 1975; Birch et al., 1978; and Drake et al., 1981).

There have also been numerous theoretical studies of subsonic jets. Early work concentrated on similarity-type correlations, integral models and mixing-length models (Birch et al., 1978, 1984; Forstall and Shapiro, 1950; and Hinze, 1975). Beginning with Rodi (1972), Launder et al. (1971) and Lockwood and Naguib (1975), recent interest has turned to the use of higher-order turbulence closures for the high-Reynolds number jets encountered in most practical applications. Initially, difficulties were encountered in establishing empirical aspects of these closures, since the important effects of initial conditions at the jet exit were not immediately recognized. Effects of variable-density jets were also problematical, but later use of mass-weighted Favre-averaged quantities has yielded methods which are reasonably effective when Mach numbers are low and the Reynolds number is high (Bilger, 1976). In this laboratory, numerous evaluations of predictions and measurements in low-speed, high Reynolds number, round jets have been reported, which have established reasonably reliable methods for finding mean properties in constant and variable density jets when initial conditions are properly known (Chen and Faeth, 1982, 1983; Jeng and Faeth, 1984; Shuen et al., 1984; and Sun and Faeth, 1986). Major uncertainties, at this time, relate to turbulence quantities and improvements in the physical basis of higher-order turbulence closures – even for simple free jet flows. Another limitation is that past work has not considered high-speed supersonic flows, where effects of the kinetic energy of the flow must be considered.

Supersonic Jets. Supersonic adapted and underexpanded jets have received far less attention than subsonic jets. The reason for this is that the varying static pressure field, the high velocities, and the presence of shock waves cause significant measurement difficulties. The absence of data needed to evaluate predictions has also limited the development of theory for these flows.

Early studies of underexpanded jets focussed on the properties of the Mach disk (Adamson and Nicholls, 1959; Lewis and Carlson, 1964; Crist et al., 1966; and Davidor and Penner, 1971). These studies generally used shadowgraph and Schlieren techniques to measure Mach disk size and position and inviscid analysis to estimate these properties: achieving some success for nozzle flows. More recently, Addy (1981) used shadowgraphs to find the size and location of the Mach disks – observing significant effects of nozzle geometry (all having small length-to-diameter ratios) which he attributes to variations in the position of the sonic line at the jet exit.

Early measurements of the structure of underexpanded and supersonic jets are reviewed by Eggers (1966) and Birch and Eggers (1973). This generally involved the use of probes, particularly for measurements of mean quantities along the axis of the flow. More recent probe

measurements of static pressure distributions along the axis of underexpanded jets have been reported in conjunction with shock noise studies by Seiner and Norum (1979, 1980). Most of these measurements were limited to convergent/divergent nozzle configurations.

Several nonintrusive techniques have been applied for measurements of velocities in supersonic gas jets; however, most studies reported thus far have concentrated on the development of instruments and the current velocity data base for these flows is limited. Huffaker et al. (1969) discussed the selection of LDA tracers for supersonic flows, pointing out potential problems of achieving good particle response and adequate signal-to-noise ratios which have plagued most subsequent workers. For example, Flack and Thompson (1977), Lau and coworkers (1979, 1980, 1981), Ewan and Moodie (1986) and Birch et al. (1987), either avoided the supersonic portion of the flow entirely, or only reported a few points along the flow axis as part of an empirical correlation scheme (Birch et al., 1987).

Use of laser scattering from molecules provides a means of eliminating problems of the limited response of particles. Gustafson (1981) has showed that coherent anti-Stokes Raman scattering (CARS) can be used to measure velocities in supersonic flows, by observing the Doppler shift of the CARS spectra, similar to methods based on emission spectra which are widely used in astronomy. The high cost of CARS systems, however, precludes widespread use of this technique. Laser-induced fluorescence (LIF) offers a less expensive alternative whose feasibility appears to be promising based on studies of subsonic gas flows (Hiller et al., 1983) and supersonic jets (McDaniel et al., 1983; McDaniel, 1981a, Hiller et al., 1986).

Turning to scalar properties, density, pressure, temperature, and species concentrations are of interest. McDaniel et al. (1982) proposed the use of off-resonance laser-induced fluorescence (ORLIF) for density measurements. However, ORLIF is not very desirable for measurements of compressible flows at atmospheric pressure, due to quenching effects, and this approach has not been pursued.

The use of LIF for static pressure measurements in underexpanded jets was first proposed by McDaniel (1983). Subsequently, Hiller et al. (1986) applied LIF to the pressure field of an underexpanded round nitrogen jet, using image-intensified detection. These results were encouraging and demonstrated the feasibility of LIF for pressure measurements.

Due to collisional quenching of the excited state, LIF is a function of temperature as well as pressure. This has prompted the use of laser-induced iodine fluorescence for a number of temperature measurements in compressible flows; for example, the flow field within a Laval nozzle (Fletcher and McDaniel, 1987) and in a nonreacting scramjet combustor simulation (Fletcher and McDaniel, 1987a). However, these measurements have been limited to mean temperatures. Species other than iodine have been used for LIF temperature measurements: Gross and McKenzie (1985) reported that LIF from nitric oxide (NO) was sensitive to temperatures in the range 150-295 K, with uncertainties using current technology of one

percent for mean temperatures and six percent for temperature fluctuations. Traditional techniques of infrared spectroscopy have also been used to measure mean stagnation temperature ratios for supersonic jets (Robinson et al., 1979).

Concentration measurements needed to find the mixing properties of underexpanded jets are very limited. Birch et al. (1984) measured the concentration decay of underexpanded natural gas jets injected into still air using sampling and gas chromatography. These measurements were limited to the flow axis, and emphasize conditions in the constant-pressure portion of the flow.

Computations of underexpanded jet flows have also proved to be very challenging and are not well established due to uncertainties in numerical methods and lack of data concerning turbulence properties to assess turbulence modeling approximations. Vatsa et al. (1981, 1982) report calculations for slightly underexpanded jets, using a quasiparabolic algorithm and an empirical algebraic turbulence model. The comparison between predicted and measured static pressure distributions was encouraging. Mikhail et al. (1980) report some computations using MacCormack's explicit scheme for a nozzle boat-tail configuration. During this investigation, computations for a highly underexpanded jet, containing a Mach disk were attempted, however, the solution converged to only the weak-shock mode. Therefore, further studies of computation methods capable of the strong shock-capturing were suggested.

More recently, Dash and Wolf (1984a), Dash et al. (1985), Seiner et al. (1985), and Dash et al. (1986) reported strong-shock-capturing computations of turbulent underexpanded jets, using several contemporary turbulence models, where the stiffness difficulties were avoided. The parabolized Navier-Stokes approach was developed to calculate the fully-coupled viscous/inviscid jet interaction flowfield. The code, which is called SCIPVIS, includes a hyperbolic/parabolic method for treating the supersonic viscous portions of the flow, with a partially-parabolic method for treating the subsonic nonconstant pressure mixing region. The comparison between predictions and existing measurements for nozzle flows was encouraging, especially for mean static pressure variations along the jet axis. These properties are largely governed by inviscid effects, however, so that the effectiveness of turbulent mixing predictions are still uncertain.

Analyses, or turbulent models, used for high-speed and underexpanded jet flows are largely adopted directly from methods used for low-speed flows (Dash and Wolf, 1984a, 1984b). It has not been possible to adequately evaluate these methods, or extend them if necessary, due to the unavailability of needed structure measurements. It is widely recognized that turbulent mixing properties are influenced by compressible flow phenomena. In particular, the growth of mixing layers in high-speed shear layers is known to be smaller than in low-speed flows (Dash and Wolf, 1984a, 1984b; Bogdanoff, 1983; and Papamoschou and Roshko, 1986). The importance of this effect can be represented by the convective Mach number of the mixing layer. Compressibility corrections for higher-order turbulence closures

have been proposed (Dash et al., 1975), however, limited evaluation of these methods has not been very encouraging (Dash and Wolf, 1984a, 1984b).

Due to the difficulties of exact treatment of the external expansion region of underexpanded jets, a number of approximate methods have been proposed (Kalgathi, 1981, 1984; Birch et al., 1984, 1987; Hess et al., 1973; and Gore et al., 1986). This involves avoiding detailed analysis of the near-field and transition regions, by seeking an equivalent adapted-jet initial condition. Kalgathi (1981, 1984) and Gore et al. (1986) assumed that the jet exit flow can be approximated by an equivalent converging/diverging nozzle flow where the flow at the exit of the nozzle has expanded to the ambient pressure. Several other equivalent adapted exit conditions have been proposed, as follows: a "pseudo diameter" approximation which only satisfies conservation of mass (Birch et al., 1984); a "pseudo source" method where both the mass and momentum of the jet are satisfied (Birch et al., 1987); and a "momentum/velocity" technique where all of the excess pressure at the jet exit is assumed to effectively increase the momentum of the jet (Hess et al., 1973; Gore et al., 1986). All these concepts were predated by theoretical ideas reported by Hess et al. (1973). The details of near-field cannot be found using these approximations; however, some success has been achieved concerning the far-field mixing properties (Birch et al., 1987).

To summarize, past measurements of underexpanded jets are very limited, due to difficulties in obtaining adequate instrument accuracy. However, laser-based nonintrusive techniques have been reported which appear to be promising for measurements of velocities and scalar properties in the near-field of underexpanded jets. Recent predictions of these flows have been reported by Dash and coworkers (1984, 1984a, 1985, 1986), using contemporary turbulent mixing models. However, evaluation of these predictions has not been very definitive due to the limited availability of measurements, and methods for treating reduced turbulent mixing due to compressibility effects at high convective Mach numbers have not been very encouraging. Several approximate methods, using effective initial conditions, have also been proposed, to avoid direct treatment of the near-field shock-containing portion of the flow. The relative merits of these methods, however, have not been established.

1.3 Specific Objectives

The preceding discussion has indicated that subsonic jets have been extensively studied, both theoretically and experimentally. Past studies of underexpanded jets, however, are quite limited. Existing measurements of underexpanded jets consist of flow visualizations of shock structure and static pressure measurements along the axis of the flow, which emphasize the inviscid portions of the flow; and structure measurements in the far-field, largely to test proposals for equivalent jet exit conditions which seek to avoid computations of flow properties in the complex shock-containing flow near the jet exit. Evaluation of predictions for underexpanded jets has accordingly not proceeded very far, although effects of compressibility are known at high convective Mach numbers.

In order to help overcome some of the current limitations concerning understanding of the properties of turbulent sonic underexpanded gas jets, the present investigation was undertaken with the following specific objectives:

1. To complete new measurements of the structure and mixing properties of the flow, as follows: the shock-cell structure, using Schlieren photography; mean and fluctuating velocities, using LDA; mixing properties, using LIF; and static pressure distributions, also using LIF.
2. To employ the new measurements, as well as data already in the literature, to evaluate methods for predicting the structure of underexpanded jets: considering methods capable of treating the shock-containing near-field region; and approximate methods, based on equivalent jet exit conditions, for estimates of far-field mixing levels.

Measurements were limited to steady injection of air into still air, from a round passage. A long length-to-diameter ratio passage was used, yielding nearly fully-developed pipe flow at the exit. This provides a well-defined initial condition for the flow, with numerous practical applications, which has not been considered in the past. Measurements were also completed for subsonic and sonic adapted jets, in order to provide baselines for experimental and theoretical methods prior to treating underexpanded jets.

The following discussion is brief; more details and a complete tabulation of data are provided by Chuech (1987). The report begins with a description of experimental and theoretical methods. Results are then discussed beginning with subsonic jets and finally considering related supersonic flows and underexpanded jets. The report ends with a summary of the main conclusions drawn from the study.

2. EXPERIMENTAL METHODS

2.1 Apparatus

The overall arrangement of the air-jet apparatus is illustrated in Fig. 11. The apparatus is relatively simple, involving an air supply, a long length-to-diameter horizontal passage exhausting to room conditions, and an exhaust system. Measurements included flow visualization, using Schlieren photography; mean and fluctuating velocities, using laser-Doppler anemometry (LDA); mixing levels, or the mean and fluctuating concentrations of a trace species, using laser-induced iodine fluorescence (LIF); and mean static pressures, using the collision quenching of LIF.

The test apparatus was located in a room $6\text{ m} \times 7.5\text{ m} \times 4\text{ m}$ high. The air supply was provided by laboratory facilities, consisting of dried and filtered air drawn from a storage tank (storage pressures in excess of 10 MPa with an air dewpoint less than 240 K). Air flow rates were controlled with a dome regulator (Grove R94393) and metered with a standard critical flow nozzle (Flow-Dyne Engineering, Inc., type NS16-7, Model No. N160200-SA). Calibration of the nozzle was provided by the manufacturer (0.75 percent accuracy, traceable to the National Bureau of Standards). The inlet temperature of the critical-flow nozzle was monitored with a thermocouple. A relief valve (McMaster-Carr Supply Co., Pop Safety Valve, Part No. 4673K53, set roughly at 1 MPa) was installed to avoid accidental overpressure which could damage the system.

LDA measurements used oil seeding particles in the flow, while LIF involved seeding with iodine vapor. The seeding-particle and iodine-vapor generators could be valved from the system when not in use. The oil particles and iodine vapor are objectional in the test area; therefore, the jet flow was passed outside the building through a vent having an inlet diameter of 300 mm.

Except for LIF measurements of static pressures, the jet exhausted into the room before leaving through a vent. For the static pressure measurements, the jet exhausted into an enclosure, which was attached to the vent at its downstream end. The enclosure was constructed from a polyethylene cylindrical tank (Mattern and Lee Equipment, Inc., Model No. 82, 710 mm diameter \times 810 mm long). The tank was modified so that its upstream end was sealed to the injector, using a flexible bladder so that the jet could be traversed; therefore, the enclosure was at atmospheric pressure. Whether the enclosure was in place or not, the distance between the jet exit and the inlet of the exhaust system was greater than 500 mm. The passage exit was 1300 mm above the floor.

Air was supplied to the nozzle through a flexible hose. The nozzle assembly was constructed from plexiglass in order to avoid corrosion by iodine. The inlet of the nozzle was fitted with a flow straightener, consisting of a 19 mm diameter array of plastic straws, each having inside diameters of 6 mm and lengths of 75 mm. The flow straightener was followed by a circular profile contraction (2.8:1 area ratio) to the nozzle passage. The nozzle passage had a constant diameter of 9.5 mm and was 50 passage diameters long, to provide nearly fully-developed flow at the exit of the passage. Static pressure was monitored at the inlet of the contraction using a Heise, Model CMM 26629 pressure gage (0-2.4 MPa for a total pointer displacement of 1600 mm). Pressure was also monitored with four 500 μm diameter static pressure taps located 15, 45, 65 and 95 mm from the exit of the passage, which were read with a bank of mercury manometers (each 1830 mm high). These measurements were extrapolated to find the static pressure at the exit of the passage.

All optical components were mounted rigidly; therefore the nozzle was traversed to measure profiles of flow properties at various points. The aluminum plates supporting the nozzle assembly were mounted on two pairs of linear bearings (Thomson Co., Model SPB-12 and Model SPB-16) to provide traversing in the horizontal plane. The traverses were controlled by a stepping motor (Velmex, Inc., Model 8300) and a computer (IBM 9000) using two motor-driven Unislide assemblies (Velmex, Inc., Model B4018Q1J and Model B4021Q1J) having positioning accuracies of 5 μm . The mounting stand had four screw adjustments to control the height and angle of the flow.

2.2 Instrumentation

Measurements included flow visualization, mean and fluctuating velocities, mean and fluctuating concentrations, and mean static pressures. Techniques used in each instance are summarized in the following.

Flow Visualization. Continuous and spark Schlieren photography were used for flow visualization. The Schlieren system was based on two 150 mm diameter parabolic reflectors having focal lengths of 1220 mm. The continuous light source was provided by a 100 W mercury arc (PEK-109, Illumination Industries, 0.1 mm arc size), typically operating at 25 V DC. The starter and adjustable resistor were used to trigger and control the arc, with the intensity and the quality of the light adjusted using neutral-density and spatial optical filters. A vertical knife edge was used, yielding response to the refractive index gradient in the streamwise direction. Photographs were obtained using a 4 \times 5 Graphlex camera. High-speed black and white film (Polaroid, type 57, 4 \times 5 film, ASA 3000) was used, with an exposure time of 10 ms.

Except for the light source, the spark Schlieren system was identical to the continuous Schlieren system. The spark light source was fabricated in this laboratory. The system provided a 10 J discharge with a discharge duration of roughly 100 ns (20 kV and 5 nF capacitor discharge). The capacitor bank was loaded using a high-voltage DC power supply (Sorenson and Co., Model No. 230-6) yielding up to 30 kV. The system was operated in a darkened room with the camera shutter open during the period of spark discharge; therefore, the exposure time was fixed by the flash duration.

Velocity Measurements. Velocity measurements were carried out using a single-channel laser-Doppler anemometer (LDA), illustrated in Fig. 12. The components of the system are summarized in Table 1. The LDA was operated in the dual-beam, forward-scatter mode with off-axis light collection (25°) in order to achieve reasonably good signal-to-noise ratios and spatial resolution.

An argon-ion laser, yielding 1.7 W at 514.5 nm, was used for the LDA. A Bragg-cell frequency shifter eliminated directional bias and ambiguity. The optical arrangement yielded a

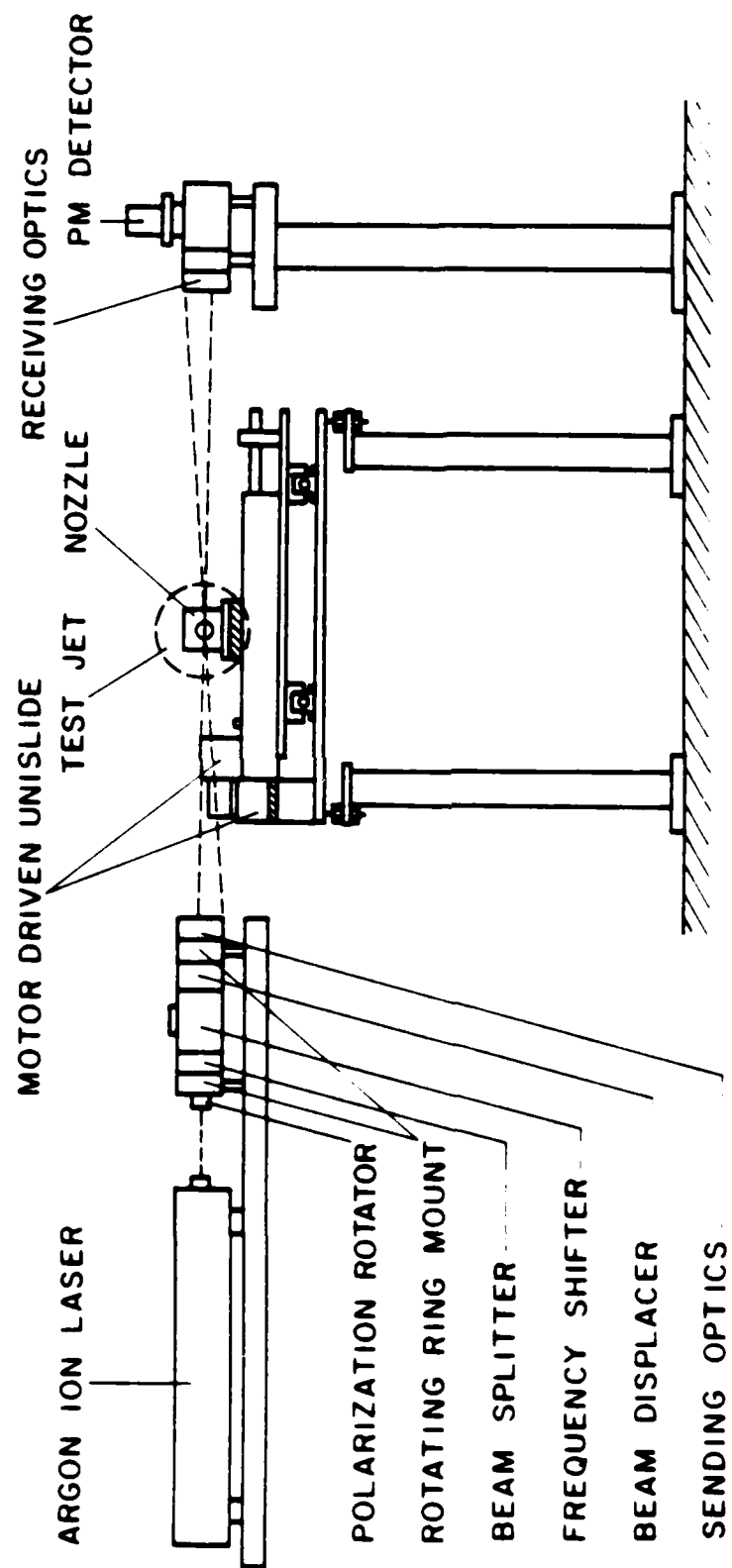


Fig. 12 Sketch of the LDA system.

Table 1. Summary of LDA Components

Component	Manufacturer	Model	Specification/Function
Argon-ion laser	Coherent	INNOVA 90-4	Single-line mode 1.7W at 514.5 nm; 1.5 mm (e^{-2} points) beam diameter.
Rotating mount	TSI	9179	56 mm length.
Rotating mount for beam splitter	TSI	9178-1	Length of optics module: 58 mm; Beam cover length: 61 mm.
Beam splitter	TSI	9115-1	50 mm beam spacing.
Receiving assembly	TSI	9140	X-Y adjustable focus: adjustment for photodetector.
Photomultiplier system	TSI	9160	200 MHz response; 0.20 mm aperture.
Transmitting lens	TSI	9119	For sending and receiving optical systems; 600 mm focal length; 60 mm clear aperture; 25 mm length.
Filter	TSI	9158	514.5 central wavelength; 6.3 nm bandwidth; 80% peak transmittance; 25 mm diameter.

Table 1. Summary of LDA Components (Continued)

Component	Manufacturer	Model	Specification/Function
Frequency shifter	TSI	9180-12	Bragg cell, 2 kHz to 40 MHz shift frequency.
RMS/DC/MS voltmeter	TSI	1076	True rms voltmeter.
Burst counter	TSI	1990C	Signal processor; 150 MHz maximum Doppler frequency.
A/D converter	LeCroy	8212A/8	12-bit and 2.5 mV resolution; 50 kHz bandwidth.
Memory	LeCroy	8800A	32 K memory.
Computer	IBM	9002	68000 8-MHz microprocessor; 128 K RAM; 128 K ROM.
Hard disk	IBM	9017	10 M memory.
Printer	IBM	5182	Color printer.

6.1 μm fringe spacing; and a measuring volume diameter and length of 200 μm and 460 μm . Owing to the dual-beam configuration, the closest allowable approach of the measuring volume to the plane of the nozzle exit was roughly 2 mm, since nearer positions caused the upstream beam to be interrupted by the nozzle assembly.

Smoke particles having average diameters of 500 nm were used to seed the flow for LDA measurements. These particles had characteristic response frequencies of 30 kHz – which was adequate for measurements for the subsonic and sonic portions of the flow. However, the particles could not respond to the rapid velocity changes encountered in passing through shock waves in the supersonic region.

Seeding densities yielded less than 0.3 particles/measuring volume. In the subsonic portions of the flow, seeding levels were high in comparison to flow length scales; therefore, a low burst-density, high data-density signal was obtained. This allowed data reduction as time averages of the analog output of the burst-counter signal processor, without problems of velocity bias. The output signal was acquired using a 12-bit A/D converter and stored on a 32 K fast memory, before transferring the data to a laboratory computer for processing and storage.

Bias errors and experimental uncertainties of the LDA measurements are discussed by Chuech (1987). Effects of gradient broadening were small for present test conditions; therefore, experimental uncertainties were largely governed by sampling times. Estimated experimental uncertainties (95 percent confidence) are less than ten percent for both mean and fluctuating velocities, evaluated following Kline and McClintock (1953). Measurements were repeatable within the range of the uncertainties.

Concentration Measurements. Laser-induced fluorescence (LIF) was used to measure mean and fluctuating concentrations. Figure 13 is a sketch of the LIF system, while the system components are summarized in Table 2. The LIF signal originated from inelastic scattering of light from a laser beam, due to the presence of trace amounts of iodine vapor in the jet flow. The LIF signal was produced from the overlapping P13 and R15 rotation lines in the $43' - 0''$ vibration band of the B-X electronic transition of iodine (McDaniel, 1983, 1983a) – which is within the gain profile of the 514.5 nm line of an argon-ion laser (the transition is located 2.0 GHz to the high-frequency side of the line center). The intensity of the signal is proportional to the concentration of iodine molecules in the measuring volume; therefore, the measurement indicates the extent of mixing of the flow with the surroundings (Lai and Faeth, 1987).

The LIF system is based on an arrangement developed by Lai and Faeth (1987). The laser was operated at a wavelength of 514.5 nm. A portion of the laser beam was split from the main beam in order to provide continuous monitoring of beam power. Another portion was split and directed across the exit of the jet: the transmitted power of this beam was measured, giving the concentration of iodine seeding gas at the jet exit by the degree of absorption.

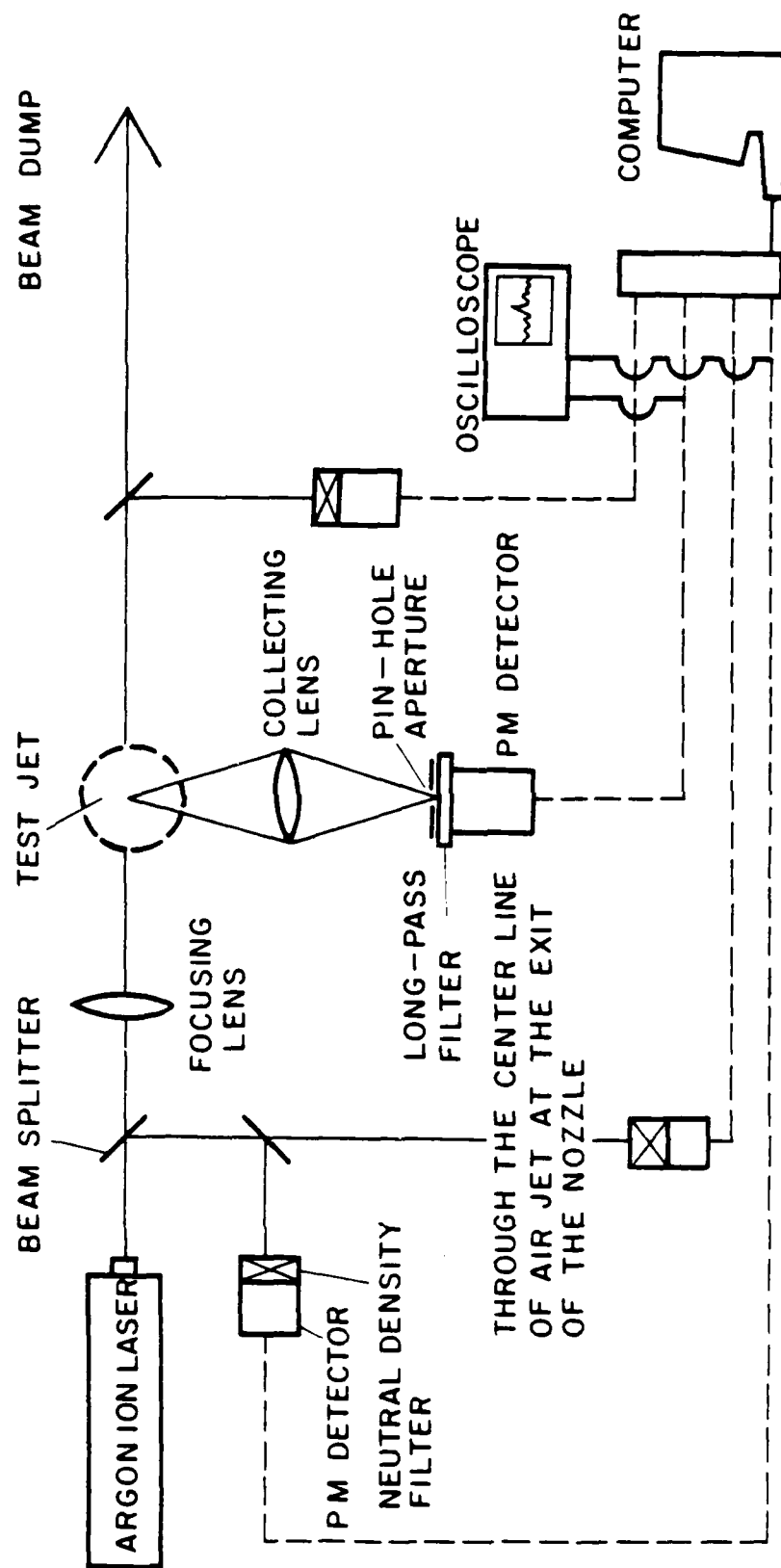


Fig. 13 Sketch of the LIF system.

Table 2. Summary of LIF Components

Component	Manufacturer	Model	Specification/Function
Argon-ion laser	Coherent	INNOVA 90-4	Single-line mode: 1700 mW at 514.5 nm 1.5 mm (e ² points) beam diameter.
Beam splitter	Oriel	3740	Pellicle beam splitter: 7 μ m thick; transmits 92% in visible and near-IR range.
Neutral density filter	Oriel	5077	Sets of 6 visible absorption.
Collecting lens	Canon	FD 85/1.2L	85 mm focal length; 71 mm clear aperture.
Focusing lens	TSI	9119	600 mm focal length; 60 mm clear aperture.
Aperture	---	----	1.0 mm diameter.
Long pass filter	Oriel	51300	50% transmission, cutoff at 530 nm.
Photomultiplier Assembly:			
Tube	Hamamatsu	R268	Bialkali photocathode; 11 stages: head-on.

Table 2. Summary of LIF Components (Continued)

Component	Manufacturer	Model	Specification/Function
Tube	Hamamatsu	R787	Multi-alkali photocathode; 9 stages; side-on.
Magnetic shield	Hamamatsu	E989	
Socket	Hamamatsu	C1053	5 MHz frequency response.
High voltage power supply	Bertram	215	0 - +3000 V; 0 - 5 mA DC.
Frequency filter	ITHACO	4213	Variable bandpass: high-pass: 1 Hz - 1 MHz; low-pass: 1 Hz - 100 kHz; cutoff accuracy $\pm 1\%$.
Spectral analyzer	Hewlett Packard	3580A	Maximum frequency range: 50 kHz.
X-Y recorder	Hewlett Packard	7035B	
A/D converter	LeCroy	8212 A/8	12-bit and 2.5 mV resolution; 50 kHz bandwidth.
Memory	LeCroy	8800 A	32 K memory.

Table 2. Summary of LIF Components (Continued)

Component	Manufacturer	Model	Specification/Function
Computer	IBM	9002	68000 8-MHz microprocessor; 128 K RAM; 128 K ROM.
Hard disk	IBM	9017	10 M memory.
Printer	IBM	5182	Color printer.

Finally, the intensity of the beam passing through the measuring volume was also measured, so that effects of absorption on the beam power at the measuring station could be estimated. However, this correction was small, as were effects of reabsorption of fluorescence, since beam lengths through iodine-containing portions of the flow were relatively short. The other two measurements allowed correction of raw data for laser power and seeding density fluctuations when the measurements were processed.

The LIF signal was observed from an angle of 14° to the optical axis in the forward-scatter direction. An F1.2 lens was used to collect scattered light to provide good signal-to-noise ratios. The measuring volume was fixed by the waist diameter of the focussed laser beam and the field stop of the detector optics – yielding a cylindrical measuring volume with a diameter of 0.2 mm and a length of 1 mm. A current-to-voltage converter having frequency response to 5 MHz was used with the photomultiplier tube of the detector, in order to resolve concentration fluctuations in the high-speed flows.

Care was taken to reduce noise sources of the photomultipliers: magnetic shield cases were used to eliminate unwanted ambient magnetic fields; the tubes were operated 200-300 V lower than the maximum rating, to reduce anode dark current due to field emission; the average anode current was kept below 1 μ A, to avoid current drift due to baseline drift; and the voltage divider current was kept at least 20 times the anode output current, to prevent deviation from linear response of the tube.

The air flow was seeded with iodine by passing a portion through a bed of iodine crystals (bed diameter and depth of 130 and 330 mm). The bed operated at room temperature and the flow was saturated at the exit of the bed; therefore, the concentration of iodine vapor, which is proportional to the iodine vapor pressure, varied with changes in room temperature. These changes, however, are accounted for by the monitoring system described earlier. The iodine crystals were reagent grade, having an initial flake shape of 2-8 mm diameter and 0.5 mm thickness. Iodine vapor is relatively corrosive even at low concentrations; therefore, components downstream of the iodine seeder were plexiglass, plastic or brass – all of which have reasonably good corrosion resistance to iodine.

The signal scattered to the detector includes a relatively strong Rayleigh-scattered signal at the laser line (514.5 nm) along with the LIF signal at longer wavelengths. A spectrum of this signal, at atmospheric pressure and room temperature, is illustrated in Fig. 14, based on measurements reported by Lai and Faeth (1987). For the excited vibrational level of the $43'-0''$ transition that is populated by absorption of the laser beam, a vibrational progression of fluorescence Stokes bands results from transition to various ground vibrational levels. There are actually four rotational transitions (R11, P13, R15 and P17) that make up each Stokes band while the P13 and R15 rotational transitions overlap together to form a triple rotational structure. However, a low resolution (8 nm bandwidth) monochromator was used for these measurements; therefore, the laser line appears as a strong band and the details of the spectra of

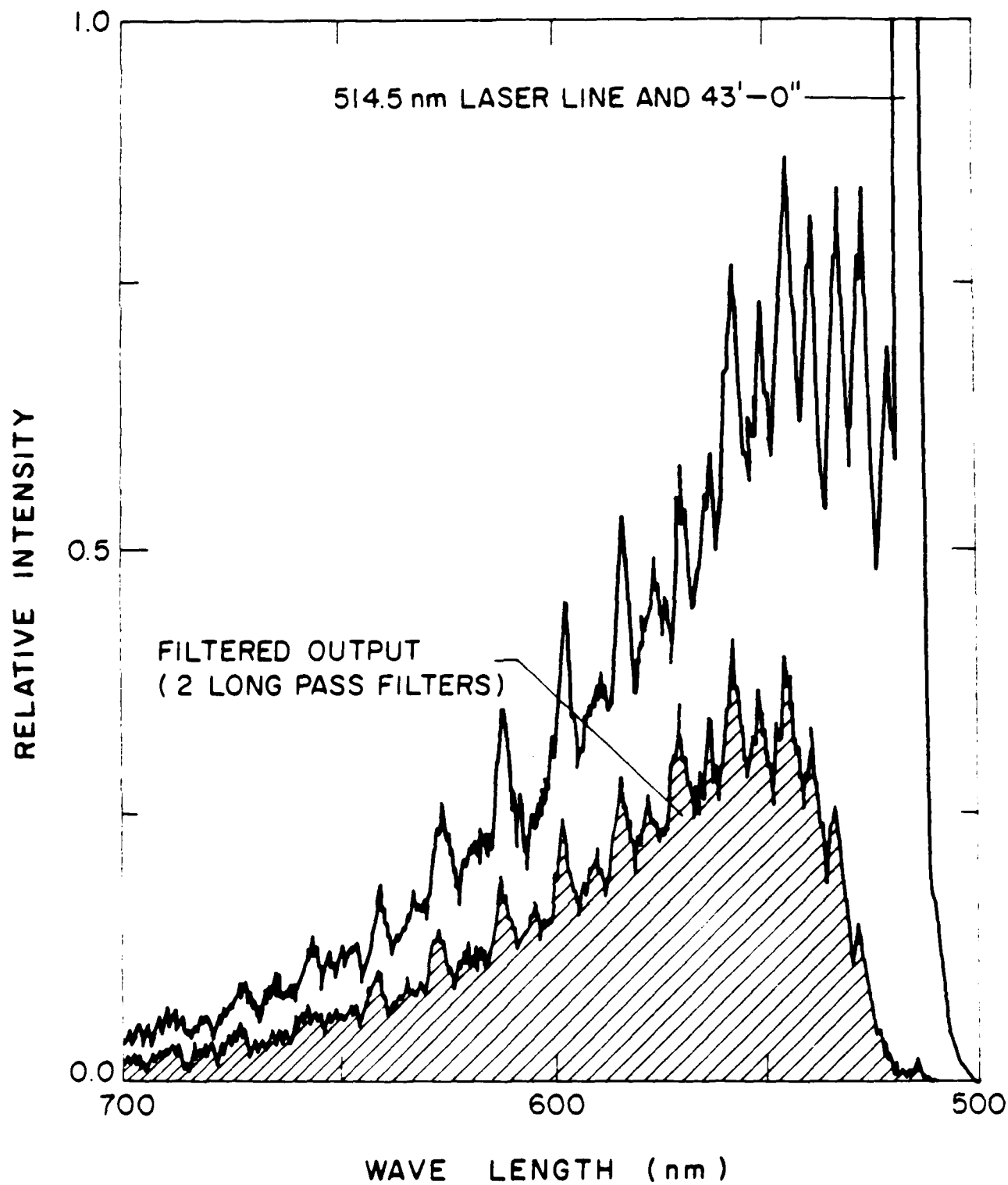


Fig. 14 Original and filtered LIF spectrum: from Lai and Faeth (1987).

the Stokes bands at longer wavelengths are lost. The laser line must be blocked to obtain a signal proportional to iodine concentration, at a given static pressure and temperature. This was done by installing a series of long-pass optical filters in front of the detector. The resulting spectrum, after filtering, is also illustrated in Fig. 14. The filters clearly eliminate the signal at the laser line.

The calibration curve of the optically filtered LIF signal, as a function of mixture fraction (the fraction of mass which originated from the jet), is illustrated in Fig. 15. These results were obtained at room temperature and pressure, with unsaturated fluorescence, i.e., the signal intensity was proportional to laser power. The calibration shows that the filtered signal is a linear function of mixture fraction, which is directly proportional to iodine concentration.

Calibrations similar to Fig. 15 are sufficient to treat all points in the flow field where the pressure and temperature are equal to ambient conditions, e.g., the adapted jets everywhere and the far-field region of the underexpanded jets. The near-field region of the underexpanded jets, however, involves local variations of mean static pressure and temperature that must be considered (static pressure and temperature fluctuations are small for present flows and can be neglected). These effects were examined using the analysis of McDaniel (1983b). For excitation at 514.5 nm, the intensity of the LIF signal can be written as follows:

$$I_{LIF} = K(T) N_{I_2} / p \quad (2.1)$$

where $K(T)$ is a complex function of temperature which accounts for the relative proportion of the various transitions, effects of collisional quenching, broadening, the finite width of the laser line, the laser power, and the transmission properties of the long-pass optical filters. Equation (2.1) is written for the high pressure limit, where quenching rates are fast in comparison to the spontaneous decay causing fluorescence, since this limit is satisfied for present test conditions. The pressure dependence of equation (2.1) results from collisional quenching of excited iodine molecules before they can decay.

At a fixed static temperature and pressure, equation (2.1) indicates that the LIF signal is proportional to iodine concentration, which is confirmed by the calibration illustrated in Fig. 15. For measurements in underexpanded jets, however, static temperatures and pressures vary in a complex manner, e.g., temperatures vary isentropically with pressure through expansion waves and weak compression waves, but vary in a different manner through shock waves where the process has irreversibilities. Fortunately, however, $K(T)$ is a rather weak function of temperature for present test conditions, varying less than 7 percent for an underexpansion ratio of 1.2 and less than 11 percent for an underexpansion ratio of 1.37; therefore, the LIF signal is approximately proportional to iodine concentration and inversely proportional to pressure. This simplification arises since static temperatures vary to a lesser degree than static pressures, and $K(T)$ varies only in a small range due to the limited variation of static temperatures for the present test conditions. As a result, concentrations were determined by

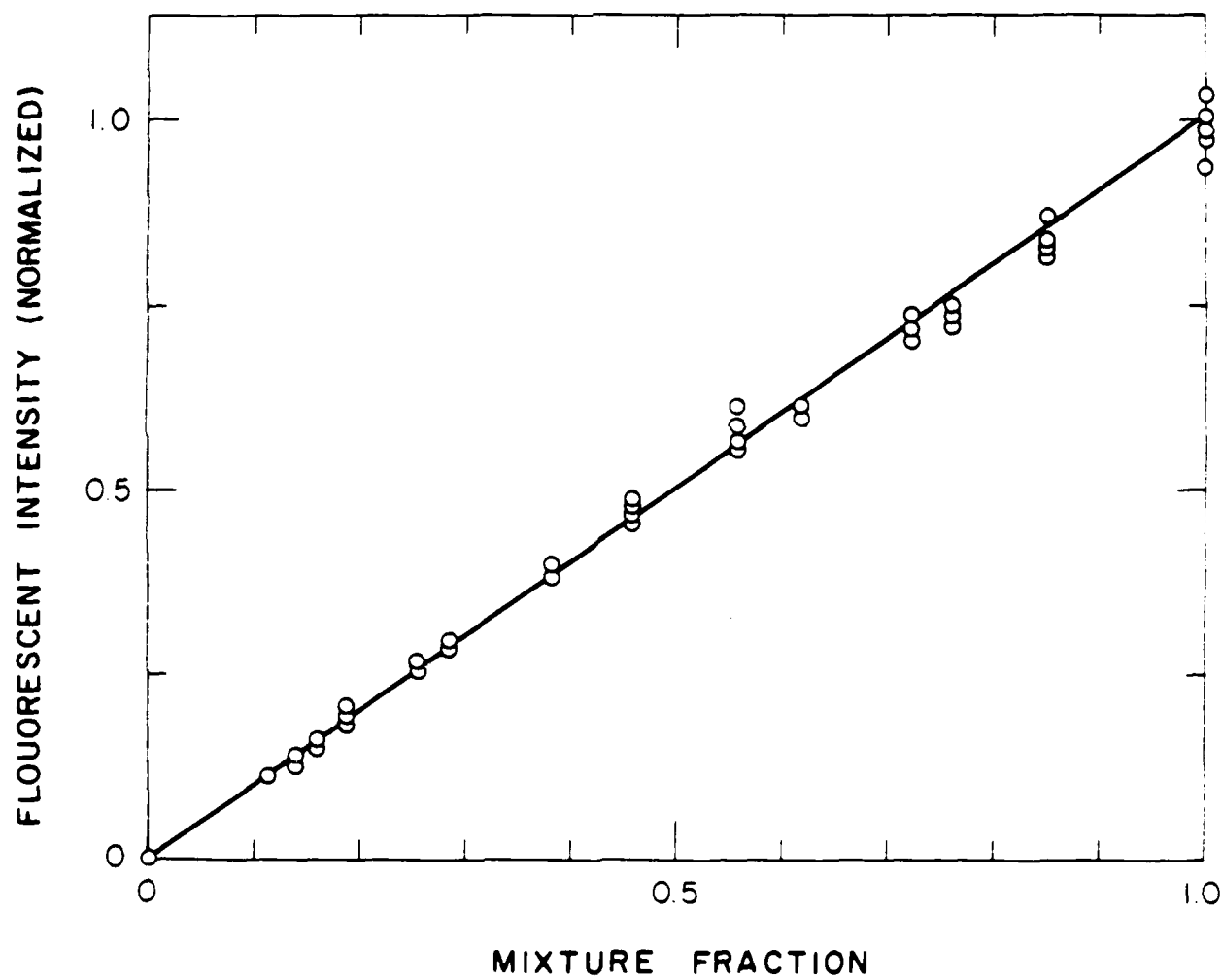


Fig. 15 Calibration of LIF intensity with mixture fraction.

correcting the raw data at each point, using the static pressure measurements described in the next section, through equation (2.1). The intensity of laser-induced iodine fluorescence signals, indicating mixing concentrations at the probe volume, were sampled and processed using the same data acquisition system, A/D converter, and computer, as the LDA measurements.

The power spectral densities of concentration fluctuations were measured at various points using a spectral analyzer (Hewlett Packard, Model 3580A) and a variable electronic filter with a 1 percent cutoff frequency accuracy (Ithaco, Model 4213). The power spectral density measurements provided a means of monitoring signal-to-noise ratios, which are crucial for accurate measurements of concentration fluctuations of high-speed flows. Some typical examples, along the axis of the subsonic jet considered during the present investigation, are illustrated in Fig. 16. The results at $x/d = 5$ and 10 are truncated due to the 50 kHz limit of the spectrum analyzer. However, results of $x/d = 20$ reach the noise baseline at frequencies below 50 kHz, and exhibit reasonably good signal-to-noise ratios for these measurements.

Errors and experimental uncertainties for the LIF measurements are discussed in Chuech (1987). Effects of gradient broadening were generally small for present test conditions, except near the edge of the flow at the exit of the jet. Experimental uncertainties were largely governed by corrections for static pressure changes (in the near-field region of underexpanded jets), finite sampling times, drift in experimental operating conditions and iodine concentrations, and absorption of the laser beam and scattered fluorescence by iodine. Due to these factors, experimental uncertainties (95 percent confidence) of mean concentrations were less than 10 percent, where the pressure was equal to the ambient pressure, increasing to less than 20 percent at the highest pressures where measurements were made. Errors in concentration fluctuations were generally higher, due to signal noise, particularly when large signal bandwidths were needed in high-speed portions of the flow. This yielded experimental uncertainties (95 percent confidence) generally less than 20 percent for all static pressure conditions. Measurements were repeatable within these ranges over the period of testing.

Static Pressure Measurements. Collisional quenching effects were used to measure mean static pressures, through equation (2.1). The optical arrangement for these measurements was the same as for the concentration measurements. However, effects of varying iodine concentration were removed by exhausting the jet into a vented enclosure, so that iodine concentrations were constant throughout the flow field. The LIF signal then becomes inversely proportional to pressure.

The effect of pressure on the LIF signal was verified by calibration measurements. These tests involved a modified vacuum cell (MDC Mfg., Inc.) having four windows, to allow LIF measurements at the center of the cell. Iodine crystals were placed in the cell and allowed to come to equilibrium, yielding a constant concentration (number density) of iodine molecules within the cell. The pressure was then varied by admitting air to the cell, or venting it, insuring

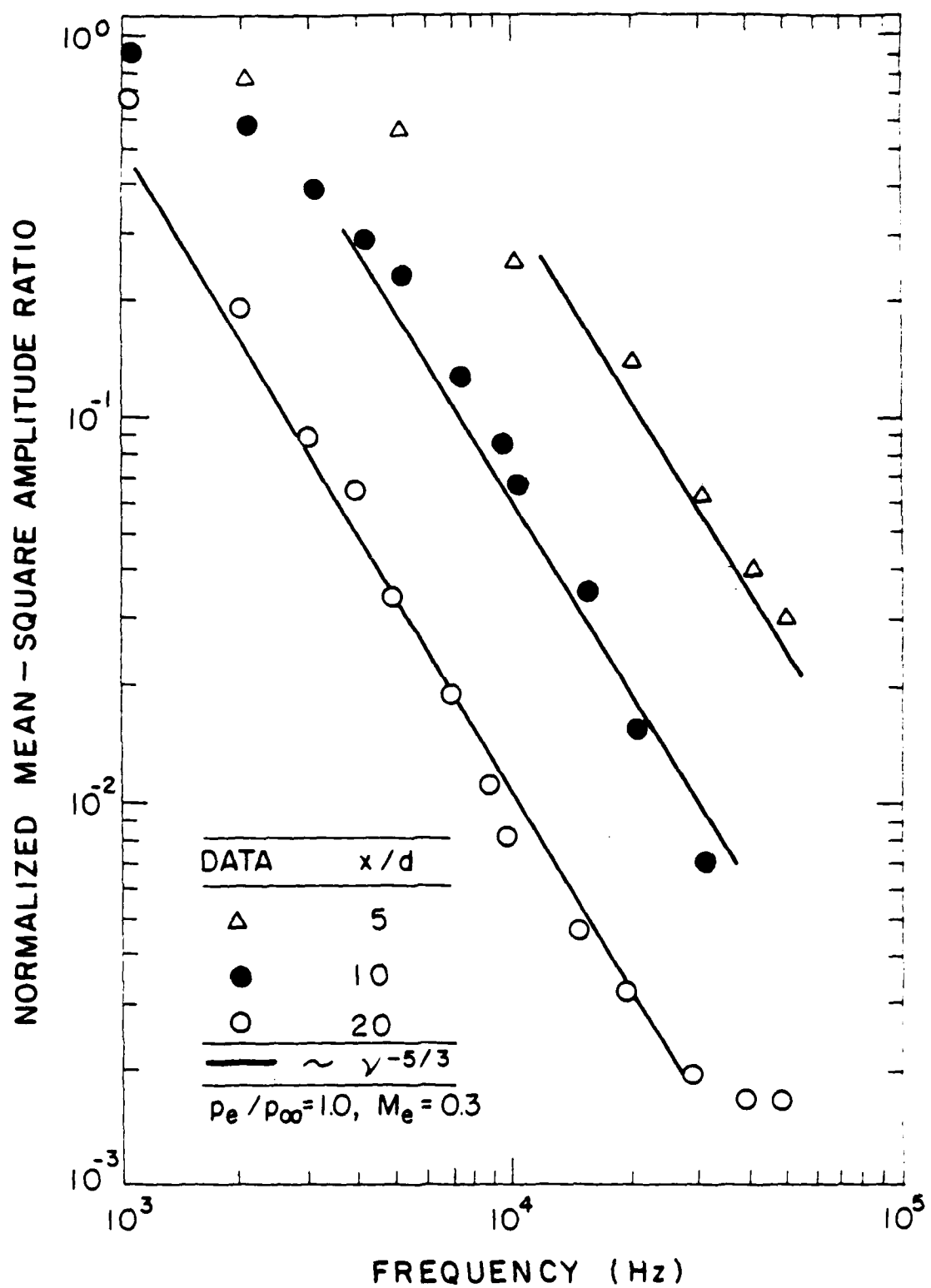


Fig. 16 Power spectral density of mixing concentration fluctuations at the centerline of a subsonic jet.

sufficient time for equilibration of the iodine concentration before new measurements were made. The temperature of the cell was monitored, to allow for variations of iodine vapor pressure with temperature.

The calibration measurements for the effect of pressure are illustrated in Fig. 17. LIF intensity is plotted as a function of pressure with both variables normalized by results at atmospheric pressure. The pressure range of the tests extended from 1.0-2.2 atm. The predicted results, according to equation (2.1), are also illustrated on the figure. The agreement between predictions and measurements is clearly quite satisfactory. McDaniel (1983b) completed similar measurements at subatmospheric pressures, showing that LIF intensity remains inversely proportional to pressure for pressures as low as 0.5 atm, which is lower than the lowest pressure encountered during present tests.

Errors and experimental uncertainties for the static pressure measurements are discussed by Chuech (1987). The pressure measurements were significantly gradient broadened across shock waves, due to the finite size (0.2 mm diameter and 1 mm long) of the LIF measuring volume. However, gradient-broadening effects were small elsewhere. Experimental uncertainties of the mean static pressure measurements were largely due to potential effects of temperature variations on $K(T)$, and discretization and calibration accuracies. Exclusive of gradient broadening, experimental uncertainties (95 percent confidence) of the mean static pressure measurements are estimated to be less than 13 percent of the difference between the static and ambient pressures.

2.3 Test Conditions

Present Measurements. Test conditions for the flow visualization tests are summarized in Table 3. Subsonic, sonic, and underexpanded air jets in still air were considered, with underexpansion ratios up to 4.2. Addy (1981) finds that Mach disks appear for underexpansion ratios of 2-3; therefore, this range was considered during the tests.

Test conditions for structure measurements are summarized in Table 4. Flow visualization, velocity, concentration and mean static pressure measurements were completed for the first three test conditions. Measurements for the fourth condition were limited to flow visualization and mean static pressures. All the flows were highly turbulent, with Reynolds numbers at the jet exit in the range 57,300 - 367,200. This minimizes effects of laminar transport, which are not very important for practical applications. The measurements emphasize near-injector conditions where underexpansion effects are important, extending from the jet exit to roughly 20 injector diameters downstream. Convective Mach numbers for these tests were less than 0.6; therefore, effects of compressibility were small (Bogdanoff, 1983; Papamoschou and Roshko, 1986).

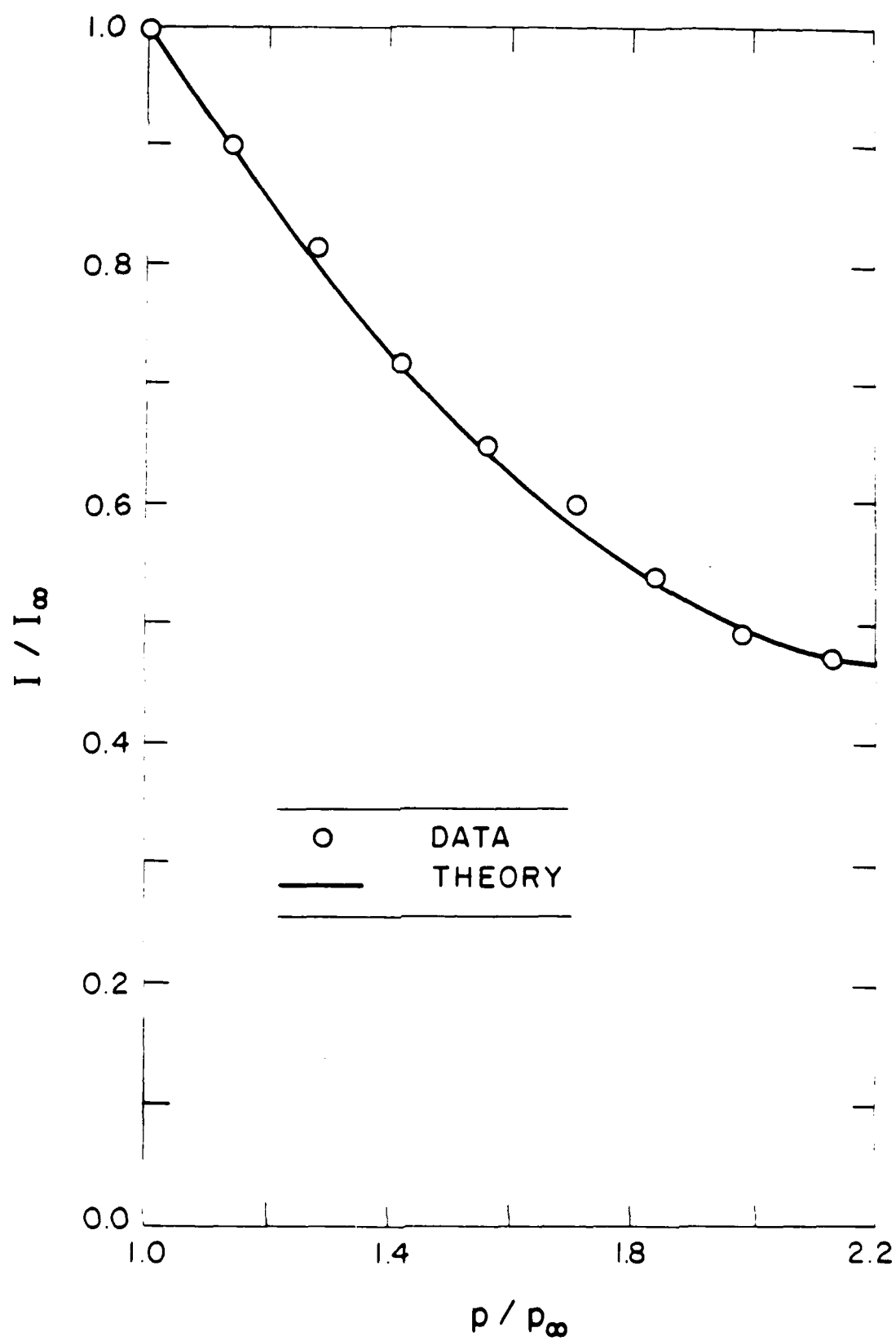


Fig. 17 Calibration of LIF intensity with pressure.

Table 3. Test Conditions for Flow Visualization^a

Parameter	Range
Mass flow rate (kg/s)	0.006 - 0.113
Exit plane Mach number	0.2 - 1.0
Underexpansion ratio	1.0 - 4.2
Reynolds number ^b	44,000 - 1,125,600

^aHorizontal air jets injected into still room air: injector diameter 9.53 mm, injector length-to-diameter ratio 50, ambient pressure 99 ± 0.5 kPa, and ambient temperature 297 ± 3 K.

^b $Re = u_e d / \nu_e$.

Table 4. Test Conditions for Structure Measurements^a

Test Condition	1	2	3	4
Jet type	Subsonic	Sonic	Underexpanded	Underexpanded
Mass flow rate (kg/s)	0.008	0.027	0.032	0.037
Exit plane Mach number	0.30	1.00	1.00	1.00
Convective Mach number ^b	0.16	0.48	0.54	0.58
Underexpansion ratio	1.00	1.00	1.20	1.37
Reynolds number ^c	57,300	268,000	321,600	367,200
Froude number $\times 10^6$ ^d	11.5	1.04	1.04	1.04

^aHorizontal air jets into still room air: injector diameter 9.53 mm; injector length-to-diameter ratio 50, ambient pressure 99 ± 0.5 kPa, and ambient temperature 297 ± 3 K.

^bMaximum convective Mach number in flow as defined by Papamoschou and Roshko (1986).

^c $Re = u_e d / \nu_e$.

^d $Fr = ad / u_e^2$.

Related Measurements. Measurements from earlier studies were also compared with present predictions and measurements. These sources are summarized in Table 5. Subsonic jets include measurements of Becker et al. (1967) and Wagnanski and Fiedler (1969) for slug flows; and Birch et al. (1978) and Shuen et al. (1984) for fully-developed pipe flows. Underexpanded jets include measurements of Addy (1981), Birch et al. (1984, 1987), and Ewan and Moody (1986) for convergent nozzles; and Seiner and Norum (1980) and Eggers (1966) for convergent/divergent nozzles. All the underexpanded jet measurements in Table 5 approximate slug flow at the jet exit. All the flows in Table 5 have Reynolds numbers greater than 10^4 and are reasonably turbulent. The measurements of Birch et al. (1984, 1987, Eggers (1966) and Seiner and Norum (1980) all involve convective Mach numbers greater than 0.6, so that significant reductions of turbulent mixing rates in these flows due to compressibility is expected (Bogdanoff, 1983; Papamoschou and Roshko, 1986).

3. THEORETICAL METHODS: ADAPTED JETS

3.1 Description of the Analysis

The analysis used for adapted jets is described in this chapter; similar considerations for underexpanded jets are discussed in the next chapter. The approach used is based on methods developed earlier in this laboratory for low-speed variable-density flows (Jeng and Faeth, 1984). This involves estimating turbulence properties using a k - ϵ - g turbulence model which has been effective for a variety of constant- and variable-density single-phase round jets (Faeth, 1983; Jeng and Faeth, 1984; Shuen et al., 1984; Sun and Faeth, 1986). The main changes needed for present work involve treating effects of relatively high flow Mach numbers, particularly when underexpanded jets are approximated using adapted jets having effective initial conditions (denoted effective adapted jets). This extension is made following Dash and Wolf (1984, 1984a, 1984b) and Dash et al. (1978, 1985, 1986), yielding a unified turbulence model for all the flows considered here.

In addition to the present flows (Table 4), measurements reported by Becker et al. (1967), Birch et al. (1978), Shuen et al. (1984) and Wagnanski and Fiedler (1969), see Table 5, were considered during the calculations. All these flows involve steady injection of a gas from a round passage, with no swirl, into a still gaseous environment. The flows generally involve variable-density phenomena, due to static temperature changes caused by changes of velocity or differences in scalar properties (temperature or composition) from injector exit to ambient conditions.

The major assumptions of the analysis are as follows: steady flow (in the mean), with no swirl, from a round passage into a still gaseous environment; the boundary-layer approximations apply; either constant-pressure flow with negligible effects of buoyancy (for present test conditions) or buoyancy forces aligned in the streamwise direction (for the test conditions of others); axisymmetric flow; ideal gas mixture with constant specific heats for

Table 5 Test Conditions for Related Measurements

Source	Flow Gas	Nozzle Type	Diameter ^a	Initial Condition	Mach Number ^b	Convective Mach number ^c	Reynolds Number ^d	Underexpansion Ratio	Instrumentation
<u>Subsonic Jets:</u>									
Becker et al. (1967)	Air	Convergent Nozzle	6.35	Slug Flow	0.38	0.19	54,000	1.0	Concentration: Mie Scattering
Birch et al. (1978)	Methane	Long Passage	12.65	Fully Dev. Pipe Flow	0.06	0.03	16,000	1.0	Concentration: Raman Scattering
Shuen et al. (1984)	Air	Long Passage	10.9	Fully Dev. Pipe Flow	0.10	0.05	22,000	1.0	Velocity: LDA
Wyganski and Fielder (1969)	Air	Convergent Nozzle	26.41	Slug Flow	0.21	0.10	120,000	1.0	Velocity: Hot Wire
<u>Underexpanded Jets:</u>									
Addy (1981)	Air, Helium	Convergent Nozzle	12.7	Slug Flow	1.00	--	100,000-5,000,000	1-5	Schlieren Photography
Birch et al. (1984)	Natural gas	Convergent Nozzle	2.7	Slug Flow	1.00	0.77	163,000	1.9	Concentration Gas Chromatograph

Table 5 Test Conditions for Related Measurements (cont.)

Source	Flow Gas	Nozzle Type	Diameter ^a	Initial Condition	Mach Number ^b	Convective Mach number ^c	Reynolds Number ^d	Underexpansion Ratio	Instrumentation
Birch et al. (1987)	Air	Convergent Nozzle	2.7	Slug Flow	1.00	0.65	23,000	1.9	Velocity: Hot Film Anemometry
Eggers (1966)	Air	Convergent Nozzle	25.6	Slug Flow	2.20	0.92	3,200,000	1.0	Velocity: Hot Wire
Ewan and Moody (1986)	Air, Helium	Convergent Nozzle	6.3 12.7 25.4	Slug Flow	1.00	--	76,000- 1,100,000	2.7-10	Shadowgraphs, Velocity: LDA
Seiner and Norum (1980)	Air	Conv.-Div. Nozzle	50	Slug Flow	2.00	0.94	8,000,000	1.45	Pressure: Static Press. Probe

^a Nozzle exit diameter, d (mm).

^b Average Mach number at the nozzle exit.

^c Maximum convective Mach number in flow as defined by Papamoschou and Roshko (1986).

^d $Re = u_e d / \nu_e$

each species; negligible effects of radiation; equal exchange coefficients of all species and heat; in cases where buoyancy is important, effects of buoyancy are only considered in the governing equations for mean quantities; and negligible effects of density fluctuations. The first assumption is a condition of all the experiments to be considered. Justification of the remaining assumptions is discussed in the following.

The boundary-layer approximations are well established for forced and buoyant jets and can be adopted with little error. This approach vastly reduces computational requirements so that acceptable numerical accuracy can be achieved with modest computer costs. Another advantage of the boundary-layer flows considered here is that they provide conditions where the simplest and most well-established turbulence models were developed, and where they exhibit their best performance.

Effects of buoyancy must be treated differently for the present experiments and for the other flows considered during the computations. The present flows have relatively-low initial Froude numbers (less than 10^{-6} , see Table 4) and only the near-injector region ($x/d \leq 20$) is of interest; therefore, buoyancy effects can be ignored with little error. This is an important assumption since injection was horizontal so that effects of buoyancy would destroy axisymmetry – vastly increasing the complexity of the flows and the computational requirements needed to predict their properties. Some of the other flows have significant effects of buoyancy, since regions far from the jet exit are considered at times. In these cases, however, buoyancy forces are aligned with the streamwise direction – preserving axisymmetry as well.

Compressibility factors in the equation of state are very close to unity for all conditions encountered during the computations; thus the ideal-gas approximation is appropriate. Test conditions for the present adapted jets involve static temperature variations less than 20 percent, at levels near room temperature, and negligible concentration changes, justifying the use of constant specific heats. Larger temperature variations are encountered when the analysis is used for effective adapted jet conditions; however, assuming constant specific heats is still appropriate in view of the other approximations implied by the effective exit conditions.

For present test conditions, static temperature variations are small and the gas mixture is a very weak radiator so that neglecting radiation is appropriate. Effective adapted jet calculations for other experiments involve more strongly radiating gases and greater static temperature changes, however, these conditions also imply large velocities so that radiative transfer numbers are small and radiation can still be neglected.

The assumption of equal exchange coefficients of all species and heat is widely accepted for the high Reynolds number flows (Re generally greater than 10^4) encountered during present computations (Lockwood and Naguib, 1975; Dash et al., 1978; Faeth, 1983). In fact, laminar transport is negligible in comparison to turbulent transport for all the flows. Since

laminar transport was not important, no attempt was made to treat variations of molecular viscosity, thermal conductivity, etc., due to variations of static temperatures and composition. Room temperature values for a representative mixture were used instead – although the choice had essentially no influence on the results.

In cases where buoyancy is important, effects of buoyancy are ignored in the governing equations for turbulence quantities. This approach has been shown to be effective for predictions of mean properties in strongly buoyant flows, and only results in a slight underestimation of turbulence quantities for local Froude numbers typical of the present flows (Jeng and Faeth, 1984; Lai et al., 1985).

Neglecting effects of density fluctuations is probably the most questionable assumption, although the use of this approximation is widespread for noncombusting jets, even when Mach numbers are high (Dash and Wolf, 1984, 1984a; Dash et al., 1978, 1985, 1986; Sinder and Harsha, 1984; Vatsa et al., 1981, 1982). For the present adapted jets, static temperature changes are less than 20 percent with comparable levels of density changes, while regions where density changes are largest also have relatively low turbulence levels; therefore, density fluctuations are small throughout the flow field and the approximation introduces little error. Potential density fluctuations are greater for computations treating effective adapted jets, but neglecting density fluctuations in these cases seems appropriate in view of the other approximations of this approach. Under this assumption, time (Reynolds) averages and mass-weighted (Favre) averages are the same (Bilger, 1976) and the formulation can be stated in terms of time averages, for consistency with the approach to be used for the underexpanded jets.

3.2 Governing Equations

Under the present assumptions, governing equations must be written for conservation of mass, mean momentum, mean mixture fraction (the fraction of mass which originated at the jet exit), mean stagnation enthalpy, turbulence kinetic energy, the rate of dissipation of turbulence kinetic energy, and the mean-squared mixture fraction fluctuations. Knowledge of the mixture fraction and mixture fraction fluctuations provides a means of finding species concentrations and their fluctuations, through the assumption of equal exchange coefficients of all species and the equation of state of the mixture.

The analysis is formulated in an axisymmetric coordinate system, with x, u and r, v denoting streamwise and radial directions and velocities. In terms of time-averaged quantities, the governing equations can be written in the following general form:

$$r \frac{\partial}{\partial x} (\bar{\rho} \bar{u} \phi) + \frac{\partial}{\partial r} (r \bar{\rho} \bar{v} \phi) = \frac{\partial}{\partial r} (r \mu_{\text{eff}, \phi} \frac{\partial \phi}{\partial r}) + r S_{\phi} \quad (3.1)$$

where $\phi = 1$ (for conservation of mass), \bar{u} , \bar{f} , \bar{H} , k , ϵ or g . The governing equation for \bar{v} was not used for the adapted jets, but will be needed later for the underexpanded jets.

Expressions for $\mu_{\text{eff},\phi}$ and S_ϕ in equation (3.1) are summarized in Table 6, along with the appropriate empirical constants. Aside from the expressions for \bar{H} , the approach used for these quantities follows Lockwood and Naguib (1975), as modified by Jeng and Faeth (1984), after allowing for the fact that time and mass-weighted (Favre) averages are identical under present approximations. The treatment of the \bar{H} equations was drawn from Dash and Wolf (1984, 1984a) and Dash et al. (1978, 1985, 1986), with empirical constants selected to satisfy the assumption of equal exchange coefficients of all species and heat. Terms involving the laminar viscosity, μ , are considered when evaluating μ_{eff} ; however, the effect of these terms was negligible as noted earlier. For present flows, $S_u = 0$, but this term was considered in the form shown for other flows (with the coordinate system aligned along the direction of gravitational acceleration).

The expression for the turbulent viscosity, μ_t , was provisionally extended from earlier work, to treat effects of compressibility at high convective Mach numbers. It is well known that turbulent mixing rates are reduced for supersonic compressible flows in comparison to subsonic flows (Eggers, 1966). As noted earlier, Dash et al. (1975) proposed a compressibility correction to deal with this phenomenon, however, evaluation of this approach was not very encouraging (Dash and Wolf, 1984, 1984a). A somewhat different approach was examined during the present investigation. This involved correcting the expression for the turbulent viscosity, similar to Dash et al. (1975), however, the correction was correlated in terms of the convective Mach number of the turbulent mixing layer as a whole. This choice was motivated by the recent findings of Bogdanoff (1983) and Papamoschou and Roshko (1986), which suggest the importance of the convective Mach number for describing the mixing properties of high-speed turbulent flows. Since the effect follows from the growth rate of large eddies in the mixing layer, it also appears to be appropriate to apply the correction globally across the mixing layer (rather than locally) similar to distortion corrections that have been proposed for axisymmetric flows (Launder et al., 1972).

The compressibility-corrected version of the k - ϵ turbulence model (denoted c.c. in the following) used the following modified expression for the turbulent viscosity

$$\mu_t = \bar{\rho} C_\mu K(M_c) k^2 / \epsilon \quad (3.2)$$

where $K(M_c)$ is the compressibility correction which is taken to be a function of the convective Mach number, M_c , of the mixing layer. The following correlation was used for $K(M_c)$:

$$\begin{aligned} K(M_c) &= 1.00, & M_c < 0.55 \\ K(M_c) &= 2.03 - 1.87 M_c, & 0.55 \leq M_c \leq 0.95 \\ K(M_c) &= 0.25, & 0.95 < M_c \end{aligned} \quad (3.3)$$

Table 6. Summary of Parameters in Governing Equations^a

ϕ	$\mu_{\text{eff},\phi}$	S_ϕ						
1	-----	0						
\bar{u}	$\mu + \mu_t$	$a(\rho_\infty - \bar{\rho})$						
\bar{v}	$(\mu + \mu_t)/\sigma_v$	$-r^{-1}\partial/\partial r(r(p+2\bar{\rho}k/3))$						
\bar{f}	$(\mu/Sc) + (\mu_t/\sigma_f)$	0						
\bar{H}	$(\mu / Pr) + (\mu_t/\sigma_H)$	$r^{-1}\partial/\partial r(r\mu_t(1-\sigma_H^{-1})\partial/\partial r(\bar{u}^2/2))$						
k	$\mu + (\mu_t / \sigma_k)$	$\mu_t(\partial\bar{u}/\partial r)^2 - \bar{\rho}\epsilon$						
ϵ	$\mu + (\mu_t / \sigma_\epsilon)$	$(C_{\epsilon 1}\mu_t(\partial\bar{u}/\partial r)^2 - C_{\epsilon 2}\bar{\rho}\epsilon) \epsilon/k$						
g	$(\mu/Sc) + (\mu_t/\sigma_g)$	$C_{g 1}\mu_t(\partial\bar{f}/\partial r)^2 - C_{g 2}\bar{\rho} g \epsilon/k$						
C_μ	$C_{\epsilon 1}$	$C_{g 1}$	$C_{\epsilon 2} = C_{g 2}$	σ_v	σ_k	σ_ϵ	$\sigma_f = \sigma_H = \sigma_g$	$Sc = Pr$
0.09	1.44	2.8	1.87	3/4	1.0	1.3	0.7	0.7

^a $S_u = 0$ for present adapted jets; $S_u = a(\bar{\rho}_\infty - \bar{\rho})$ for constant-pressure portions of the flow when buoyancy is important; and assumes the form shown in the table for underexpanded jets under the parabolized Navier-Stokes approximation.

The small contribution of laminar transport to \bar{S}_H was neglected, and has been omitted from the table.

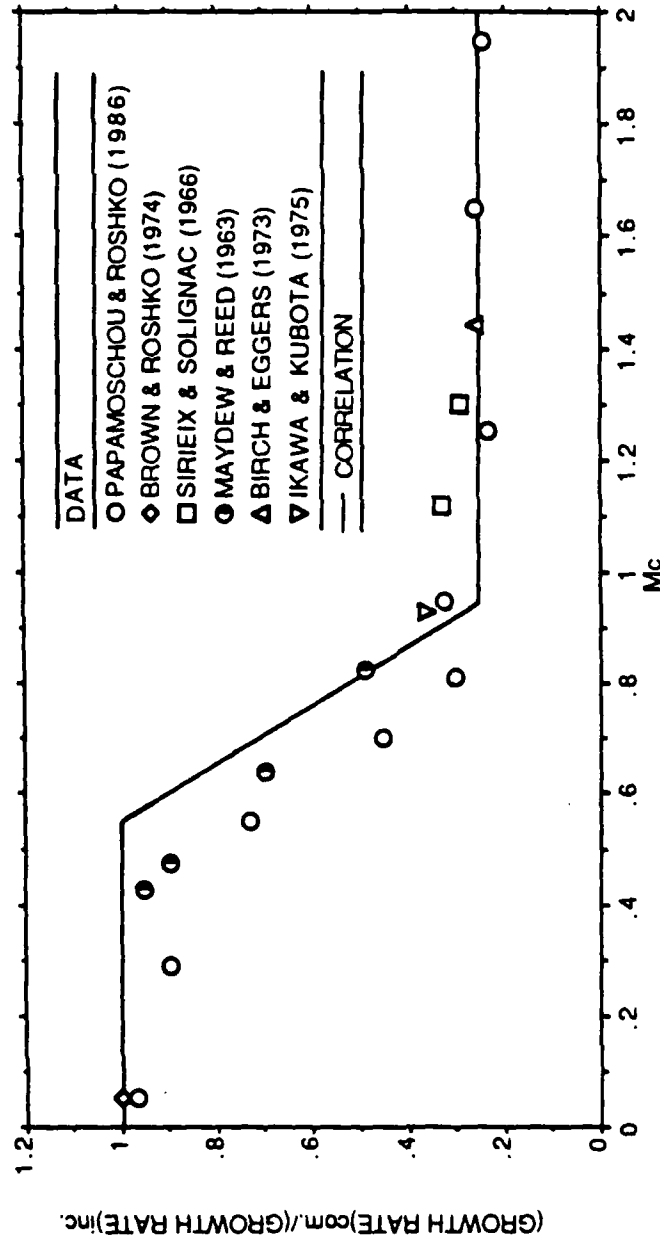


Fig. 18 Turbulent mixing rates for constant-pressure mixing layers as a function of convective Mach number.

where M_c was computed as described by Papamoschou and Roshko (1986).

The form of equation (3.3) was established by plotting measurements of the ratio of compressible to incompressible mixing-layer growth rates as a function of the convective Mach number, similar to Papamoschou and Roshko (1986). This plot appears in Fig. 18. Measurements of constant-pressure mixing layers, with low turbulence levels in the undisturbed streams, due to Papamoschou and Roshko (1986), Maydew and Reed (1963), Sirieux and Solignac (1966), Birch and Eggers (1973), Brown and Roshko (1974) and Ikawa and Kubota (1975) are shown along with the correlation of equation (3.3).

In agreement with a similar plot presented by Papamoschou and Roshko (1986), all the measurements correlate reasonably well as a function of M_c . There is relatively little effect of compressibility on turbulent mixing rates for $M_c < \text{ca. } 0.5$; a sharp reduction of mixing rates for $\text{ca. } 0.5 < M_c < \text{ca. } 1.0$; while for $M_c > \text{ca. } 1.0$, mixing rates remain constant at levels roughly 25 percent of their incompressible values. As shown in Fig. 18, the correlation of equation (3.3) generally reflects these trends. The effect of the proposed compressibility correction will be evaluated in the following, by comparing predictions with and without the correction with available measurements.

3.3 Scalar Properties

Under the assumption of equal exchange coefficients of all species, at the limit where time and mass-weighted averages are the same, the local time-averaged mass fraction of each species is related to the mixture fraction, as follows:

$$\bar{Y}_i = Y_{i\infty} + \bar{f}(Y_{ie} - Y_{i\infty}) \quad (3.4)$$

The mixture molecular weight is then taken to be

$$\bar{W} = (\sum \bar{Y}_i / W_i)^{-1} \quad (3.5)$$

Taking the ambient temperature as the reference condition for enthalpies, the local static temperature, under the boundary layer approximations, becomes:

$$\bar{T} = T_\infty + (\bar{H} - \bar{u}^2 / 2) / C_p \quad (3.6)$$

where

$$C_p = \sum \bar{Y}_i C_{pi} \quad (3.7)$$

The time-averaged density is then given by the ideal gas equation of state, as follows:

$$\bar{p} = p_{\infty} \bar{W} / (R\bar{T}) \quad (3.8)$$

where absolute pressures and temperatures are used in equation (3.8).

3.4 Boundary and Initial Conditions

The boundary conditions for equations (3.1) are that \bar{u} , \bar{f} , \bar{H} , k , ϵ and g are all zero at the edge of the flow, since the surroundings are still and represent the datum states for mixture fraction and enthalpy. Gradients of these quantities are zero along the axis, due to symmetry. This yields

$$r = 0, \quad \partial\phi / \partial r = 0; \quad r \rightarrow \infty, \quad \phi = 0 \quad (3.9)$$

If there is a potential core in the flow, the conditions at $r = 0$ in equations (3.9) are only applied beyond its downstream end. When a potential core is present, properties in the potential core provide the boundary conditions at the inner edge of the surrounding shear layer when equations (3.1) are integrated.

For the present measurements of adapted jets, initial conditions were specified at the jet exit, noting that the passage length was sufficient to provide nearly fully-developed pipe flow at the exit. The approximation of fully-developed pipe flow was confirmed by measurements to be described later. The distribution of \bar{u}_e was obtained from Schlichting (1979) and the distributions of \bar{k}_e and $\bar{\epsilon}_e$ were obtained from Hinze (1975), all at the Reynolds number range of the present experiments, while $\bar{v}_e = 0$. The stagnation temperature of the injected gas was essentially equal to the ambient temperature due to the poor heat transfer properties of the injector passage; therefore, $\bar{H}_e = 0$ based on the chosen enthalpy reference state. By definition, $\bar{f}_e = 1$ and $\bar{g}_e = 0$.

Initial conditions for calculations involving effective adapted jets will be discussed in Section 4. The adapted jet measurements of Shuen et al. (1984) also involved fully-developed pipe flow at the injector exit; therefore, initial conditions were prescribed similar to the present experiments.

The measurements of Becker et al. (1967) and Wygnanski and Fiedler (1969) involved short converging nozzles. This was approximated as slug flow with relatively low turbulence intensities at the jet exit. Initial conditions were prescribed similar to Shuen et al. (1983a), as follows:

$$r \leq 0.495d;$$

$$\bar{u}_e = \text{const.}, \quad \bar{v}_e = \bar{H}_e = g_e = 0, \quad \bar{f}_e = 1 \quad (3.10)$$

$$k_e = (0.02 \bar{u}_e)^2, \quad \epsilon_e = 2.84 \times 10^{-5} \bar{u}_e^3 / d$$

Equations (3.10) provides the inner boundary conditions of the shear layer until it reaches the jet axis. The initial variation of \bar{u} and \bar{f} are taken to be linear in the shear layer, while the other the other properties are found by solving the transport equations under the Couette flow approximation.

3.5 Numerical Computations

The equations were solved using a modified version of the GENMIX algorithm (Spalding, 1977). The computational grid was similar to past work (Jeng and Faeth, 1984) with 33-99 cross-stream grid nodes. Streamwise step sizes were limited to six percent of the current flow width or an entrainment increase of five percent – whichever was smaller. The accuracy of the numerical solution was assessed by comparing the mean mixture fraction flux between the jet exit and the downstream positions. If the differences were greater than 1 percent, the calculation was redone using a finer grid. Overall numerical accuracy was finally assessed by halving all grid sizes for some typical conditions: changes in dependent variables for these checks were also less than 1 percent.

4. THEORETICAL METHODS: UNDEREXPANDED JETS

4.1 Parabolized Navier-Stokes Method

Description of Analysis. Underexpanded jets are far more complicated than adapted jets, since effects of compressibility (shock waves, expansion waves, etc.) must be considered along with the usual problems of treating turbulent mixing. Developing a computer algorithm to deal with these difficulties is a substantial task which was beyond the scope of the present investigation; therefore, only existing methods were considered, as a baseline, in order to highlight needs for additional development of analysis by comparing predictions with the present measurements. Two general approaches were examined, as follows: the parabolized Navier-Stokes approach, embodied by the SCIPVIS computer program of Dash and Wolf (1984, 1984a); and use of effective adapted-jet exit conditions, in conjunction with computations for adapted jets discussed in the previous section.

Compressible flows are an active area of computational fluid dynamics and several methods have recently been reported which could be used to treat underexpanded jets, for

example: Vatsa et al. (1981, 1982), Dash and Wolf (1984, 1984a), and Mikhail et al. (1980) report computations of underexpanded jets in coflow. Mikhail et al. (1980) treat the full Navier-Stokes equations (allowing for streamwise diffusion, recirculation and pressure gradients in all directions), providing a potentially complete treatment of the problem. However, the solution of the full Navier-Stokes equations is computationally intensive, and numerical difficulties have been encountered when turbulence models are used, due to the stiffness of the governing equations for turbulence quantities (Sindir and Harsha, 1984). In contrast, the parabolized Navier-Stokes approach of Dash and Wolf (1984, 1984a) has modest computational requirements, has been stable using a variety of turbulence models, and is available as a well-documented computer code; therefore, this approach was used during the present investigation.

The flows to be considered include the present measurements, as well as several experiments reported by others, e.g., Addy (1981), Birch et al. (1984, 1987), Ewan and Moody (1986), Eggers (1966) and Seiner and Norum (1980), see Table 5. All these flows involve steady injection of air (with trace concentrations of other species, at most) from a round passage, with no swirl, into still air. Since the jets were underexpanded and only the near-injector region was of interest, Froude numbers are low and effects of buoyancy can be neglected with little error. These conditions imply axisymmetric flow and the formulation is posed accordingly.

Several other assumptions are the same as for the analysis of adapted jets: ideal gas mixture with constant specific heats, negligible effects of radiation, equal exchange coefficients of all species and heat, and negligible effects of density fluctuations. As before, present conditions imply no difficulties with the ideal gas approximation. Static temperature variations are greater for underexpanded jets than for adapted jets; however, specific heat variations are still relatively small, as is the radiation number, justifying the assumptions of constant specific heats and negligible effects of radiation. Due to the high Reynolds numbers of the flows, assuming equal exchange coefficients of all species and heat is justified based on past practice (Lockwood and Naguib, 1975; Dash et al., 1978; Faeth, 1983). Neglecting density fluctuations is more questionable since static temperature and pressure variations can be quite large for underexpanded jets. However, the greatest departures of density from ambient values occur in regions where turbulence intensities are relatively small, helping to justify this approximation. Allowing for density fluctuations in compressible flow would also involve a more complex turbulence model, with many parameters poorly defined at this time; therefore, use of the approximation, which is tantamount to extending concepts of incompressible flows directly to compressible flows, will be adopted following Dash and Wolf (1984, 1984a).

Referring to Fig. 5, the SCIPVIS algorithm separates the flow field into a predominantly inviscid shock-cell structure along the axis near the injector (treated as inviscid flow) with viscous shear (mixing) layers growing along the side of the jet and downstream of the triple point (if present). The mixing layers finally merge to the axis in the transitional region. The

treatment of wave and shock processes in the inviscid regions follows the shock-capturing algorithm of Dash and Thorpe (1980). Flows within the mixing layers and the transitional region are quasi-parabolic and are assumed to be approximated by the parabolized Navier-Stokes equations. Somewhat different computational procedures are used in the viscous supersonic and viscous subsonic portions of the flow. The details of the numerical procedures for each region, and methods used to match regions at their boundaries, are discussed by Dash and Wolf (1984, 1984a).

The main limitation of the SCIPVIS algorithm, for present purposes, is that the presence of an inviscid shock-cell region is a key aspect of the organization of the numerical calculations. In contrast, present experiments begin as fully-developed pipe flows and viscous effects are important throughout the shock cell region. It was beyond the scope of the present study to modify SCIPVIS to account for these differences; nevertheless, it is still of interest to exercise the SCIPVIS algorithm for the present flows in order to highlight potential effects of a strongly turbulent flow at the jet exit.

Governing Equations. Under the present assumptions, in conjunction with the quasi-parabolic approximation, governing equations for the viscous regions must be written for conservation of mass, mean momentum in the streamwise direction, mean momentum in the radial direction, mean mixture fraction, mean stagnation enthalpy, turbulence kinetic energy, and the rate of dissipation of turbulence kinetic energy. Concentration fluctuations were not considered, since few mixing measurements in compressible flows have been reported so that the formulation of this equation is not very well established at high Mach numbers.

The governing equations can be placed in the same general form as equation (3.1), where $\phi = 1$ (for conservation of mass), \bar{u} , \bar{v} , \bar{f} , \bar{H} , k and ϵ . The expressions for $\mu_{eff,0}$ and S_0 appearing in equation (3.1) are summarized in Table 6. The main differences between the formulations for adapted and underexpanded jets are that underexpanded jets involve the pressure gradient as a source term in the equation for \bar{u} ; and the presence of a governing equation for \bar{v} , to allow for effects of finite pressure gradients in the r -direction, which is a feature of the quasiparabolic approach.

Methods used to find scalar properties for the underexpanded jets were the same as for the adapted jets. The details of this aspect of the calculations are reported in Section 3.3. The boundary conditions are also the same as for the adapted jets, and are treated in the same manner as slug flows, discussed in Section 3.4. Initial conditions for mean velocity distributions were prescribed at the jet exit, similar to the adapted jets; however, since the near-injector region is assumed to be inviscid in SCIPVIS, turbulence properties are of no consequence at the jet exit, as noted earlier.

Numerical Solution. Specification of the numerical grid, and assessment of numerical accuracy, followed the procedures outlined in Section 3.5. As before, halving the grid size, from the grid used for the results reported here, resulted in less than a one percent change in mixture-fraction distributions.

As noted by Dash and Wolf (1984, 1984a) SCIPVIS cannot handle the formal limit of a still ambient environment: a coflow must be imposed to stabilize the solution algorithm. During initial calculations, it became evident that even the lowest level of co-flow that could be used still influence predictions for the underexpanded jets. This effect is illustrated by the mean mixture fraction predictions for an underexpanded jet (underexpansion ratio of 1.2) illustrated in Fig. 19. Clearly, progressively increasing the coflow velocity causes the mixture fraction profile to be stretched downstream, retarding the rate of mixing.

In order to deal with the coflow problem, all solutions of the parabolized Navier-Stokes equations were carried out for a range of coflow velocities, including the lowest coflow velocity that would still yield a stable solution. This series of results was then extended to zero coflow velocity (a still ambient environment) using Richardson extrapolation. The result of this process is also illustrated in Fig. 19. Fortunately, the results show that the effect of coflow is regular; therefore, errors introduced by the extrapolation are not felt to be large in comparison to other uncertainties of the analysis. Use of results at the lowest coflow where a solution can be obtained, however, can lead to significant underestimation of the rate of flow development near the jet exit.

4.2 Approximate Methods

Divergent-Nozzle Approximation. In order to avoid the complexities of the near-injector region, particularly when properties far from the injector are of interest, several approximate methods involving computations for adapted jets having equivalent initial conditions have been proposed (Kalghati, 1981, 1984; Birch et al., 1984, 1987; Hess et al., 1973; and Gore and Faeth, 1986). Three methods were considered during the present work, as follows: the divergent-nozzle approximation, the pseudo-diameter approximation, and the momentum-velocity approximation.

Kalghati (1981, 1984) and Gore et al. (1986) assumed that the flow at the exit of an underexpanded jet can be approximated by a one-dimensional isentropic divergent nozzle which expands the flow to the ambient pressure. In other words, the underexpanded jet becomes an adapted jet by using the flow conditions at the exit of the hypothetical diverging nozzle as the initial conditions.

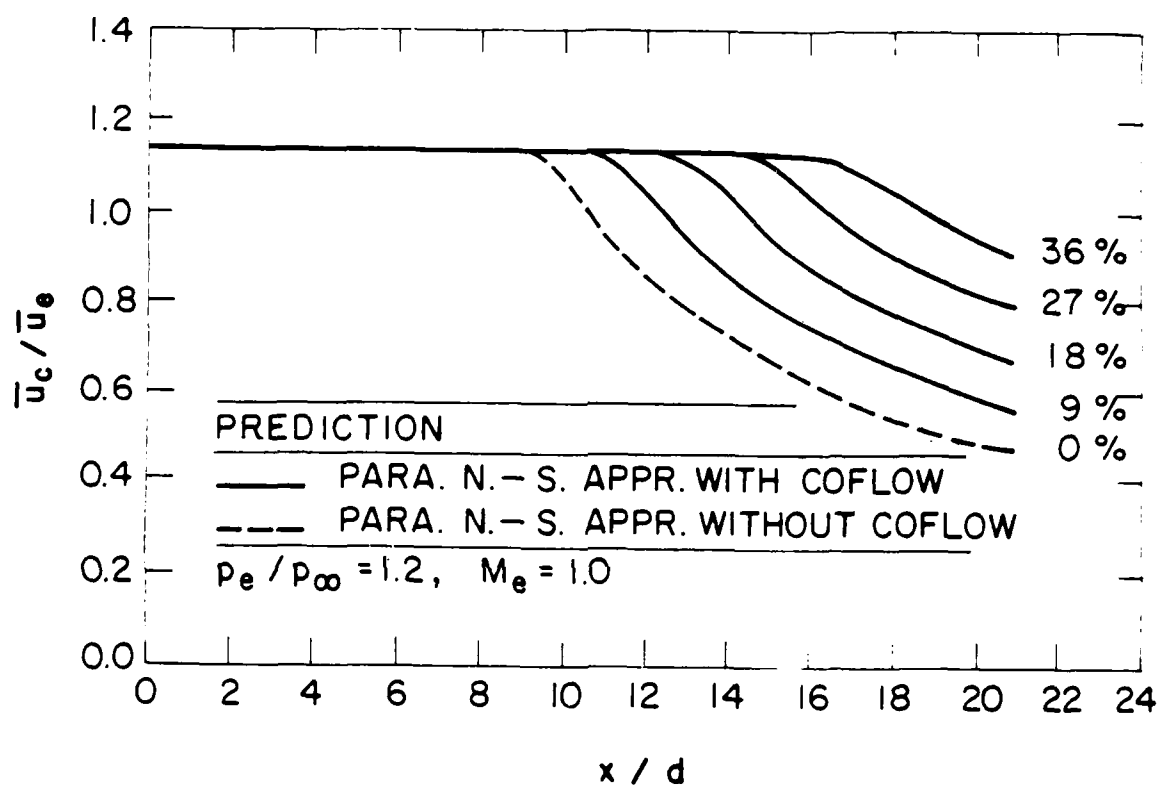


Fig. 19 A typical example of the coflow effect on solutions of the SCIPVIS program.

Figure 20 is an illustration of the hypothetical expansion for the divergent-nozzle method. Properties at the new initial condition, T_{eq} , p_{eq} , etc., can be found in terms of the equivalent exit Mach number, M_{eq} , as follows (Zucrow and Hoffman, 1976):

$$p_o/p_{eq} = (1 + (\gamma-1)M_{eq}^2/2)^{\gamma/(\gamma-1)} \quad (4.1)$$

$$T_o/T_{eq} = 1 + (\gamma-1)M_{eq}^2/2 \quad (4.2)$$

$$\rho_o/\rho_{eq} = (1 + (\gamma-1)M_{eq}^2/2)^{1/(\gamma-1)} \quad (4.3)$$

$$d/d_{eq} = M_{eq}^{1/2} ((2/(\gamma+1))(1 + (\gamma-1)M_{eq}^2/2))^{(\gamma+1)/(4(1-\gamma))} \quad (4.4)$$

Stagnation conditions (p_o , T_o , etc.) in equations (4.1) - (4.4) refer to stagnation conditions at the passage exit, where the flow is assumed to be sonic, while $p_{eq} = p_{\infty}$. Given p_o and p_{eq} , equation (4.1) is solved to find M_{eq} . Then all other average properties at the equivalent initial condition can be found.

In using this approximation, the character of the flow at the equivalent exit condition was assumed to be the same as at the actual passage exit, e.g., either slug flow or fully-developed pipe flow. The equivalent initial conditions were applied at the actual passage exit position, ignoring any displacement to a virtual region. In spite of the crudeness of this approximation, it at least conserves the mass, momentum and energy of the jet as a whole.

Pseudo-Diameter Approximation. The "pseudo-diameter" approximation for under-expanded jets was proposed by Birch et al. (1984). In this method, the equivalent exit area is fixed by the mass flow rate of the flow, while the flow is assumed to have static properties at the ambient temperature and pressure, and has a uniform sonic velocity. In other words, the Mach number of the equivalent flow is unity with static scalar properties fixed at the ambient temperature and pressure.

Under these approximations, the equivalent velocity and density are:

$$u_{eq} = (\gamma R T_{\infty}/W)^{1/2} \quad (4.5)$$

$$\rho_{eq} = Wp_{\infty}/(R T_{\infty}) \quad (4.6)$$

while actual exit conditions are given by

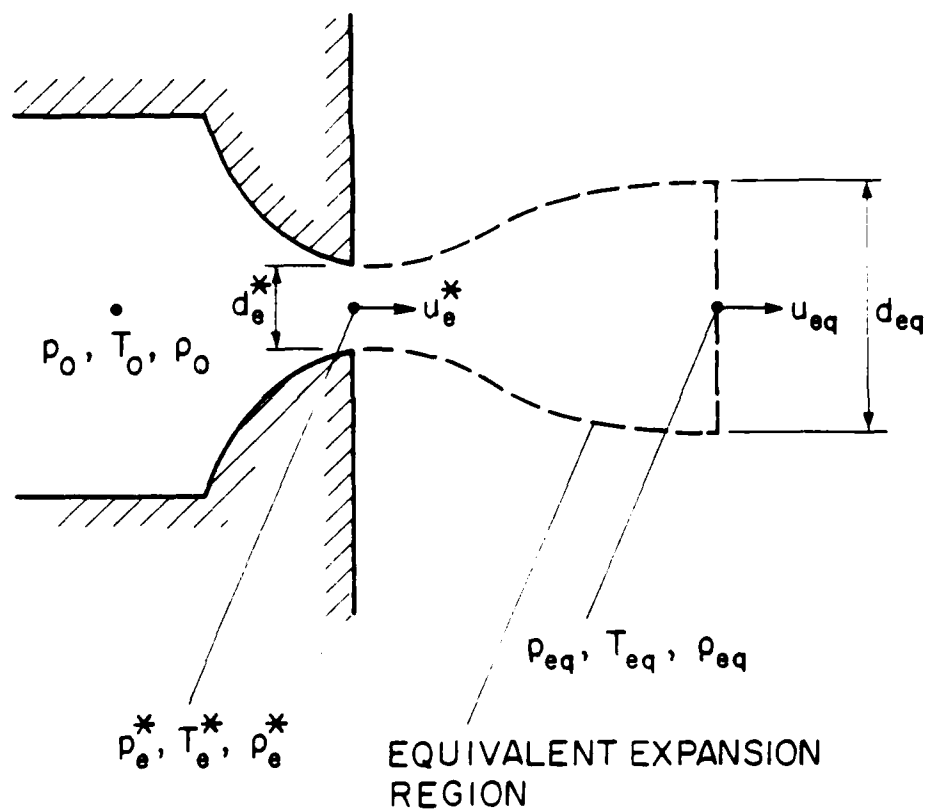


Fig. 20 Schematic of equivalent divergent-nozzle expansion of an underexpanded jet.

$$u_e = (\gamma R T_e / W)^{1/2} = (2\gamma R T_o / (W(\gamma+1)))^{1/2} \quad (4.7)$$

$$\rho_e = \rho_o (2/(\gamma+1))^{1/(\gamma-1)} = (2/(\gamma+1))^{1/(\gamma-1)} \rho_o W / (R T_o) \quad (4.8)$$

The ratio of the pseudo-diameter to the actual diameter is as follows:

$$(d_{eq}/d_e)^2 = \rho_e u_e / (\rho_{eq} u_{eq}) = (2/(\gamma+1))^{(\gamma+1)/(2\gamma-2)} \rho_o / p_\infty \quad (4.9)$$

where the last expression is only true if $T_o = T_\infty$, which was the case for present calculations.

The character of the flow was also preserved when using this approximation. This approach only satisfies conservation of mass of the original flow.

Momentum-Velocity Approximation. In underexpanded jets, the flow parameters change rapidly near the jet exit. Initially, there is an increase in the diameter of the flow, but this is followed by a shock cell and consequent density increase, leading to a reduction of the flow diameter. This process can be repeated a number of times, see Figs. 5 and 6. Furthermore, entrainment rates for supersonic flows are lower than for subsonic flows, tending to inhibit the growth of the jet diameter in the region where shock cells are present (Dash et al., 1975). These observations prompted use of equivalent exit conditions having the same diameter as the passage exit, denoted momentum-velocity approximations (Hess et al., 1973; Gore and Faeth, 1986).

For the momentum-velocity approach, all the excess pressure at the jet exit is applied to increase the momentum of the jet. This yields

$$u_{eq} = u_e + (p_e - p_\infty) / (\rho_e u_e) \quad (4.10)$$

The static temperature is taken to be equal to the ambient temperature, and $d_{eq} = d$. By these choices, the method does not actually preserve any conserved property of the flow – mass, momentum, or energy.

5. RESULTS AND DISCUSSION

5.1 Subsonic Jets

The present experiments included the range of subsonic and underexpanded jets

summarized in Tables 3 and 4. This information was supplemented by the measurements of others which are summarized in Table 5, in order to evaluate methods of predicting these flows. In the following, measured and predicted results for subsonic, sonic and underexpanded jets will be considered in turn.

Initial Conditions. Initial conditions for the subsonic jet, $M_e = 0.3$, are illustrated in Fig. 21. Time-averaged mean and fluctuating concentrations and streamwise velocity fluctuations are plotted in the figure, as a function of radial distance normalized by the nozzle-exit radius. In addition to present measurements, streamwise mean and fluctuating velocities from Shuen et al. (1984) are illustrated on the figure, since they also pertain to exit conditions from a relatively-long constant-diameter passage. In both cases, optical limitations of the LDA prevented measurements exactly at the exit of the nozzle. Present measurements were obtained at $x/d = 0.2$, while those of Shuen et al. (1984) were obtained at $x/d = 1.0$. These nozzle exit conditions should approximate fully-developed pipe flow; therefore, correlations of time-averaged streamwise mean and fluctuating velocities, from Hinze (1975), are also shown on Fig. 21. Furthermore, the mixture fraction is unity, and there are no mixture fraction fluctuations, within the nozzle fluid, by definition: lines representing these definitions have also been drawn on Fig. 21.

In general, the measurements illustrated in Fig. 21 approximate the correlations for fully-developed pipe flow. Exceptions are observed near the edge of the flow, where profiles are broadened due to the development of the shear layer between the passage exit and the streamwise position where the measurements were made. The present measurements of streamwise mean and fluctuating velocities also agree reasonably well with those of Shuen et al. (1984), except that the latter are more broadened near the edge of the flow, since they were obtained somewhat farther from the exit of the passage, i.e., $x/d = 1.0$ as opposed to 0.2 for the present measurements. The uniformity of concentrations near the core of the present flow ($2r/d < 0.8$), and the absence of concentration fluctuations in this region, indicate that mixing of the tracer iodine vapor with the jet flow upstream of the passage exit was adequate.

Properties Along Axis. Predicted and measured mean and fluctuating properties along the axis of the subsonic jet are illustrated in Fig. 22. The results include mean and fluctuating concentrations and streamwise velocities. In addition to the present data, measurements of streamwise mean and fluctuating velocities due to Shuen et al. (1984), for fully-developed pipe flow at the passage exit, are shown on the figures. The predictions pertain only to present test conditions and were found using initial conditions for fully-developed pipe flow, as discussed earlier. In keeping with the isotropic turbulence approximation used in the present turbulence model, the assumption of isotropy was used to estimate \bar{u}' from k , i.e., $\bar{u}'^2 = 2k/3$. If the usual levels of anisotropy observed near the axis of fully-developed jets, $\bar{u}'^2 = k$ (Wynanski and Fiedler, 1969) were used instead, predictions would be roughly 20 percent

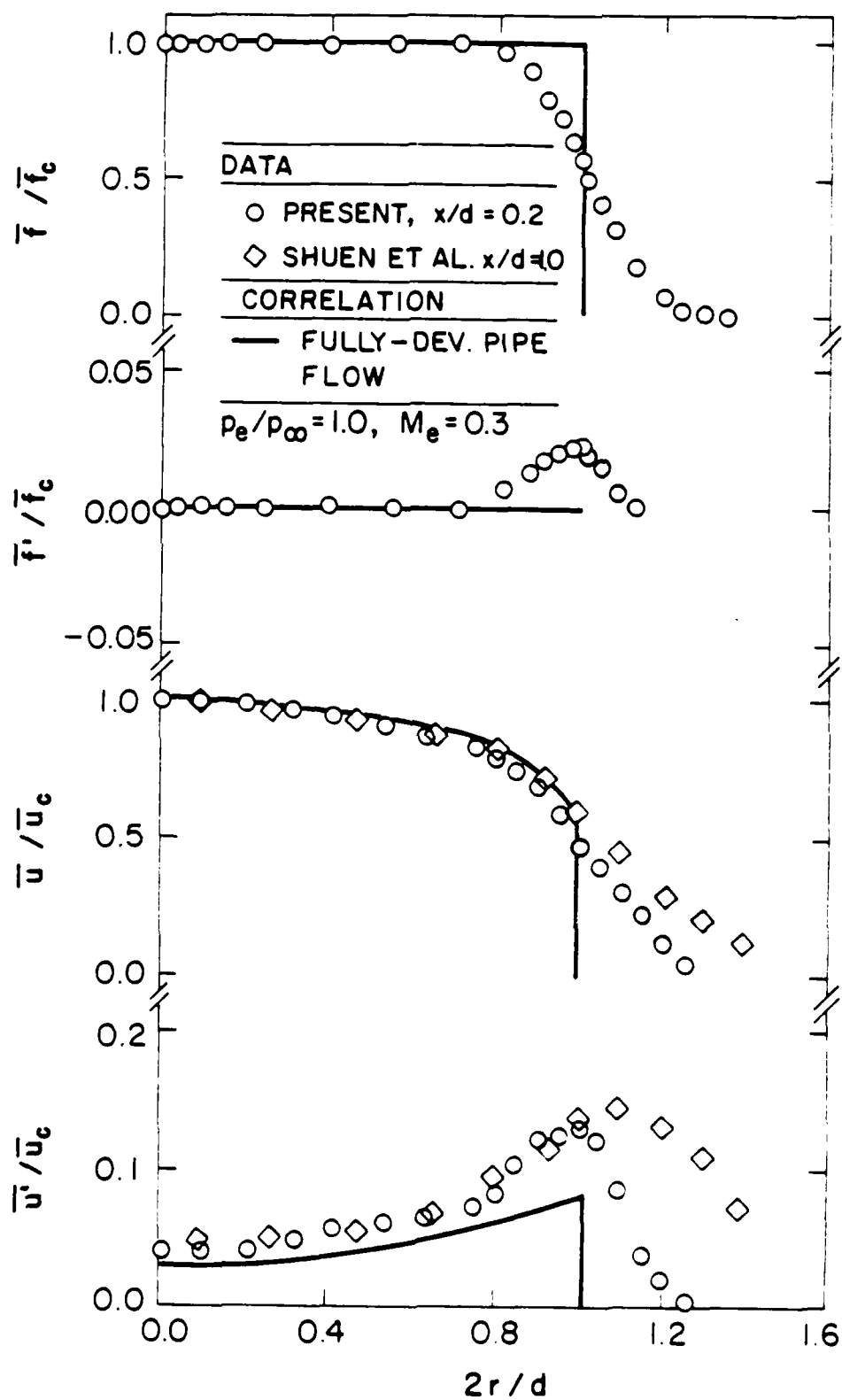


Fig. 21 The initial conditions for the subsonic jet: radial profiles of mean and fluctuating quantities at $x/d = 0.2$.

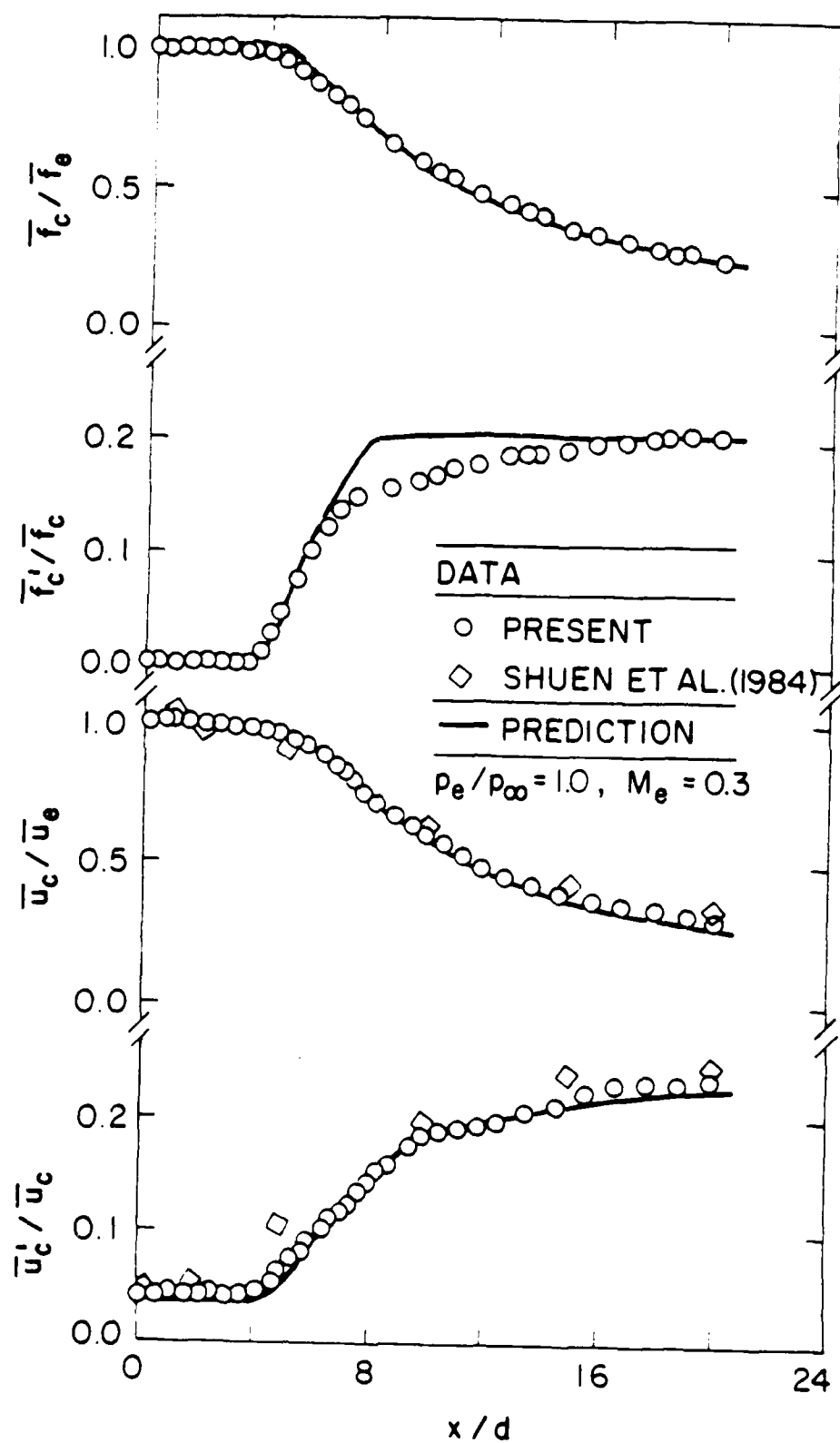


Fig. 22 Axial variation of mean and fluctuating quantities in the subsonic jet.

higher. Present measurements are in the near-injector region, where the flow is still developing; therefore, it is likely that actual levels of anisotropy in the flow are between these limits.

Present measurements of streamwise mean and fluctuating velocities generally agree with the findings of Shuen et al. (1984) within experimental uncertainties. Similar to the findings of Shuen et al. (1984), using the same turbulence model, predictions are in reasonably good agreement with measurements of streamwise mean and fluctuating velocities. Although predictions were obtained for present test conditions, predictions based on the initial conditions of Shuen et al. (1984) are virtually the same, as are the measurements for the two subsonic jet experiments. This agrees with the well-known independence of flow properties on Reynolds number for a particular initial condition, when normalized in the manner of Fig. 22.

Present results extend past findings to also consider predictions and measurements of fluctuating concentrations in Fig. 22. The agreement between predictions and measurements is reasonably good; however, there are significant discrepancies between predictions and measurements of concentration fluctuations for $8 < x/d < 16$, which follows the region where concentration fluctuations rapidly increase, just downstream of the potential-core. This could be due to a defect of the model, since boundary-layer approximations become questionable when flow properties change rapidly in the streamwise direction. Even this discrepancy, however, is not large in view of experimental uncertainties. In general, the results provide a reasonable baseline for the analysis, consistent with past evaluations of the present approach for constant and variable-density round jets (Jeng and Faeth, 1984).

The results illustrated in Fig. 22 demonstrate the importance of conditions at the passage exit in determining the properties of the near-field region of jets. For fully-developed pipe flow, the flow near the axis is always turbulent and a potential core is not present in the usual sense. However, transition from pipe flow to more jet-like properties does result in a region where properties don't vary very much along the axis and have a potential-core character. This region extends to $x/d \sim 4$ for the results illustrated in Fig. 22. In contrast, measurements of jet properties for slug-flow initial conditions indicate potential core lengths of roughly $x/d \sim 8$ (Wyganski and Fiedler, 1969). Similarly, measurements downstream of the potential core exhibit lower degrees of overall mixing (higher mixture fractions) at particular streamwise positions for slug flows (Becker et al., 1967), than the present results for fully-developed pipe flow at the passage exit. This behavior results from the shorter potential core in the present case, which increases the relative degree of mixing at every axial station. Another effect of jet exit conditions is that concentration fluctuation intensities increase at a faster rate than velocity fluctuation intensities downstream of the potential-core-like region. This is caused by the fact that concentration fluctuations are formally zero at the jet exit, while velocity fluctuations are rather large at the jet exit (representative of fully-developed pipe flows). It is encouraging that predictions represent these differences reasonably well.

Radial Profiles. The radial variations of flow properties for the subsonic jet, at $x/d = 5$, 10 and 20, are illustrated in Figs. 23-25. Mean and fluctuating concentrations and streamwise velocities, normalized by the mean concentration and the mean velocity at the axis, respectively, are plotted as a function of r/x , which is the similarity variable for fully-developed turbulent jets. The predictions are based on fully-developed pipe flow at the passage exit, as noted earlier.

Predictions and measurements of mean concentrations and streamwise velocities, illustrated in Figs. 23-25, are in reasonably good agreement. Flow near the passage exit, $x/d = 5$, is still developing, since radial profiles extend to $r/x \sim 0.25$, rather than $r/x \sim 0.15-0.20$ which is associated with fully-developed jets (Wyganski and Fiedler, 1969). However, flow widths at $x/d = 10$ and 20, particularly the latter, have already approached widths in terms of r/x which are representative of similarity conditions far from the injector (Wyganski and Fiedler, 1969). This relatively rapid development of the flow is due to the fully-developed pipe flow initial condition, which provides a reasonably strong turbulent flow, and a potential for rapid mixing, right at the jet exit. In contrast, slug flow initial conditions, with low turbulence levels, defers much of the development of the flow to the end of the potential core, ca. $x/d = 8$. The fact that the end of the potential core-like region is reached near $x/d \sim 4$, see Fig. 22 is also indicated by the rounded shape of the mean concentration and streamwise profiles near the axis, with no evidence of a constant-property unmixed region at the core of the flow, at $x/d = 5$.

The comparison between the predicted and measured velocity fluctuations illustrated in Figs. 23-25 is reasonably good, well within theoretical uncertainties due to the varying anisotropy of the flow, and experimental uncertainties. This level of performance is typical of past experience with the present analysis for a variety of low Mach number jets (Jeng and Faeth, 1984; Shuen et al., 1984). However, the comparison between predicted and measured concentration fluctuations is not as good, particularly at $x/d = 5$ and 10 where predictions overestimate the measurements significantly. This difficulty may be related to the strong streamwise variation of concentration fluctuations along the axis in this region, discussed in connection with Fig. 22. Such rapid streamwise changes, which exceed those observed for velocity fluctuations, raise questions concerning the appropriateness of the boundary-layer approximations in this region. This view is supported by the improved comparison between predicted and measured concentration fluctuations at $x/d = 20$, seen in Fig. 25, which corresponds to a region where the streamwise variation of concentration fluctuations is much smaller than for x/d in the range 5-10, see Fig. 22.

Shuen et al. (1984) also report measurements at $x/d = 20$, for fully-developed pipe flow initial conditions, which are plotted in Fig. 25 for comparison with present results. Furthermore, radial plots of properties at $x/d = 20$, when normalized in the manner of Figs. 23-25, become relatively independent of initial conditions (whether slug or fully-developed flow), the initial density variations of the flow, and the value of x/d , i.e., similarity conditions

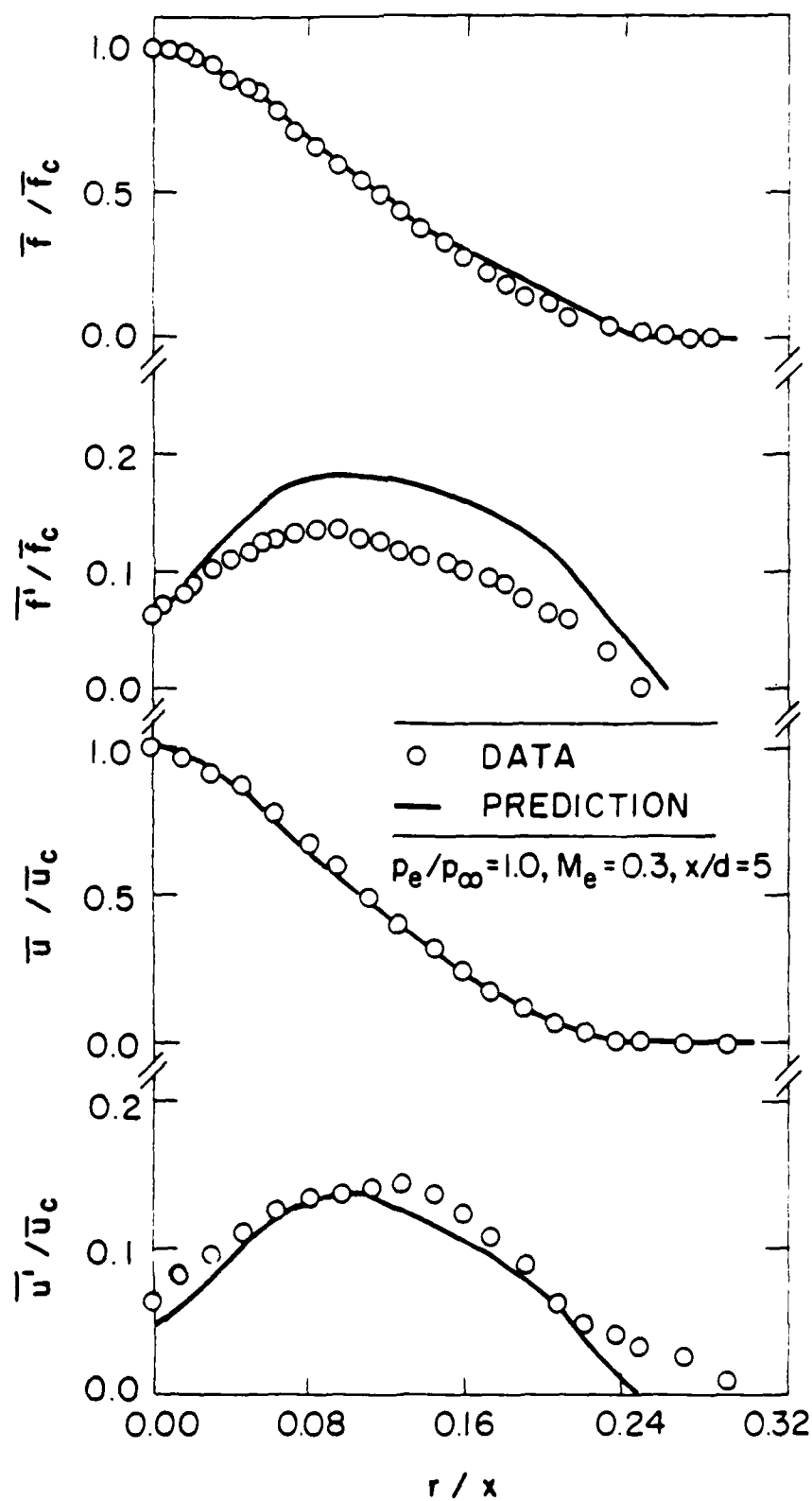


Fig. 23 Radial variation of mean and fluctuating quantities in the subsonic jet at $x/d = 5$.

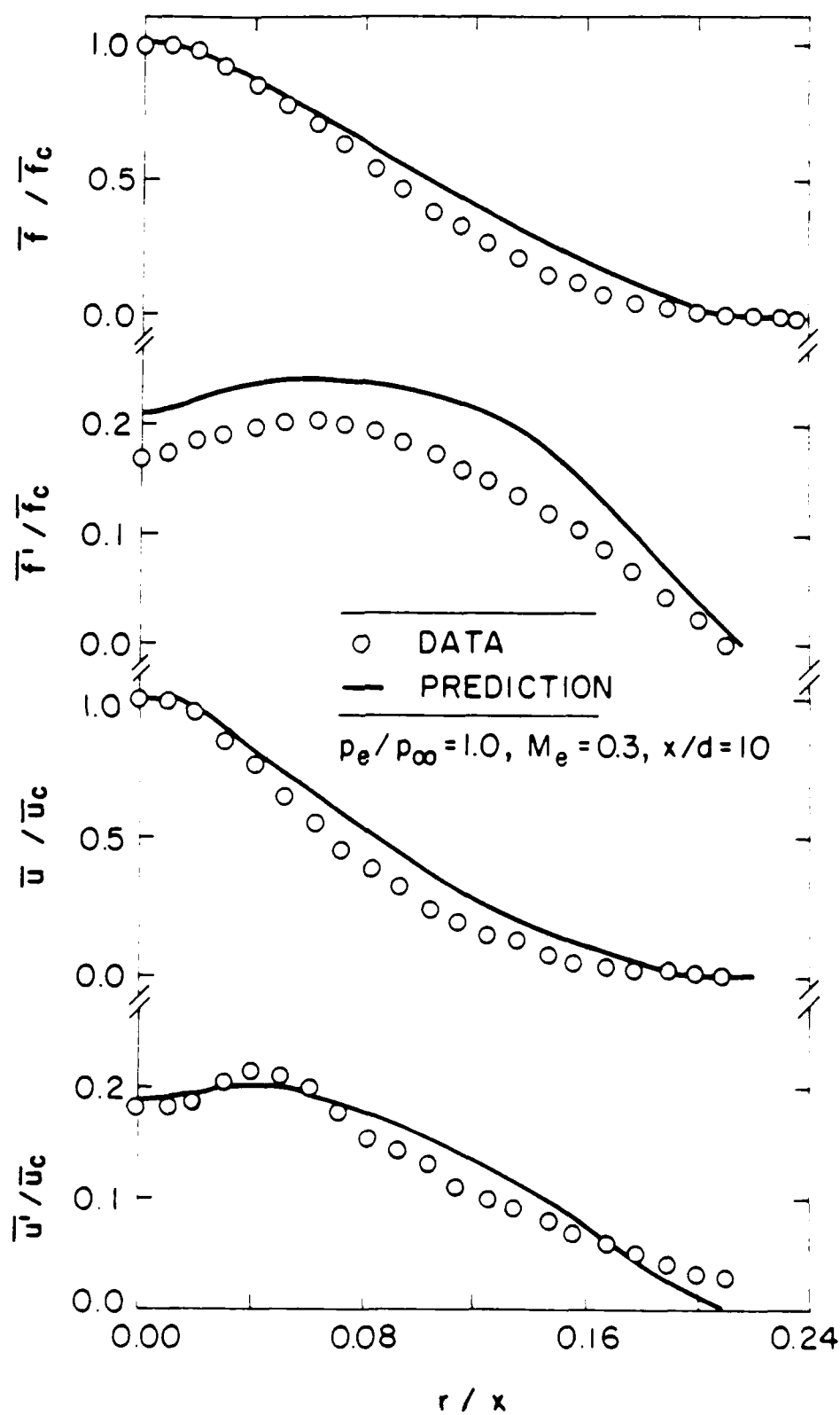


Fig. 24 Radial variation of mean and fluctuating quantities in the subsonic jet at $x/d = 10$.

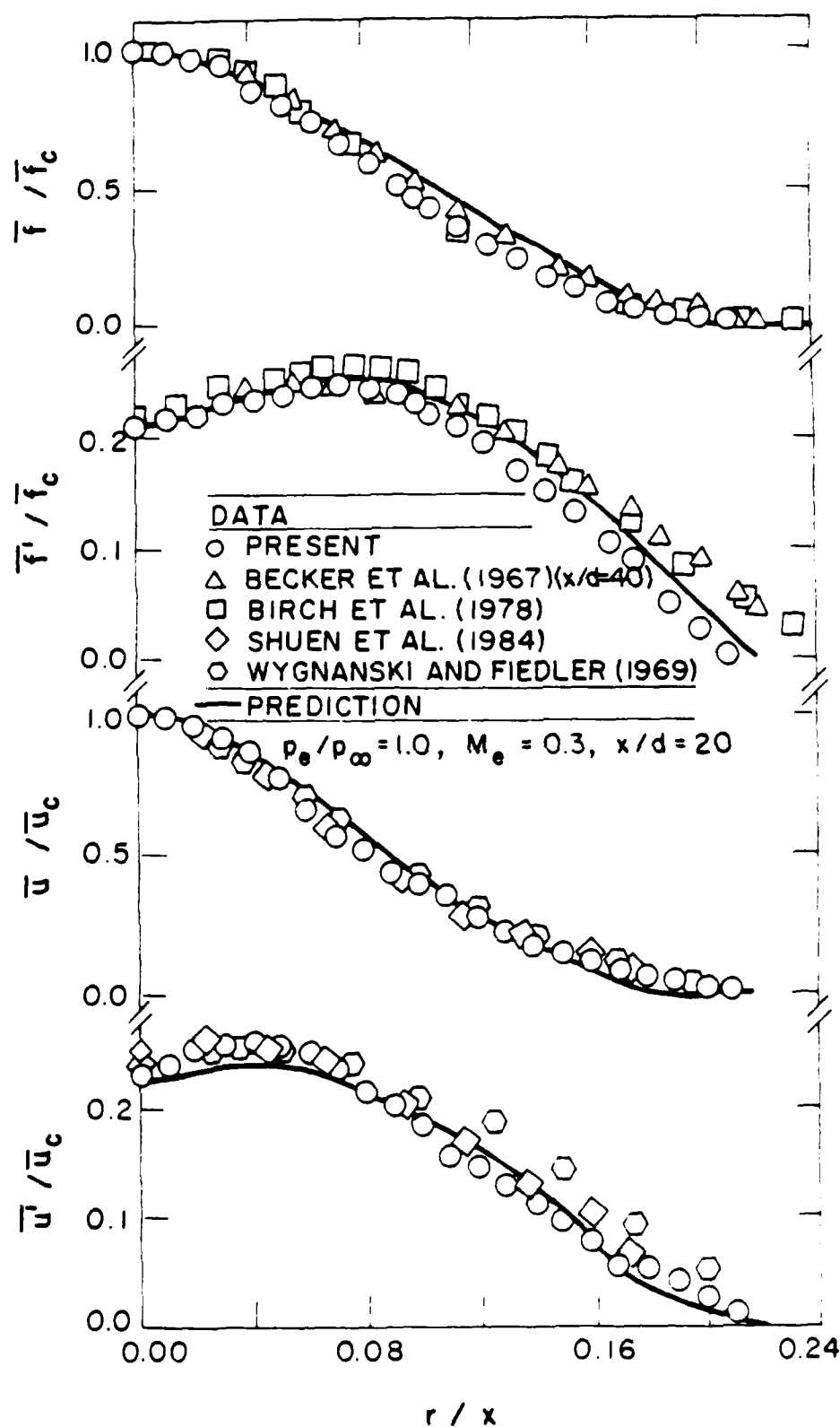


Fig. 25 Radial variation of mean and fluctuating quantities in the subsonic jet at $x/d = 20$.

are approached. Thus, several other sets of measurements are plotted in Fig. 25 as well. This includes results of Becker et al. (1967) for an air jet at $x/d = 40$, with a slug flow initial condition; results of Birch et al. (1978) for a methane jet injected into still air for a fully-developed pipe flow initial condition; and results of Wygnanski and Fiedler (1969) for an air jet with a slug flow initial condition. Mean properties of all these measurements agree reasonably well with the present measurements, and the predictions. The velocity fluctuation measurements of Shuen et al. (1984), also made with an LDA, similarly agree quite well with present measurements and predictions. However, the velocity fluctuation measurements of Wygnanski and Fiedler (1969) are higher than present results and those of Shuen et al. (1984) near the edge of the flow. This behavior is probably due to difficulties encountered with the interpretation of hot wire measurements, the approach used by Wygnanski and Fiedler (1969), in the edge region of jets where turbulence intensities are high. The concentration fluctuation measurements of Becker et al. (1967) and Birch et al. (1978) are also higher than present measurements near the edge of the flow. This is expected for the particle-scattering approach used by Becker et al. (1967), since shot noise is difficult to control in regions where particle concentrations are low and this effect tends to increase apparent concentration fluctuation levels. Birch et al. (1978) use Raman scattering for their measurements and shot noise should not be a problem. Present signal-to-noise ratios in this region are quite good, as discussed earlier. Information on signal-to-noise ratios was not provided by Birch et al. (1978), and low signal-to-noise ratios for their measurements might explain the discrepancy; however, further study will be needed to resolve the differences between the findings of Birch et al. (1978) and the present investigation.

5.2 Sonic Jet

Initial Conditions. Initial conditions for the adapted sonic jet are illustrated in Fig. 26. This condition has not been considered by others; therefore, only present measurements are compared with the correlations for fully-developed pipe flow. The results are qualitatively the same as for the subsonic jet, illustrated in Fig. 21. One curious aspect of the results is that normalized velocity fluctuations are somewhat higher in the shear layer for sonic flow than for subsonic flow. It will be shown subsequently that this trend will continue with additional exit-plane pressure increases for underexpanded jets, suggesting that the present sonic flow might be slightly underexpanded (since properties across the exit are not uniform, defining the sonic state is somewhat subjective).

Properties Along Axis. Predictions and measurements of mean and fluctuating concentrations and streamwise velocities along the axis of the sonic jet are illustrated in Fig. 27. The comparison between predictions and measurements is similar to the subsonic jet illustrated in Fig. 22. The analysis correctly represents the increase in the length of the potential core and slower mixing rates of the sonic jet, in comparison to the subsonic jet. This is an effect of the increased initial density of the sonic jet since it has a lower temperature due to a greater degree of expansion in the passage. This requires additional mixing with the

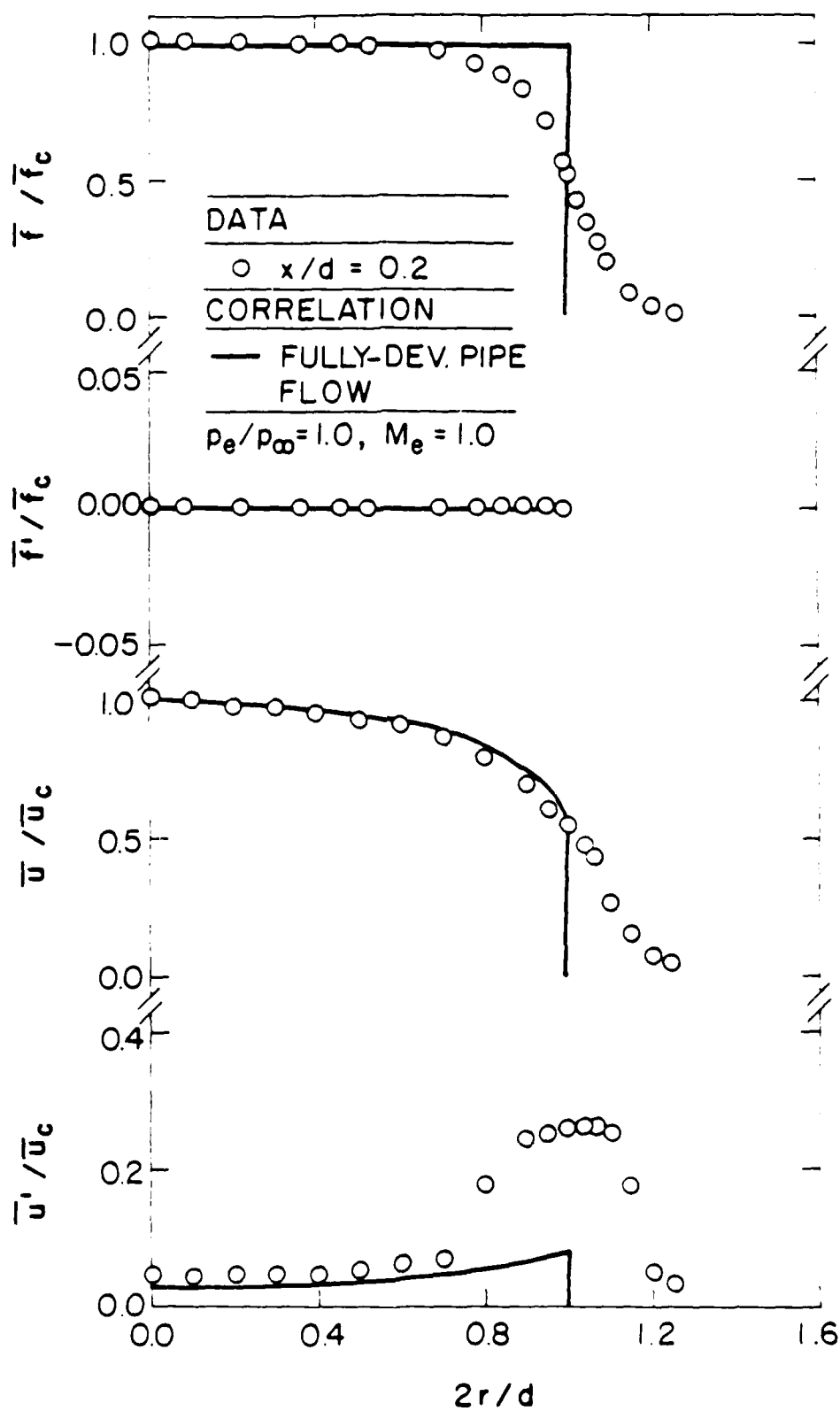


Fig. 26 The initial conditions for the sonic jet: radial profiles of mean and fluctuating quantities at $x/d = 0.2$.

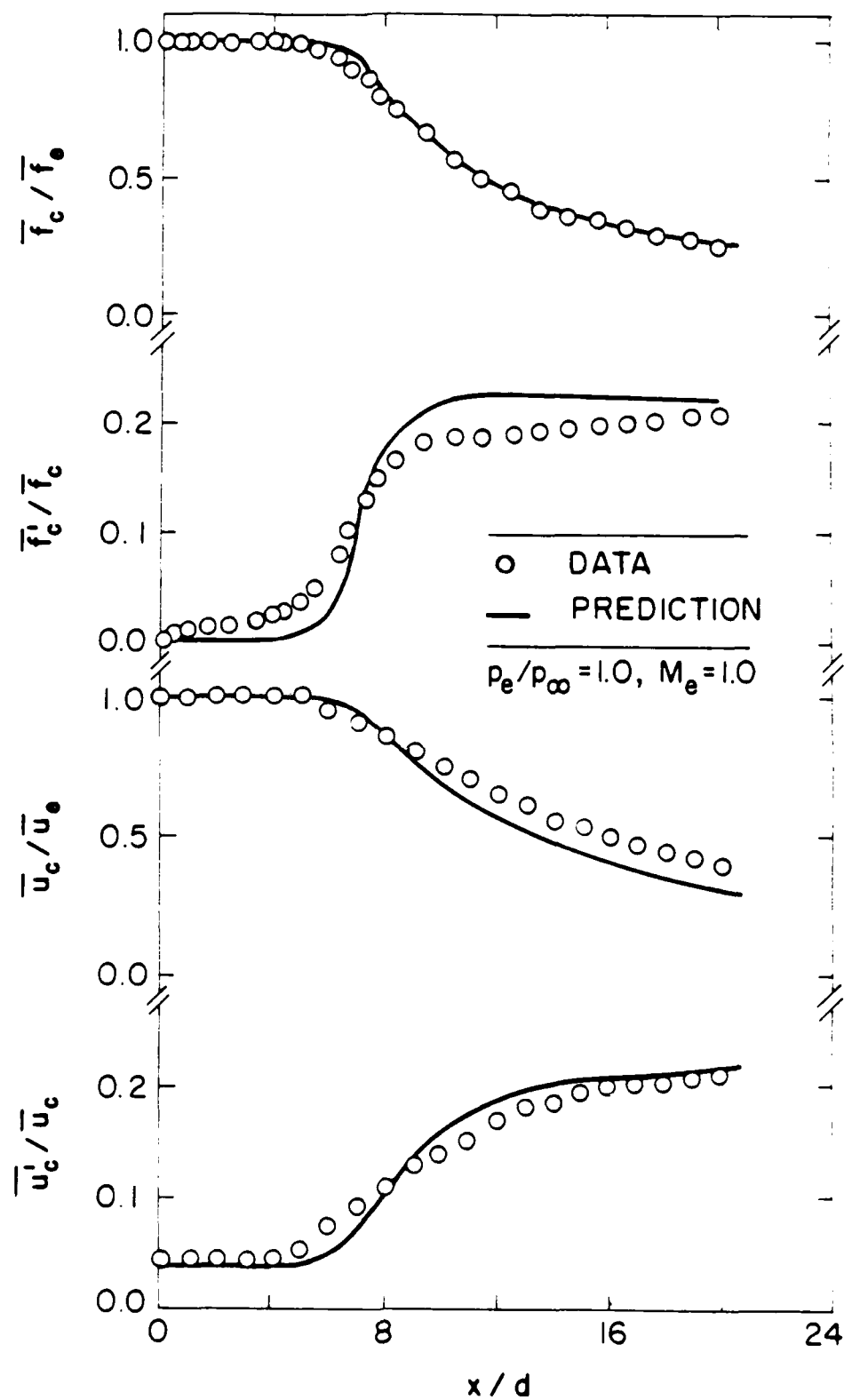


Fig. 27 Axial variation of mean and fluctuating quantities in the sonic jet.

surrounding gas in order to achieve the same scalar and dynamical state. Past comparison of measurements and predictions for variable density round jets exhibit this behavior to a greater degree, when jets having large density variations are considered (Faeth, 1983). The present analysis was also able to treat these larger density variations successfully; thus, the agreement seen in Fig. 27 is perhaps not surprising. The additional feature examined here, however, involves use of the stagnation enthalpy equation and consideration of kinetic energy in the mean: the results illustrated in Fig. 27 suggest that these aspects of the analysis are performing satisfactorily.

Radial Profiles. Predictions and measurements of the variation of flow properties in the radial direction for the sonic jet are illustrated in Figs. 28-30. The coordinates of these plots, and the spatial locations considered, are the same as for the subsonic jet, illustrated in Figs. 23-25. The comparison between predicted and measured mean properties is similar to findings for the subsonic jet, suggesting little deterioration of the analysis as the density variation and Mach numbers increase, for subsonic flow. Predictions of streamwise velocity fluctuations are also reasonably good, in view of uncertainties in the degree of anisotropy of the flow and experimental uncertainties. Predictions of streamwise velocity fluctuations are somewhat worse at $x/d = 5$ than at other locations. This position, however, is just downstream of the potential core where fluctuating velocities vary rapidly in the streamwise direction, and predictions become rather sensitive to streamwise location. This also corresponds to the position where predicted fluctuating velocities at the axis are in worst agreement with measurements, see Fig. 27.

Predicted and measured concentration fluctuations are in poorest agreement for the sonic jet, for the results illustrated in Figs. 28-30. Predicted profiles of concentration fluctuations are narrower for the sonic than for the subsonic jet, reflecting the somewhat larger jet exit density of the former flow, which reduces relative rates of turbulent mixing in the radial direction. However, the measurements indicate a larger reduction of width in going from subsonic to sonic flow, contributing to the relatively large discrepancies seen between predictions and measurements near the edge of the flow. One possible reason for this behavior is that the sonic flow may in fact be slightly underexpanded, as noted earlier, so that the compressible wave field could modify mixing properties in ways that are not considered in the present analysis. Another problem might be the relatively crude treatment of scalar properties, represented by equations (3.4)-(3.8), which ignores the correlation between H and f . This type of difficulty will become more problematical as Mach numbers of the flow increase, and represents an area of the analysis which should be given more study. Finally, the somewhat poorer results at $x/d = 5$ and 10 could be due to the rapid changes of concentration fluctuations in this region, raising questions concerning use of the boundary-layer approximations, as noted earlier. The fact that predictions of all properties improve at $x/d = 20$, where effects of compressibility, variable densities, and rapid streamwise development of the flow become small, suggests that all these factors contribute to discrepancies between predictions and measurements in the near-field portion of the flow.

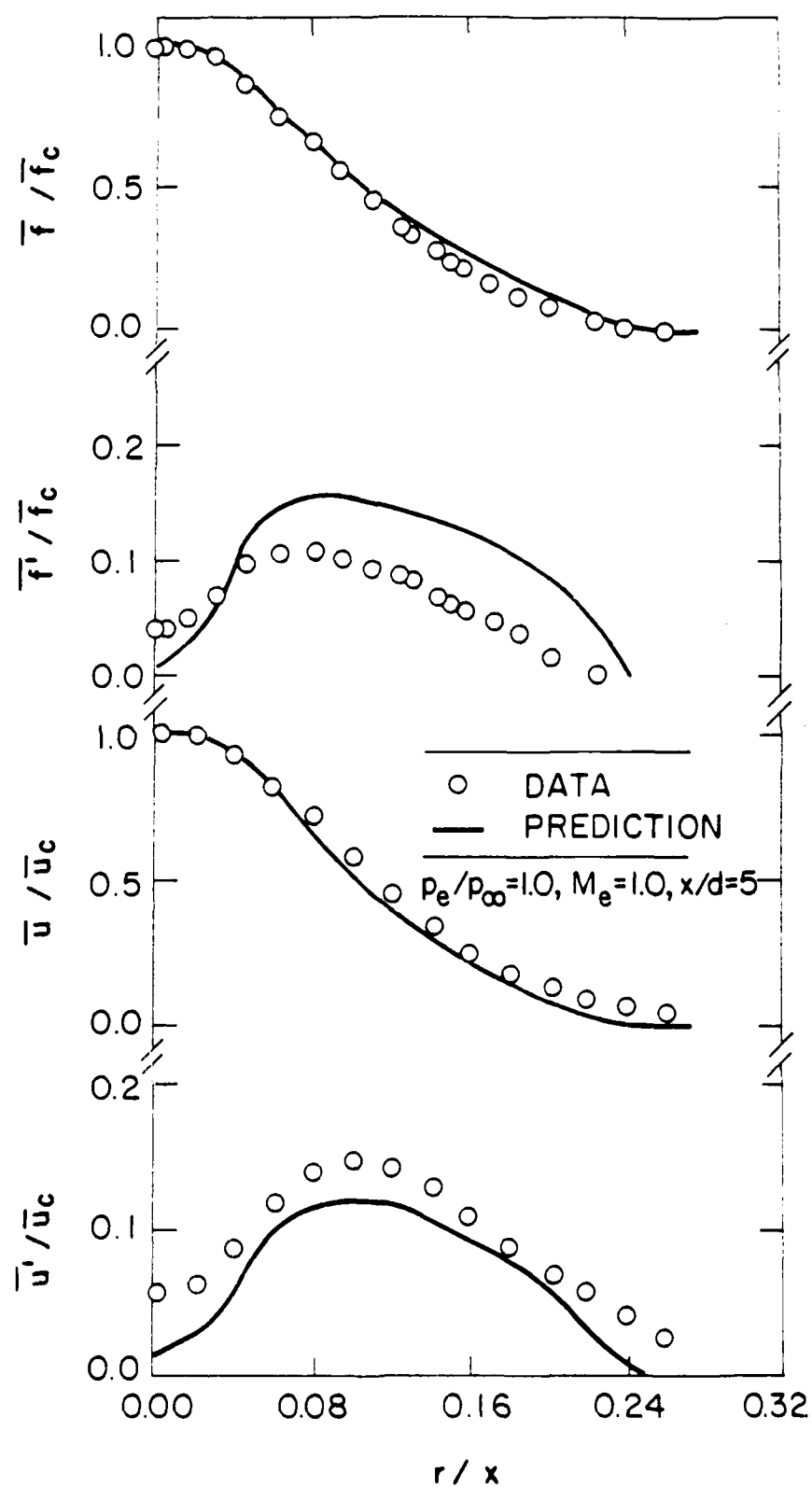


Fig. 28 Radial variation of mean and fluctuating quantities in the sonic jet at $x/d = 5$.

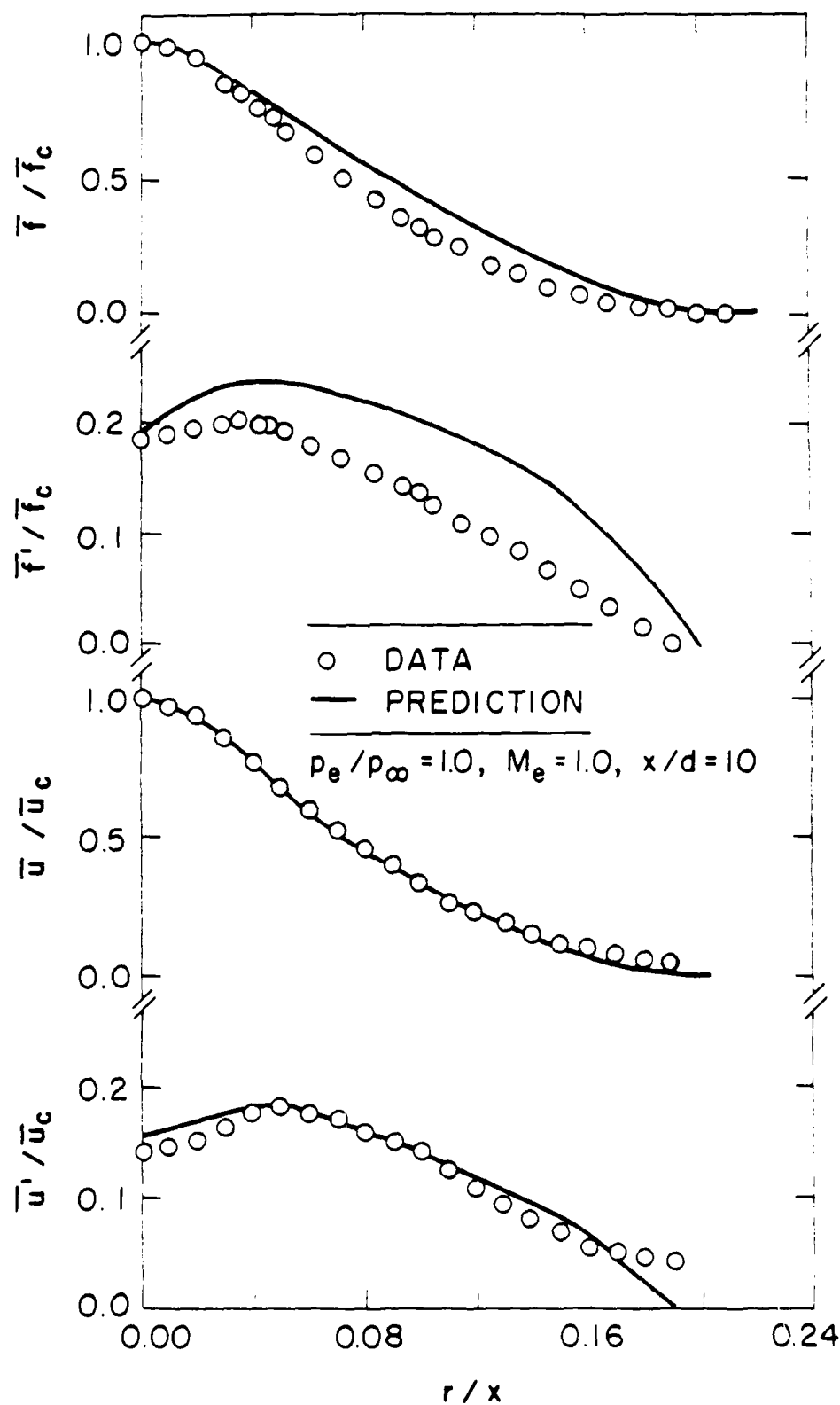


Fig. 29 Radial variation of mean and fluctuating quantities in the sonic jet at $x/d = 10$.

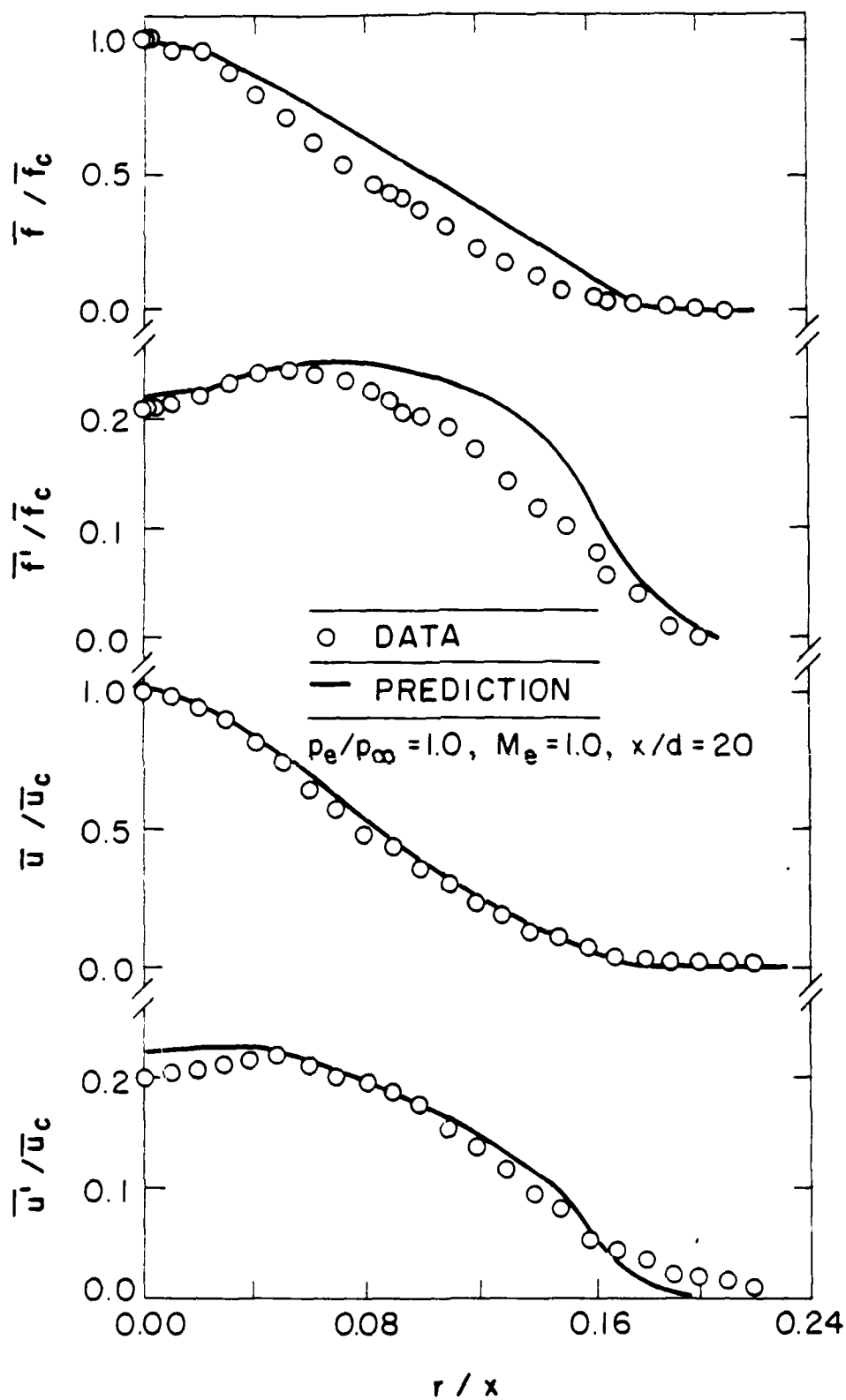


Fig. 30 Radial variation of mean and fluctuating quantities in the sonic jet at $x/d = 20$.

5.3 Supersonic Jets: Slug Flow

Both underexpanded and adapted supersonic jets, having slug flow exit conditions, will be considered first, prior to dealing with the additional problems of fully-developed flow at the jet exit for the present measurements. Results to be considered include the measurements of Birch et al. (1984, 1987), Seiner and Norum (1979, 1980) and Eggers (1966).

Predictions and measurements for the results of Birch et al. (1984, 1987) are illustrated in Fig. 31. Two jets were studied by Birch et al. (1984, 1987): natural gas injected into still air, to study mixing; and air injected into still air, to study velocities. The flows were produced using a converging nozzle, with a sonic velocity slug flow and an underexpansion ratio of 1.9 at the nozzle exit. Convective Mach numbers for these flows were 0.77 and 0.65, while the measurements were limited to $x/d > 20$; therefore, effects of compressibility were not large in the region where measurements were made.

Predictions based on the divergent-nozzle approximation, with (denoted c.c.) and without the compressibility correction, are illustrated for both jets in Fig. 31. The other two approximate methods, the pseudo-diameter and the momentum-velocity methods, gave nearly the same results as the divergent-nozzle approximation for all calculations considered during this investigation; therefore, only the latter approach will be illustrated in this report. Parabolized Navier-Stokes predictions, using the SCIPVIS algorithm and with (denoted c.c.) and without the compressibility correction, are limited to the air jet in Fig. 31. The SCIPVIS calculations give rapid mean velocity fluctuations in the shock-wave-containing region near the jet exit, which cannot be resolved on the scale of Fig. 31; therefore, only averages of these mean velocity fluctuations along the axis are shown. Velocities computed using the divergent-nozzle approximation do not fluctuate and are plotted directly on the figure: these velocities are higher than the jet exit velocity due to the effective expansion process between the jet exit and ambient pressures.

All the mean velocity predictions illustrated in Fig. 31 agree reasonably well with each other and with the measurements. However, this evaluation is not very definitive since the measurements correspond to the slug flow exit conditions, which are appropriate for SCIPVIS; the convective Mach numbers are low so that compressibility should not have a large effect on mixing; and the measurements are far from the jet exit, reducing effects of errors in the near-field region. Use of the divergent-nozzle approximation is similarly successful for mean concentrations along the axis, but with the same limitations. While effects of compressibility are not large for the results illustrated in Fig. 31, they can still be seen in the predictions. The lower values of K for $M_c > 0.55$ cause the compressibility-corrected predictions to trail the baseline predictions, extending the length of the potential core region slightly.

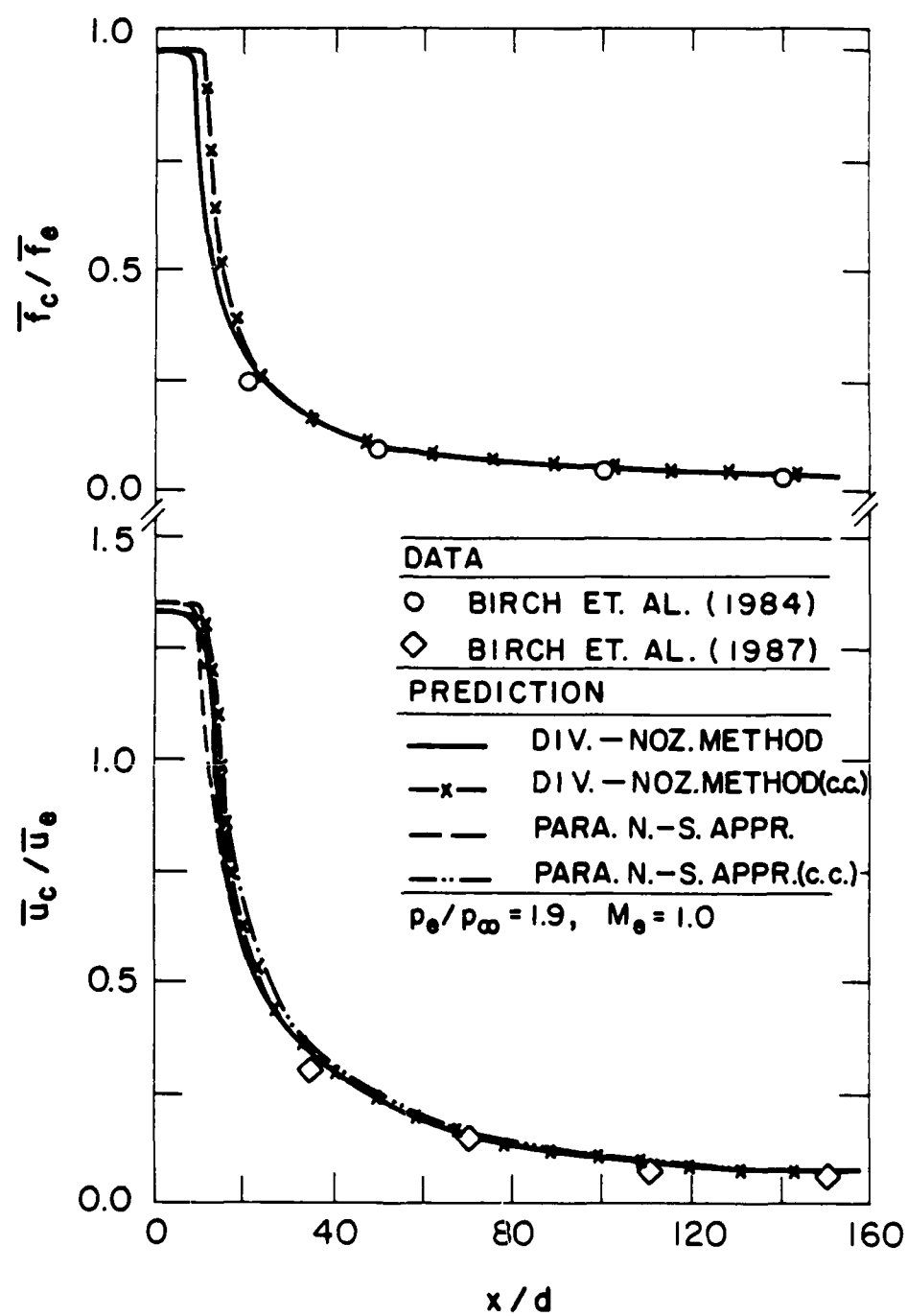


Fig. 31 Axial variation of mean velocities and concentrations in underexpanded gas jets ($p_\theta / p_\infty = 1.9$, $M_\theta = 1.0$).

The mean static pressure measurements along the axis of an underexpanded supersonic jet, due to Seiner and Norum (1980), are illustrated in Fig. 32. Test conditions involved a cold ($T_e = 164$ K) Mach 2 jet injected into still air with an underexpansion ratio of 1.45. Predictions using the SCIPVIS algorithm, both with and without the compressibility correction, are also shown on the figure. Both predictions and measurements exhibit the decaying oscillatory static pressure variation in the near-field region, caused by the interaction between the shock cells and the growing mixing layers near the edge of the flow. All predictions and the measurements agree quite well for the first few shock cells, where the flow is largely inviscid: similar behavior was observed by Dash et al. (1985) using slightly different turbulence models. Farther downstream, however, predictions using the baseline turbulence model underestimate the wavelength of the pressure oscillations, and overestimate their rate of decay in the streamwise direction. This is caused by overestimation of the rate of growth of the shear layers near the edge of the flow, which is reduced due to the high convective Mach number of this flow, 0.94. This is shown by the improved predictions of the compressibility-corrected version of the turbulent model, both with respect to the wavelength and amplitudes of the pressure oscillations far from the injector. These results suggest that the reduced rates of mixing for the Seiner and Norum (1980) measurements are consistent with the measurements of constant-pressure high convective Mach number measurements used to develop the correlation of equations (3.2) and (3.3).

Results for the measurements of Eggers (1966) are illustrated in Fig. 33. Mean velocities were measured along the axis of an adapted jet produced by a convergent/divergent nozzle injected into still air with slug flow exit conditions and an exit Mach number of 2.2. Predictions include the divergent-nozzle and parabolized Navier-Stokes methods, both with and without the compressibility correction. The convective Mach number of this flow is 0.92; therefore, effects of compressibility should be important according to the results illustrated in Fig. 18 and correlated by equations (3.2) and (3.3). This is reflected by the longer length of the potential core for predictions using the compressibility correction (nearly a 2:1 increase in the predicted length of the potential core). Since the flow is adapted, predictions using the parabolized Navier-Stokes and divergent-nozzle methods should be the same, since they both use the same turbulence models. Small differences between the predictions are due to differences in the numerical solutions using the GENMIX and SCIPVIS algorithms: particularly the need to extrapolate to zero coflow when using the latter method.

Comparing predictions and measurements in Fig. 33 indicates that use of the compressibility correction yields the best results for the subsonic portion of the flow, $\bar{u}_c/\bar{u}_e < 0.5$, where uncertainties in the measurements are relatively small. The comparison between predictions using the compressibility correction and the measurements is less satisfactory nearer to the jet exit. We suspect that the measurements are largely at fault in this region, due to problems of probes in supersonic flows. In particular, it is difficult to see how the potential core could only extend to x/d ca. 10 for Egger's (1966) measurements, while the jet studied by Seiner and

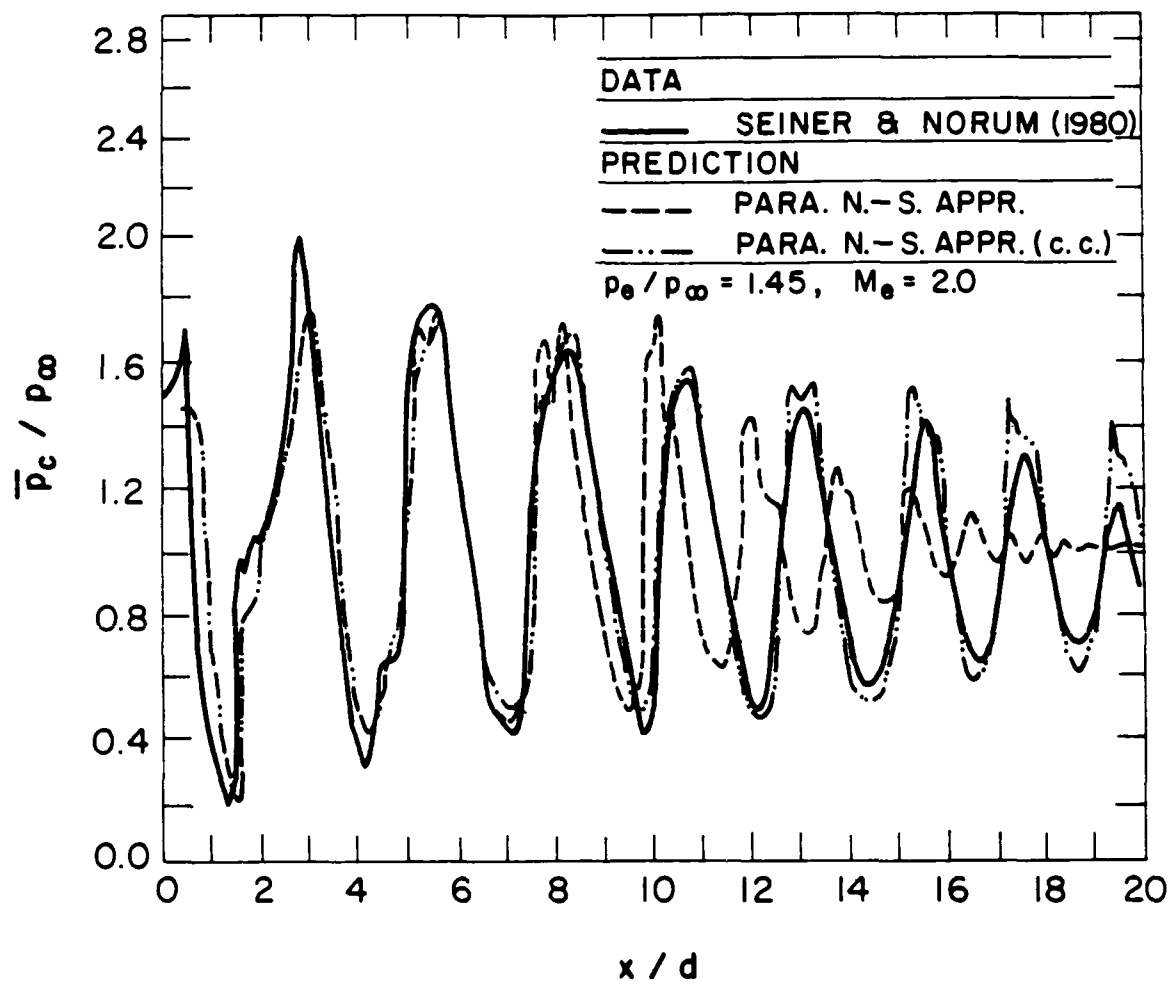


Fig. 32 Axial variation of mean static pressures in the under-expanded jet ($p_e / p_\infty = 1.45, M_e = 2.0$).

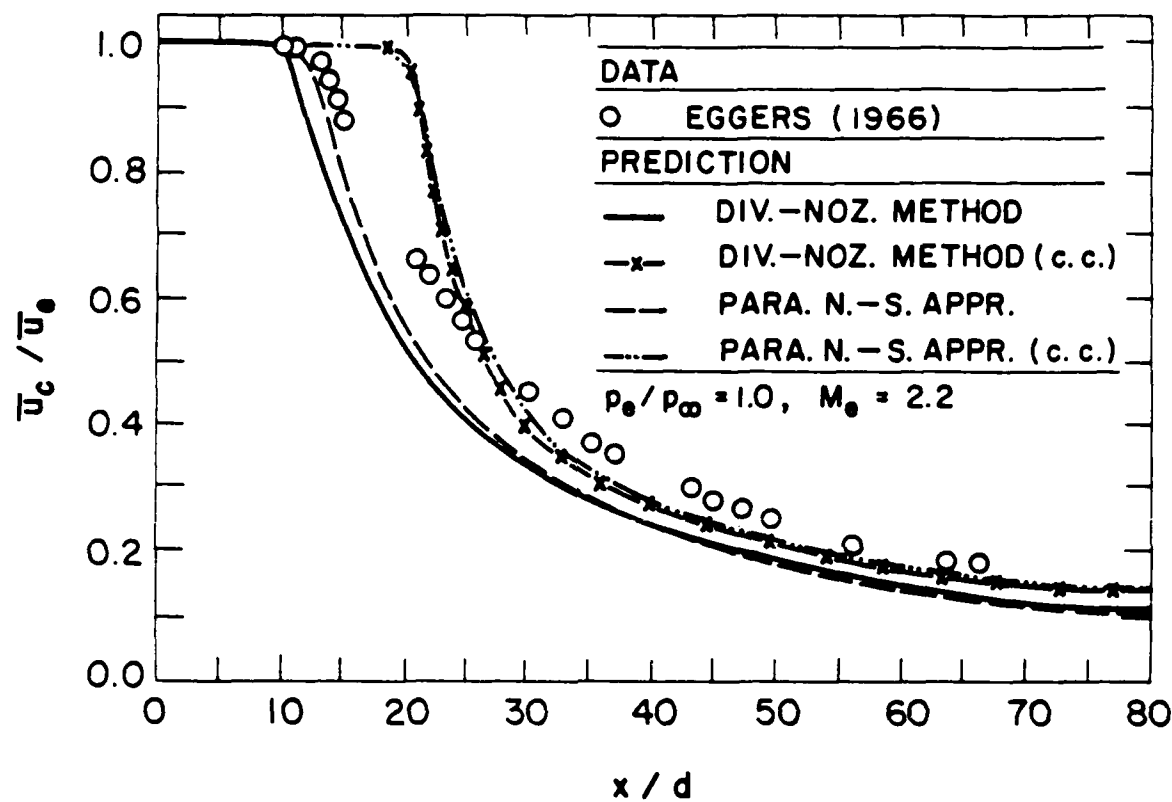


Fig. 33 Axial variation of mean velocities in an adapted supersonic jet ($p_e/p_\infty = 1.0, M_e = 2.2$).

Norum (1980), which has somewhat similar exit conditions, has a potential core greater than $x/d = 20$, see Fig. 32. These measurements should be repeated before drawing definitive conclusions concerning the value of the present compressibility correction for high-speed compressible mixing processes.

Considered together, these three evaluations suggest that both the diverging-nozzle and the parabolized Navier-Stokes methods, using the compressibility-corrected turbulence model, provide reasonably good predictions of flow properties for jets approximating slug-flow exit conditions. The baseline turbulence model without the compressibility correction, however, tends to overestimate mixing rates for convective Mach numbers greater than 0.6. These findings are in general agreement with Bogdanoff (1983) and Papamoschou and Roshko (1986), as exemplified by results appearing in Fig. 18.

5.4 Underexpanded Jets: Fully-Developed Flow

Initial Conditions. Measured initial conditions for the underexpanded jet (underexpansion ratio of 1.2) are illustrated in Fig. 34, along with the correlations for fully-developed pipe flow. Pressure variations begin quite close to the passage exit for the underexpanded jet, which complicates the interpretation of measured mean and fluctuating concentrations at $x/d = 0.2$; therefore, these measurements were not made since results for the adapted jets had already shown that concentrations were uniform at the passage exit. Similar to the adapted jets, mean and fluctuating streamwise velocities are similar to the correlation for fully-developed pipe flow within the core of the flow, but are broadened within the shear layer near the edge of the flow. For the underexpanded jet, however, the expansion wave emanating from the exit of the passage wall accelerates the gas near the edge of the flow, before mixing begins. This makes the streamwise velocity profile somewhat blunter than the fully-developed pipe flow correlation, and probably also plays a role in causing somewhat higher velocity fluctuations in the shear layer of the underexpanded jet than for the subsonic jet. Based on the measurements illustrated in Fig. 34, it was concluded that the flow at the passage exit was a reasonable approximation of fully-developed pipe flow with negligible concentration variations. These conditions were used to establish initial conditions for computations of flow properties for both underexpanded jets studied during this investigation. Profiles of mean velocities, turbulence kinetic energy, and the rate of dissipation of turbulence kinetic energy were obtained from Hinze (1975), while $\bar{f} = 1$ and $g = 0$, by definition.

Flow Visualization. Flow visualization for the weakly underexpanded jets was limited to Schlieren photographs, using a continuous light source. A continuous Schlieren photograph of the underexpanded jet having an underexpansion ratio of 1.2 appears in Fig. 35. The region near the jet exit is considered. Within this region, several oblique shock cells can be seen, similar to the pattern sketched in Fig. 2. With increasing distance from the jet exit, the

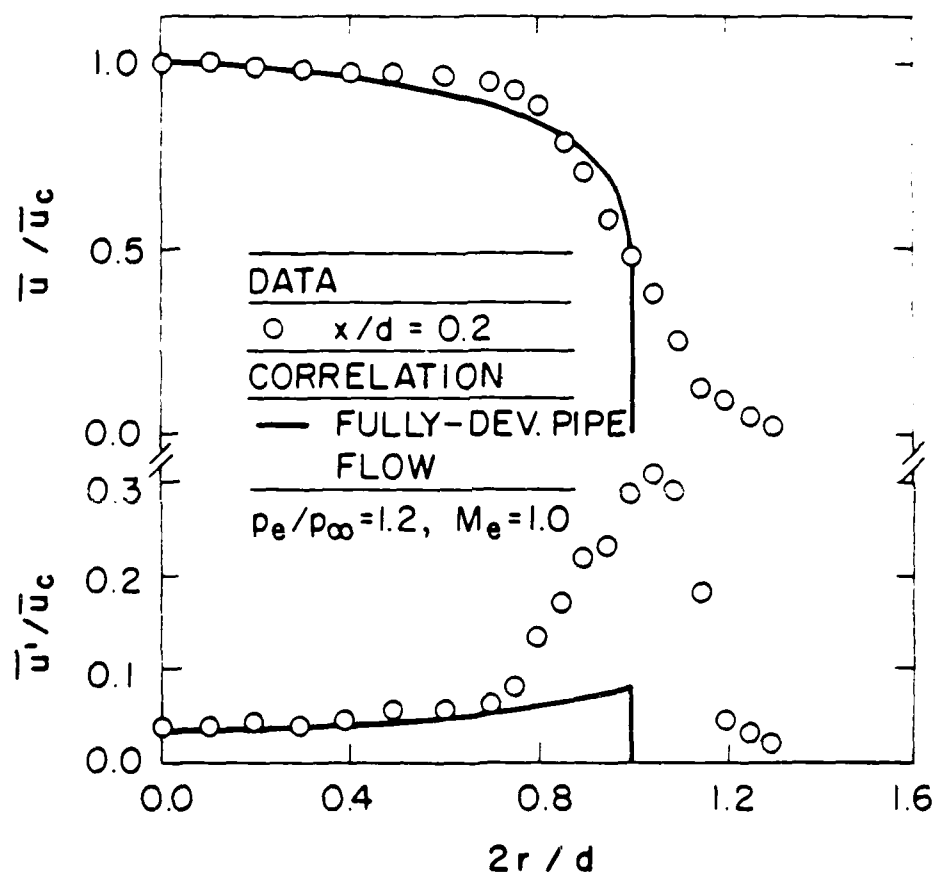


Fig. 54 The initial conditions for the underexpanded jet: radial profiles of mean and fluctuating velocities at $x/d = 0.2$.



Fig. 35 Continuous Schlieren photograph of near-field region of an underexpanded jet (underexpansion ratio of 1.2).

growth of the shear layer near the edge of the flow causes the shock cells to be increasingly restricted in the radial direction. This action of viscous effects eventually destroys the shock cell pattern, roughly 6-8 passage diameters from the jet exit. Viscous effects also cause the spacing between shock cells to decrease with increasing distance from the injector.

A Schlieren photograph of the underexpanded jet, having an underexpansion ratio of 1.4, is illustrated in Fig. 36. An oblique shock-cell pattern is seen, similar to the jet having a lower expansion ratio illustrated in Fig. 35. The main difference between the two flows is that the spacing of the shock cells increases as the underexpansion ratio increases. It is also clear that the spacing of the cells is not constant, but decreases gradually with increasing distance from the jet exit, until the flow becomes subsonic due to effects of viscosity and the shock-cell pattern disappears entirely.

Properties Along Axis. Predictions, using the SCIPVIS algorithm, and measurements of time-averaged mean static pressures along the axis for the sonic adapted jet (as a baseline) and for the two underexpanded jets, having underexpansion ratios of 1.20 and 1.37, are illustrated in Fig. 37. Normalized mean static pressure, \bar{p}_c/p_∞ is plotted as a function of normalized distance from the injector, x/d , considering the near-injector region, $x/d < 8$, where shock cells are present for the underexpanded jets.

Measurements for the adapted jet, illustrated in Fig. 37, should indicate a uniform static pressure field. Instead, there is a slight fluctuation of pressure, particularly near the passage exit. Although the pressure variation in this region is comparable to experimental uncertainties and cannot be used as a reliable measure of flow properties, the variation was reproducible and provides some additional evidence that the sonic adapted jet was actually somewhat underexpanded, ca., a few percent.

Static pressure measurements for the two underexpanded jets, illustrated in Fig. 37, clearly show an oscillatory pattern, which is expected based on the Schlieren photographs of the near-field regions of these jets, illustrated in Figs. 35 and 36. With increasing distance from the injector, the amplitude of the pressure oscillations decreases, and the wavelength decreases, until the shock cell structure is completely washed away by the growth of the shear layer near the edge of the jet. This process is completed by x/d in the range 6-7 for an underexpansion ratio of 1.20. The pressure field for an underexpansion ratio of 1.40 appears to be decaying in a similar manner; however, the full region of decay could not be measured. For $x/d > 4.5$, strong Mie scattering signals were observed along the axis and the measurements yielded anomalous results. This was felt to be due to condensation of either water or iodine vapor in the shear layer region, due to the lower static temperature levels of this flow.

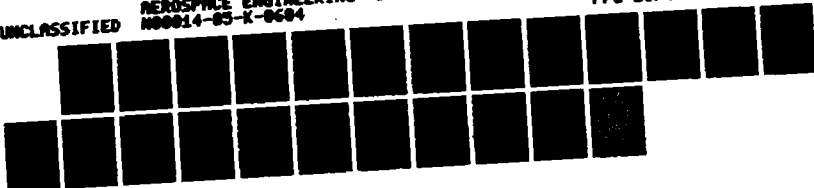


Fig. 36 Continuous Schlieren photograph
of an underexpanded jet

ND-AL90 036

UNCLASSIFIED

THE STRUCTURE OF SONIC UNDEREXPANDED TURBULENT AIR JETS 2/2
IN STILL AIR(U) MICHIGAN UNIV ANN ARBOR DEPT OF
AEROSPACE ENGINEERING S G CHUECH ET AL SEP 87
N00014-85-K-0684 F/G 28/4 ML



1·0

2·8

1

3·15
3·5
4·0
4·5

3·15

2·2

1·1

2·0

1·8

1·25

1·4

1·6

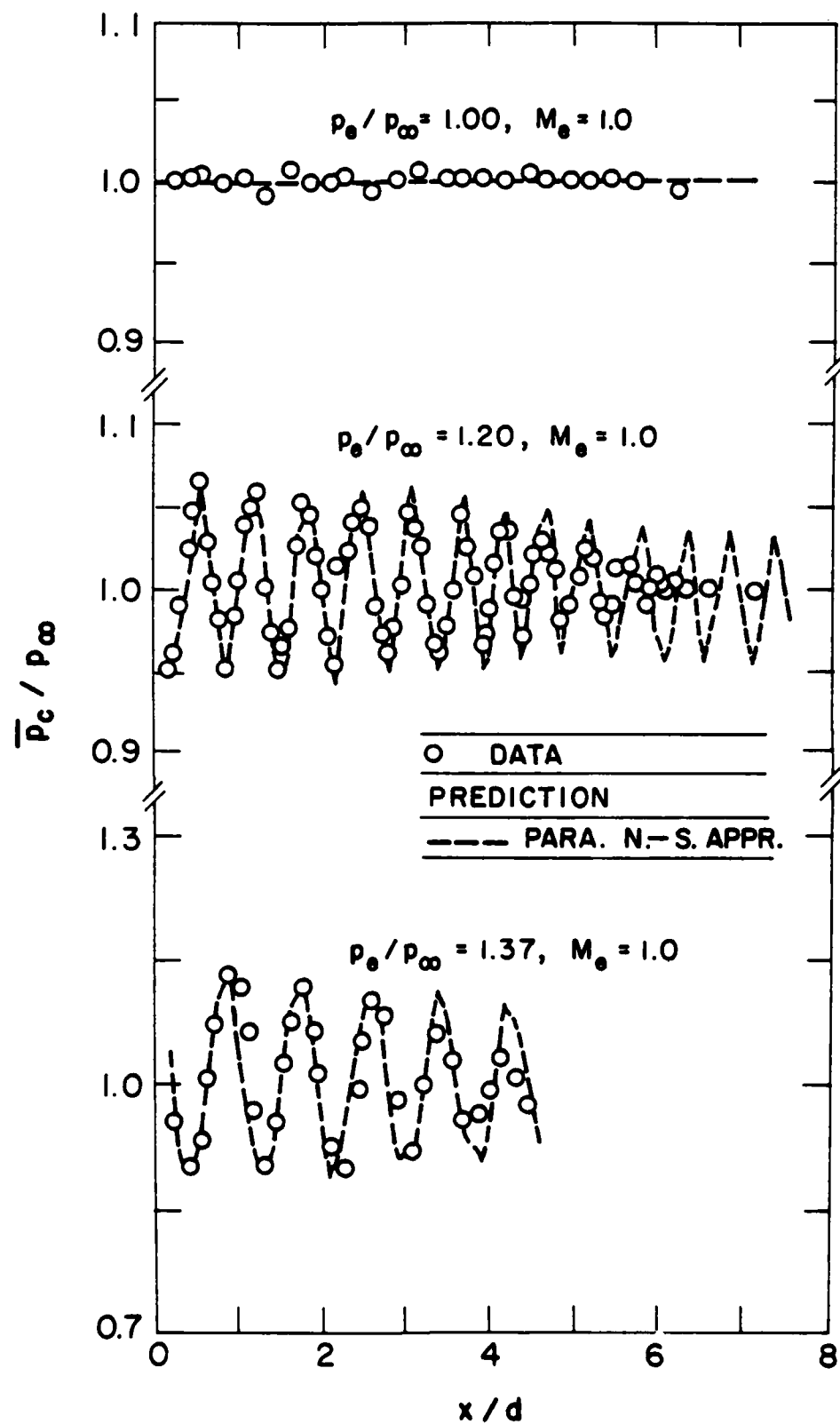


Fig. 37 Axial variation of mean static pressures in adapted and underexpanded jets.

Similar to the static pressure results for slug flow, illustrated in Fig. 32, predictions for fully-developed flow, illustrated in Fig. 37, are in reasonably good agreement with measurements for the first few shock cells, where effects of turbulent mixing are small. Farther downstream, however, predictions overestimate the amplitude and wavelength of the pressure oscillations, yielding a longer shock-wave-containing region than measured. This behavior is opposite to the findings for slug-flow jet exit conditions where the length of the shock-containing region was underestimated using the baseline turbulence model, cf. Figs. 32 and 37. The convective Mach numbers of the underexpanded fully-developed flows are less than 0.6; therefore, compressibility effects are small, so that both baseline and compressibility-corrected predictions are the same in Fig. 37. Thus, the presence of a fully turbulent core flow, as opposed to the inviscid flow prescribed by the SCIPVIS algorithm, is mainly responsible for this behavior, e.g., with an adjacent turbulent flow, the strong mixing layer near the edge of the flow grows more rapidly, causing faster decay of the shock-cell pattern. The same effect is responsible for the shorter length of the potential-core-like region for fully-developed jet exit conditions, than for slug flow, for low-speed jets.

Measured mean and fluctuating concentrations and streamwise velocities along the axis of the jet having an underexpansion ratio of 1.2 are illustrated in Fig. 38. Predictions using both SCIPVIS and the divergent-nozzle approximation are also illustrated on the figure. The length of the potential-core-like region for the underexpanded jet is similar to the sonic jet (cf. Figs. 27 and 38), which is somewhat surprising due to the vastly different core flow when shock cells are present. Measured mean velocities in the shock-containing region could not resolve the velocity changes across shock-cells due to deficiencies in particle response. Thus, only values beyond the potential-core-like region are reliable.

As expected from the static pressure results, predictions using SCIPVIS overestimate the length of the potential-core-like region. This behavior is not due to an inviscid effect, e.g., the shift in position of the sonic line between slug flow and fully-developed pipe flow jet exit conditions, since the SCIPVIS algorithm allows use of the actual initial mean velocity distribution at the jet exit. As noted earlier, faster growth of the strong mixing layer near the edge of the flow, due to the presence of the turbulent core, appears to be the most probable explanation for the differences between SCIPVIS predictions and measurements.

The predictions using the divergent-nozzle approximation are in best agreement with measurements in Fig. 38. Although the divergent-nozzle approach is somewhat ad hoc, it can account for effects of degree of flow development at jet exit and gave reasonably good results for other adapted and underexpanded jets. Thus, the improved agreement between the divergent-nozzle predictions and the measurements is supportive of the importance of turbulence at the jet exit on the near-field properties of underexpanded jets. More exact treatment of this process is very challenging, since the interaction between the strong mixing layer and the turbulent core, which have different turbulence properties, must be considered in the presence of shock waves and effects of compressibility.

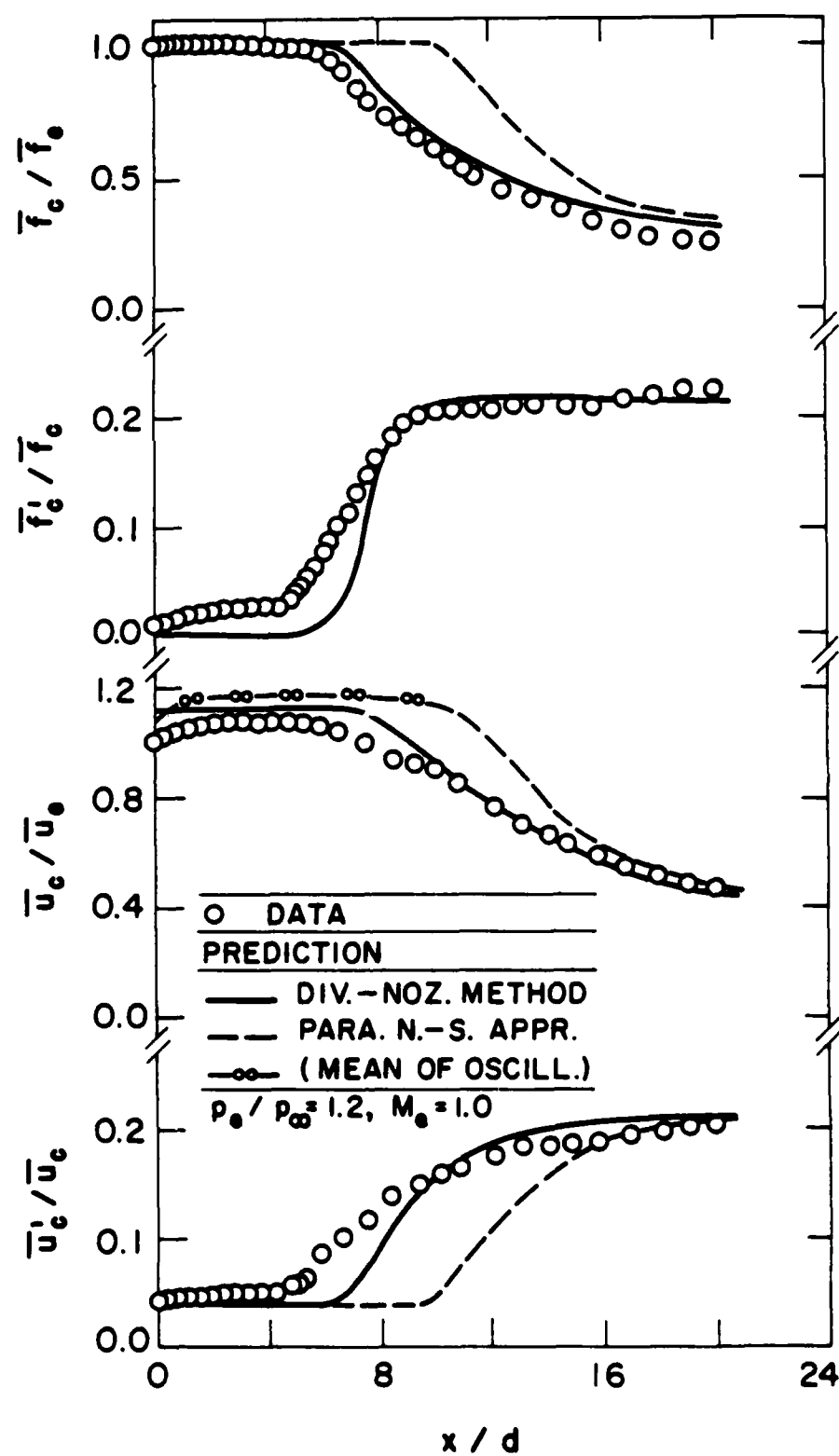


Fig. 38 Axial variation of mean and fluctuating quantities in the underexpanded jets.

Radial Profiles. The predicted and measured radial variation of flow properties in the underexpanded jet, having an underexpansion ratio of 1.2, are illustrated in Figs. 39-41, for $x/d = 5, 10$ and 20 . As in the case of the adapted jets, mean and fluctuating concentrations and streamwise velocity fluctuations are plotted as a function of r/x , which is the similarity variable for fully-developed turbulent jets. An exception for the measurements involves concentration measurements at $x/d = 5$: this profile was not measured since it is in the shock-cell region where static pressures vary, but static pressures were only found along the axis. Predictions shown on the figures include results from the SCIPVIS algorithm and use of the divergent-nozzle approximation. Similar to results along the axis, the divergent-nozzle, pseudo-diameter and momentum-velocity approximations gave nearly identical results for present test conditions. Results with and without the compressibility correction were essentially the same, due to the low convective Mach number of this flow.

In general, conclusions concerning the comparison between predictions and measurements for the radial profiles illustrated in Figs. 39-41, are similar to findings for properties along the axis, discussed in connection with Fig. 37. The SCIPVIS algorithm generally underestimates the rate of development of the flow, since this approach does not account for the presence of a turbulent core flow. In contrast, the approximate method, using equivalent jet exit conditions, yields surprisingly good results. This suggests that these methods might be helpful for analyzing some phenomena concerning the near-field region – particularly the region near the edge of the flow – where pressures are nearly equal to the ambient pressure. This would involve turbulent mixing processes with underexpanded jets, like condensing and reacting flows (Chen and Faeth, 1982, 1983; Birch et al., 1978, 1984, 1987).

Shock-Cell Parameters. Several shock-cell parameters were obtained from the continuous Schlieren photographs, over the range of conditions summarized in Table 3. This includes the standoff distance and diameter of the Mach disk and the average length of the shock cells. These measurements, and their comparison with predictions (where possible) are discussed in the following.

Predictions and measurements of Mach disk standoff distance and diameter are plotted as a function of underexpansion ratio in Fig. 42. In addition to present measurements, which pertain to fully-developed pipe flow at the passage exit, measurements of Addy (1981) and Ewan and Moodie (1986), which pertain to slug flow at the passage exit, are shown. Several predictions are also shown on the figure, as follows: estimates of Mach disk standoff distance and diameter from SCIPVIS, predictions of shock standoff distance due to Adamson and Nicholls (1959), an empirical correlation of Mach disk diameter due to Antsupov (1974), and a correlation of shock standoff distance due to Lamkin et al. (1980). All these predictions and correlations refer to slug flows having low levels of turbulence at the passage exit.

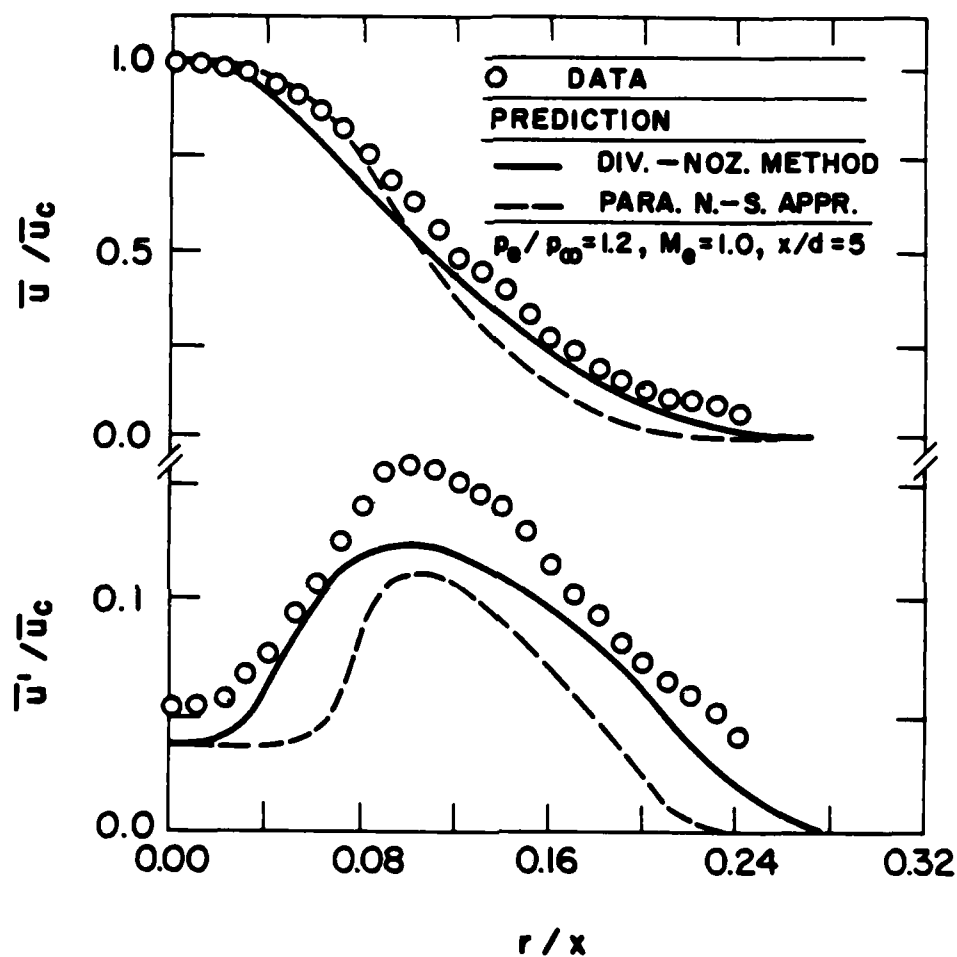


Fig. 39 Radial variation of mean and fluctuating velocities in the underexpanded jet at $x/d = 5$.

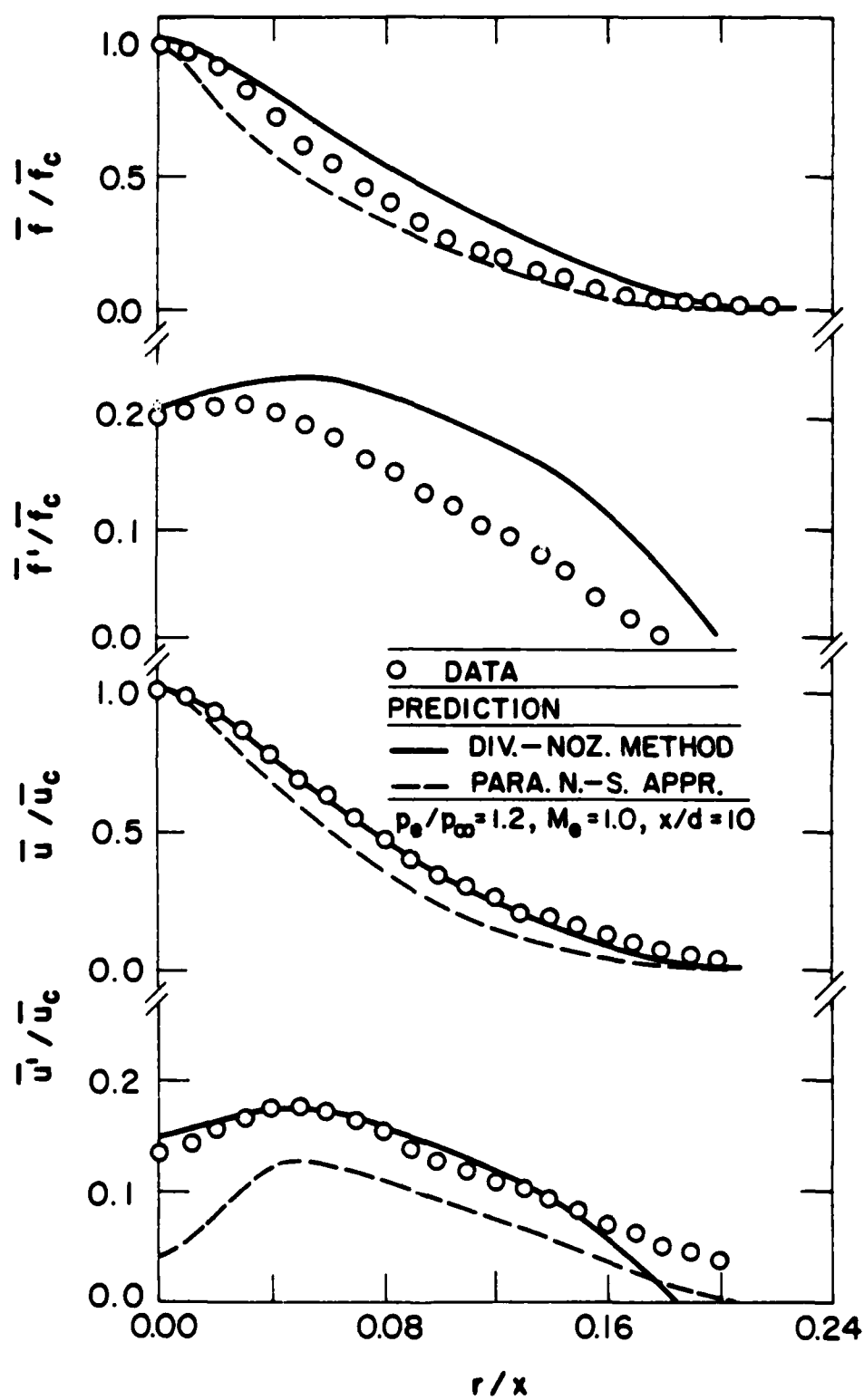


Fig. 40 Radial variation of mean and fluctuating quantities in the underexpanded jet at $x/d = 10$.

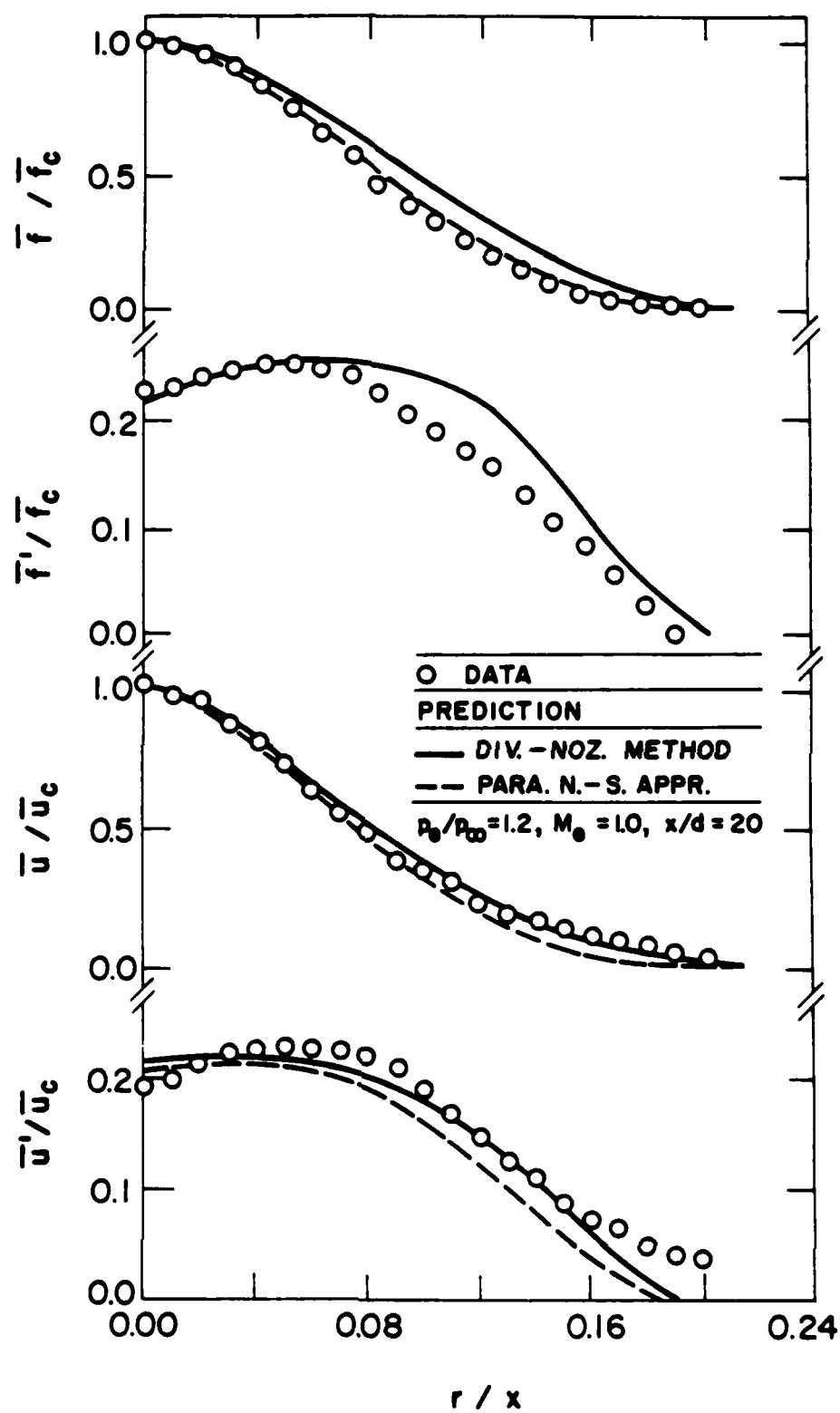


Fig. 41 Radial variation of mean and fluctuating quantities in the underexpanded jet at $x/d = 20$.

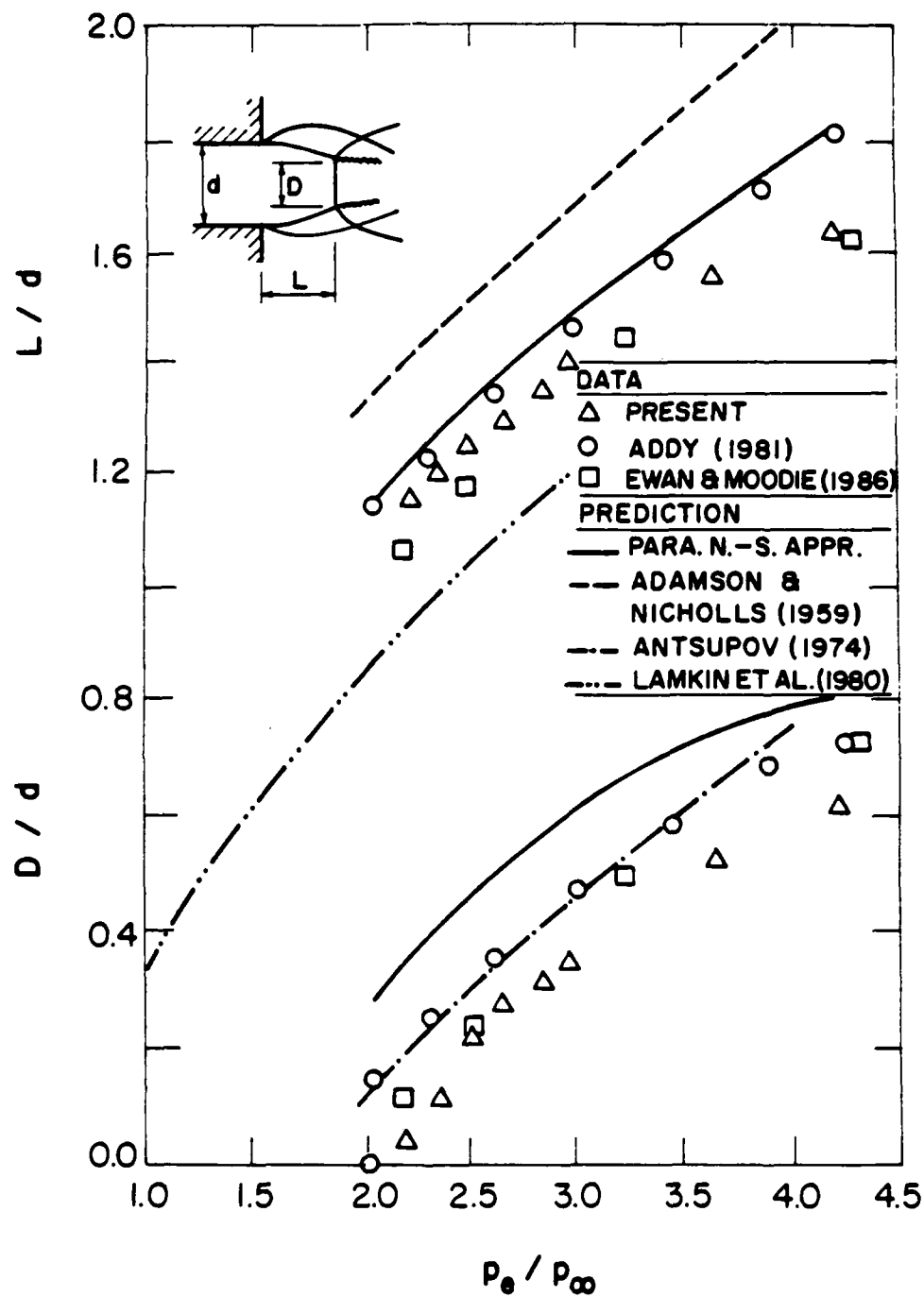


Fig. 42 Mach disk diameters and locations for sonic underexpanded jets.

The measurements illustrated in Fig. 42 show that the Mach disk is only present for underexpansion ratios greater than roughly two. This is indicated by the point where the Mach disk diameter becomes greater than zero, with all lower expansion ratios involving the intersection of oblique shocks. For a given underexpansion ratio, measurements show that the Mach disk standoff distance and diameter are somewhat smaller for fully-developed flow than for slug flow. From consideration of various nozzle geometries, but all for short nozzle passages, Addy (1981) has shown that shifts in the position and diameter of the Mach disk can partly be attributed to shifts in the position of the sonic line due to changes in the distribution of mean velocities at the passage exit. The present structure measurements, discussed in the last section, show that viscous effects and a turbulent core flow also contribute to shifts in the structure of the shock cells; therefore, these effects probably also play a role in the changes seen in Fig. 42. In particular, the more rapid growth of the shear layer near the edge of the jet constricts the shock-containing region, tending to reduce all the dimensions of the shock waves.

Predictions based on the SCIPVIS algorithm are based on the mean velocity distribution for fully-developed flow. Clearly, these predictions overestimate both the standoff distance and diameter of the Mach disk. Such behavior is expected, since SCIPVIS predictions do not properly represent the growth of the shear layer for turbulent flow at the exit of the passage. The predictions and correlations of Adamson and Nicholls (1959), Antsupov (1974) and Lamkin et al. (1980) provide qualitative estimates of the standoff distance and diameter, but do not consider effects of varying mean velocity distributions and turbulence properties at the passage exit; therefore, these methods do not provide very accurate estimates of any of the measured properties illustrated in Fig. 42.

The spacing of the shock cells in the near-field region varies with distance along the axis. However, an average spacing, S , was defined in order to quantify the effect of the underexpansion ratio on the overall appearance of the shock cell pattern. These measurements are illustrated in Fig. 43, along with predictions obtained using the SCIPVIS algorithm.

At underexpansion ratios near unity, the shock waves are oblique and cross the field nearly perpendicular to the axis; therefore, the shock-cell spacing becomes small. As the underexpansion ratio increases, the spacing increases but tends to approach a finite limit, since the shock cells are confined by the rapidly growing shear layer which constricts their dimensions, as noted earlier. The appearance of the Mach disk, at underexpansion ratios near two, has a dramatic influence on the appearance of the flow field; however, this event does not cause an appreciable change in the rate of growth of the shock cell spacing illustrated in Fig. 43. Nevertheless, the general growth of the average spacing tends to parallel the growth of the Mach disk diameter and standoff distances, pictured in Fig. 42, for underexpansion ratios greater than two. Similar to the behavior of the SCIPVIS predictions for Mach disk diameter and standoff distance, the SCIPVIS algorithm tends to overestimate the shock cell spacing. This behavior follows since the growth of the shear layer is underestimated, which provides

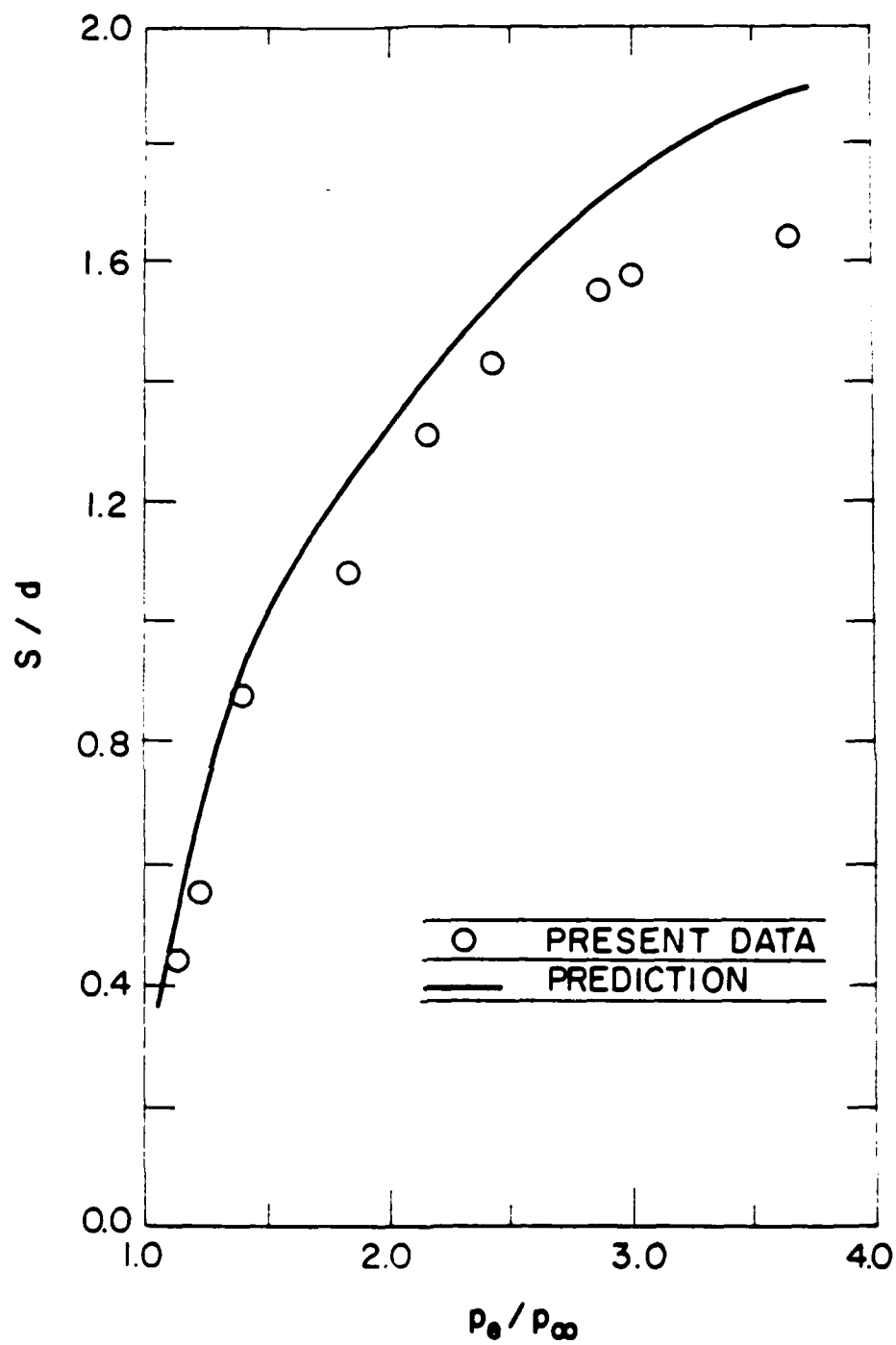


Fig. 45 Shock-cell wavelength for sonic underexpanded jets.

more room for the shock cells than is actually observed when the core flow is turbulent.

6. CONCLUSIONS

The major conclusions of the present study are as follows:

1. The shock-wave-containing near-field region of underexpanded turbulent jets is influenced by effects of both compressibility, and turbulence levels at the jet exit. Large convective Mach numbers (greater than 0.5) tend to reduce mixing rates due to compressibility effects, as described by Bogdanoff (1983) and Papamoschou and Roshko (1986), which increases the extent of the shock containing region. Conversely, high turbulence levels at the jet exit tend to increase mixing rates, similar to subsonic jets, which reduces the extent of the shock-containing region. The interaction between the multiplicity of turbulence scales in the turbulent core and the shear layer, and their relationship to the large eddies which are responsible for mixing in shear layers, presents a formidable problem which must be resolved to obtain a better understanding of underexpanded turbulent jets.
2. Use of the divergent-nozzle approximation, in conjunction with the compressibility-corrected $k-\epsilon$ turbulence model, was reasonably successful for estimating the structure of adapted jets and the constant-pressure portions of underexpanded jets (for both fully-developed and slug flow jet exit conditions). Unfortunately, this approach provides no information concerning the near-field shock-wave-containing region of the flow.
3. The parabolized Navier-Stokes approach, using the SCIPVIS algorithm and the compressibility-corrected turbulence model, was reasonably successful for slug flows at the jet exit. Additional development of this approach is needed so that effects of turbulence at the jet exit, which are important for some applications, can be accommodated.
4. The present compressibility-correction yielded encouraging results; however, it is provisional and only limited data were available to calibrate the approach. Additional measurements, involving high convective Mach numbers, are needed for a more definitive evaluation.
5. Present LIF methods provide a convenient means of measuring mean and fluctuating concentrations and mean static pressures for supersonic flows near atmospheric pressure, complementing earlier proposals for the use of LIF for pressure measurements at low pressures due to McDaniel (1983). The main

problem encountered during the present work was evidence of condensation of water vapor or iodine vapor at high underexpansion ratios. In agreement with earlier studies, it was found that conventional LDA, using seeding particles, is not satisfactory in the supersonic portions of underexpanded jets, due to the inability of particles to respond to the rapid gas velocity changes across shock waves.

Present measurements were limited to modest underexpansion ratios and fully-developed jet exit conditions. Additional measurements are needed, as follows: slug flows should be considered, to provide direct experimental evidence concerning effects of flow development; higher underexpansion ratios (greater than two) should be considered, to find the effect of the appearance of a Mach disk on flow structure and mixing properties; and high-speed adapted jets, having various turbulence levels at the jet exit, should be considered, to highlight the combined effects of compressibility and adjacent turbulent flows on near-field mixing properties. Such results would be most helpful for developing methods for predicting the structure of turbulent underexpanded jets. Work along these lines is currently in progress in this laboratory.

REFERENCES

- Abbett, M. (1971) Mach disk in underexpanded exhaust plumes. AIAA J. 9, 512-514.
- Adamson, T. C. Jr. and Nicholls, J. A. (1959) On the structure of jets from highly underexpanded jets in still air. J. Aero. Sci. 26, 16-24.
- Addy, A. L. (1981) Effects of axisymmetric sonic nozzle geometry on Mach disk characteristics. AIAA J. 19, 121-122.
- Anderson, J. D. Jr. (1984) A survey of modern research in hypersonic aerodynamics. AIAA Paper No. 84-1578.
- Antonia, R. A., Prabhu, A. and Stephenson, S. E. (1975) Conditionally sampled measurements in a heated turbulent jet. J. Fluid Mech. 72, 455-480.
- Antsupov, A. V. (1974) Properties of underexpanded and overexpanded supersonic gas jets. Sov. Phys. Tech. 19, 2.
- Becker, H. A., Hottel, H. C. and Williams, G. C. (1967) The nozzle-fluid concentration field of the round, turbulent, free jet. J. Fluid Mech. 30, 285-303.

- Bilger, R. W. (1976) Turbulent jet diffusion flames. Prog. Energy Combust. Sci. 1, 87-109.
- Birch, A. D., Brown, D. R., Dodson, M. G. and Thomason, J. R. (1978) The turbulent concentration field of a methane jet. J. Fluid Mech. 88, 431-449.
- Birch, A. D., Brown, D. R., Dodson, M. G. and Swaffield, F. (1984) The structure and concentration decay of high pressure jets of natural gas. Comb. Sci. Tech. 36, 249-261.
- Birch, A. D., Hughes, D. J. and Swaffield, F. (1987) Velocity decay of high pressure jets. Comb. Sci. Tech. 52, 161-171.
- Birch, S. F. and Eggers, J. M. (1973) A critical review of the experimental data for developed free turbulent shear layers. Free Turbulent Shear Layers 1, NASA SP 321, 11-40.
- Bogdanoff, D. W. (1983) Compressibility effects in turbulent shear layers. AIAA J. 21, 926-927.
- Brown, G. L. and Roshko, A. (1974) On density effects and large structures in turbulent mixing layers. J. Fluid Mech. 64, 775-816.
- Chen, L.-D. and Faeth, G. M. (1982) Condensation of submerged vapor jets in subcooled liquids. J. Heat Transfer 104, 774-780.
- Chen, L.-D. and Faeth, G. M. (1983) Structure of turbulent reacting gas jets submerged in liquid metals. Comb. Sci. Tech. 31, 277-296.
- Chuech, S. G. (1987) Kinematic and scalar structure of turbulent underexpanded sonic jets. Ph.D. Thesis, The Pennsylvania State University, University Park, Pennsylvania.
- Corrsin, S. and Uberoi, M. S. (1949) Further experiments on the flow and heat transfer in a heated turbulent air jet. NACA TN 1865.
- Corrsin, S. and Uberoi, M. S. (1950) Further experiments on the flow and heat transfer in a heated turbulent air jet. NACA Report 998.
- Corrsin, S. and Uberoi, M. S. (1951) Spectrum and diffusion in a round turbulent jet. NACA TR 1040.

- Crist, S., Sherman, P. M. and Glass, D. R. (1966) Study of the highly underexpanded sonic jet. AIAA J. 4, 68-71.
- Dash, S. M., Weilerstein, G. and Vaglio-Laurin, R. (1975) Compressibility effects in free turbulent shear flows. Report No. AFOSR-TR-75-1436.
- Dash, S. M. and Thorpe, R. D. (1980) Shock-capturing model for one- and two-phase supersonic exhaust flow. AIAA J. 19, 842-851.
- Dash, S. M., Wilmoth, R. G. and Pergament, H. S. (1978) Overlaid viscous/inviscid model for the prediction of near field jet entrainment. AIAA J. 17, 950-958.
- Dash, S. M. and Wolf, D. E. (1984) Interactive phenomena in supersonic jet mixing problems, part I: phenomenology and numerical modeling techniques. AIAA J. 22, 905-913.
- Dash, S. M. and Wolf, D. E. (1984a) Interactive phenomena in supersonic jet mixing problems, part II: numerical studies. AIAA J. 22, 1395-1404.
- Dash, S. M. and Wolf, D. E. (1984b) Fully-coupled analysis of jet mixing problems, Part I: shock-capturing model, SCIPVIS. NASA Contractor Report 3761.
- Dash, S. M., Wolf, D. E. and Seiner, J. M. (1985) Analysis of turbulent underexpanded jets, Part I: parabolized Navier-Stokes model, SCIPVIS. AIAA J. 23, 505-514.
- Dash, S. M., Wolf, D. E. and Sinha, N. (1986) Parabolized Navier-Stokes analysis of three-dimensional supersonic and subsonic jet mixing problems. AIAA J. 24, 1252-1253.
- Davidor, W. and Penner, S. S. (1971) Shock standoff distances and Mach-disk diameters in underexpanded sonic jets. AIAA J. 9, 1651-1653.
- Drake, M. C., Lapp, M., Penny, C. M., Warshaw, S. and Gerhold, B. W. (1981) Measurements of temperature and concentration fluctuations in turbulent diffusion flames using pulsed Raman spectroscopy. Eighteenth Symposium (International) on Combustion, The Combustion Institute, Pittsburgh, PA, 1521-1531.
- Dyer, T. M. (1979) Rayleigh scattering measurements of time-resolved concentration in a turbulent propane jet. AIAA J. 17, 912-914.

- Eggers, J. M. (1966) Velocity profiles and eddy viscosity distributions downstream of a Mach 2.22 nozzle exhausting to quiescent air. NASA TN D-3601.
- Escoda, M. C. and Long, M. B. (1983) Rayleigh scattering measurements of the gas concentration field in turbulent jets. AIAA J. 21, 81-84.
- Ewan, B.C.R. and Moodie, K. (1986) Structure and velocity measurements in underexpanded jets. Comb. Sci. Tech. 45, 275-288.
- Faeth, G. M. (1983) Evaporation and combustion of sprays. Prog. Energy Combust. Sci. 9, 1-76.
- Field, M. A., Gill, D. W., Morgan, B. and Hawksley, P.G.C. (1967) Combustion of pulverised coal. British Coal Utilization Research Association, Leatherhead, England.
- Flack, R. D., Jr. and Thompson, H. D. (1977) Some laser velocimeter measurements in the turbulent wake of a supersonic jet. AIAA J. 15, 1507-1509.
- Fletcher, D. G. and McDaniel, J. C. (1987) Temperature measurement in a compressible flow field using laser-induced iodine fluorescence. Optics Letters 11, 16-18.
- Fletcher, D. G. and McDaniel, J. C. (1987a) Quantitative measurement of transverse injector and free stream interaction in a nonreacting scramjet combustor using laser-induced iodine fluorescence. AIAA Paper No. 87-0087.
- Forstall, W., Jr. and Shapiro, A. H. (1950) Momentum and mass transfer in coaxial gas jets. J. Appl. Mech. 17, 399-408.
- Gore, J. P., Faeth, G. M., Evans, D. and Pfenning, D. B. (1986) Structure and radiation properties of large-scale natural gas/air diffusion flames. Fire and Materials, 10, 161-169.
- Graham, S. C., Grant, A. J. and Jones, J. M. (1974) Transient molecular concentration measurements in turbulent flows using Rayleigh light scattering. AIAA J. 12, 1140-1142.
- Gross, K. P. and McKenzie, R. L. (1985) Measurements of fluctuating temperature in a supersonic turbulent flow using laser-induced fluorescence. AIAA J. 23, 1932-1936.

- Gustafson, E. K., McDaniel, J. C. and Byer, R. L. (1981) CARS measurement of velocity in a supersonic jet. IEEE J. Quantum Electr. QE-17, 12, 2258-2259.
- Hess, K., Leuckel, W. and Stoeckel, A. (1973) Formation of explosive clouds of gas on overhead release, and preventive measures. Chemie-Ing. Tech. 45, 323.
- Hiller, B., Cohen, L. M. and Hanson, R. K. (1986) Simultaneous measurements of velocity and pressure fields in subsonic and supersonic flows through image-intensified detection of laser-induced fluorescence. AIAA Paper No. 86-0161.
- Hinze, J. O. (1975) Turbulence, Second Edition, McGraw-Hill, New York, 286-300, 715-742.
- Huffaker, R. M., Fuller, C. E. and Lawrence, L. R. (1969) Application of laser Doppler velocity instrumentation to the measurement of jet turbulence. S.A.E. Conference, Detroit, MI, Paper No. 690266.
- Ikawa, H. and Kubota, T. (1975) Investigation of a supersonic turbulent mixing layer with zero pressure gradient. AIAA J. 13, 566-572.
- Jeng, S.-M. and Faeth, G. M. (1984) Species concentrations and turbulence properties in buoyant methane diffusion flames. J. Heat Transfer 106, 721-727.
- Kalghati, G. T. (1981) Blow-out stability of gaseous jet diffusion flames, part I: in still air. Comb. Sci. Tech. 26, 233-239.
- Kalghati, G. T. (1984) Lift-off heights and visible lengths of vertical turbulent jet diffusion flames in still air. Comb. Sci. Tech. 41, 17-29.
- Kline, S. J. and McClintock, F. A. (1953) The description of uncertainties in single sample experiments. Mechanical Engineering 75, 3-9.
- Kotsovinos, N. E. (1975) A study of the entrainment and turbulence in a plane buoyant jet. Ph.D. Thesis, California Institute of Technology, Pasadena, CA.
- Kreid, D. K. (1974) Laser-Doppler velocimeter measurements in nonuniform flow: error estimates. Applied Optics 13, 1872-1881.
- Lai, M.-C. and Faeth, G. M. (1987) A combined laser-Doppler anemometer/laser-induced fluorescence system for turbulent transport measurements. J. Heat Transfer, 109, 254-256.

- Lai, M.-C., Jeng, S.-M. and Faeth, G. M. (1985) Structure of turbulent adiabatic wall plumes. J. Heat Transfer 108, 951-959.
- Lamkin, D. E., Koestel, A., Gido, R. G. and Baranowsky, P. W. (1980) Containment main streamline break analysis for equipment qualification. NUREG/CR-1511, LA-8305-MS.
- Lapp, M. (1974) Flame temperatures from vibrational Raman scattering. Laser Raman Gas Diagnostics, edited by M. Lapp and C. M. Penny, Plenum Press, New York, p. 107.
- Lau, J. C. (1980) Mach number and temperature effects on jets. AIAA J. 18, 609-610.
- Lau, J. C. (1981) Effects of exit Mach number and temperature on mean-flow and turbulence characteristics in round jets. J. Fluid Mech. 105, 193-218.
- Lau, J. C., Morris, P. C. and Fisher, M. J. (1979) Measurements in subsonic and supersonic free jets using a laser velocimeter. J. Fluid Mech. 93, 1-27.
- Launder, B. E., Morse, A., Rodi, W. and Spalding, D. B. (1972) Prediction of free shear flows: a comparison of six turbulence models. Free Turbulent Shear Flows, Vol. I, NASA SP-321, 361-426.
- Lewis, C. H., Jr. and Carlson, D. J. (1964) Normal shock location in underexpanded gas and gas-particle jets. AIAA J. 2, 776-777.
- Lockwood, F. C. and Naguib, A. S. (1975) The prediction of the fluctuations in the properties of free, round jet, turbulent diffusion flames. Combustion and Flame 24, 109-124.
- Long, V. D. (1963) Estimation of the extent of hazardous areas around a vent. Second Symposium on Chemical Process Hazards, 6-14.
- Maydew, R. C. and Reed, G. F. (1963) Turbulent mixing of compressible free jets. AIAA J. 1, 1443-1444.
- McDaniel, J. C. (1983) Nonintrusive pressure measurement with laser-induced iodine fluorescence. AIAA Paper 83-1468.
- McDaniel, J. C. (1983a) Quantitative measurement of density and velocity in compressible flows using laser-induced iodine fluorescence. AIAA Paper No. 83-0049.

- McDaniel, J. C., Baganoff, D. and Byer, R. L. (1982) Density measurement in compressible flows using off-resonant laser-induced fluorescence. Phys. Fluids 25, 1165-1107.
- McDaniel, J. C. Hiller, B. and Hanson, R. K. (1983) Simultaneous multiple-point velocity measurements using laser-induced fluorescence. Optics Letters 8, 51-53.
- Mikhail, A. G., Hankey, W. L. and Shang, J. S. (1980) Computation of a supersonic flow past an axisymmetric nozzle boat-tail with jet exhaust. AIAA J. 18, 869-875.
- Papamoschou, D. and Roshko, A. (1986) Observation of supersonic free shear layers. AIAA Paper No. 86-0162.
- Pitts, W. M. and Kashiwagi, T. (1984) The application of laser-induced Rayleigh light scattering to the study of turbulent mixing. J. Fluid Mech. 141, 391-429.
- Ribeiro, M. M. and Whitelaw, J. H. (1974) Statistical characteristics of a turbulent jet. Imperial College of Science and Technology Report No. HTS/74119.
- Robben, F. (1975) Comparison of density and temperature measurements using Raman scattering and Rayleigh scattering in combustion measurements in jet propulsion systems. (R. Goulard, ed.) Proceedings of a Project SQUID Workshop, Purdue University, W. Lafayette, Indiana, 179-195.
- Robinson, C. E., Roux, J. A. and Bertrand, W. T. (1979) Infrared measurements in an exhaust plume from an axisymmetric afterbody model at transonic Mach number. AEDC-TR-78-55.
- Rodi, W. (1972) The prediction of free turbulent boundary layers by use of a two-equation model of turbulence, Ph.D. Thesis, University of London, London, England.
- Rosensweig, R. E., Hottel, H. C. and Williams, G. C. (1961) Smoke-scattered light measurement of turbulent concentration fluctuations. Chem. Engng. Sci. 15, 111-129.
- Schefer, R. W. and Dibble, R. W. (1986) Rayleigh scattering measurements of mixture fraction in a turbulent nonreacting propane jet. AIAA Paper No. 86-0278.
- Schlichting, H. (1979) Boundary Layer Theory, McGraw-Hill, New York, 599.

- Seiner, J. M., Dash, S. M. and Wolf, D. E. (1985) Analysis of turbulent underexpanded jets, part II: Shock noise features using SCIPVIS. AIAA J. 23, 669-677.
- Seiner, J. M. and Norum, T. D. (1979) Experiments of shock associated noise on supersonic jets. AIAA Paper No. 79-1526.
- Seiner, J. M. and Norum, T. D. (1980) Aerodynamic aspects of shock containing jet plumes. AIAA Paper No. 80-0965.
- Shapiro, A. H. (1954) Compressible Fluid Flow, Vol. I, Ronald Press, New York, 454-455.
- Shaughnessy, E. J. and Morton, J. B. (1977) Laser light-scattering measurements of a particle concentration in a turbulent jet. J. Fluid Mech. 80, 129-148.
- Shuen, J.-S., Chen, L.-D. and Faeth, G. M. (1983a) Predictions of the structure of turbulent, particle-laden, round jets. AIAA J. 21, 1480-1483.
- Shuen, J.-S., Solomon, A.S.P., Zhang, Q.-F. and Faeth, G. M. (1984) Structure of particle-laden jets: Measurements and predictions. AIAA J. 23, 396-404.
- Sindir, M. M. and Harsha, P. T. (1984) Turbulent transport models for scramjet flowfields. NASA CR-17284.
- Sirieux, M. and Solignac, J.-L. (1966) Contribution a l'etude experementale de la couche de melange turbulent isobare d'un ecoulement supersonique. Symposium on Separated Flow, AGARD Conference Proceedings, No. 4, Pt.1, 241-270.
- Smith, J. R. and Giedt, W. (1974) Flow field temperature distribution determination using rotational Raman spectroscopy. Proceedings of the Fifth International Heat Transfer Conference, Tokyo, Japan, September.
- Spalding, D. B. (1971) Concentration fluctuations in a round turbulent free jet. Chem. Engrg. Sci. 26, 95-107.
- Spalding, D. B. (1977) GENMIX: A General Computer Program for Two-Dimensional Parabolic Phenomena. Pergamon Press, Oxford.

- Sun, T.-Y. and Faeth, G. M. (1986) Structure of turbulent bubbly jets: I. Methods and centerline properties; II. Phase property profiles. Int. J. Multiphase Flow 12, 99-126.
- Vatsa, V. N., Werle, M. J. and Anderson, O. L. (1981) Solution of slightly underexpanded two-dimensional and axisymmetric coflowing jets. AIAA J. 19, 303-310.
- Vatsa, V. N., Werle, M. J., Anderson, O. L. and Hankins, G. B. (1982) Solutions for three-dimensional over- or underexpanded exhaust plumes. AIAA J. 20, 1188-1194.
- Wynanski, I. and Fiedler, H. (1969) Some measurements in the self-preserving jet. J. Fluid Mech. 38, 577-612.
- Yee, D., Malte, P. C. and Kamber, P. D. (1983) Mixing in jet flames by laser Rayleigh scattering. AIAA Paper No. 83-0403.
- Zucrow, M. J. and Hoffman, J. D. (1976) Gas Dynamics: Volume I, John Wiley & Sons, Inc., New York, 218-219.

**ONR REPORT DISTRIBUTION LIST: CLOSED, LIQUID
METAL COMBUSTION***

Dr. Gabriel D. Roy (2)
Mechanics Division, Code 1132 P
Office of Naval Research
800 N. Quincy Street
Arlington, VA 22217-5000

Dr. Richard S. Miller (2)
Mechanics Division, Code 1132P
Office of Naval Research
800 N. Quincy Street
Arlington, VA 22217-5000

Dr. Lynn A. Parnell
Naval Ocean System Center
Code 6341
San Diego, CA 92152-5000

Defense Documentation Center (12)
Building 5, Cameron Station
Alexandria, VA 22314

Technical Information Division (6)
Naval Research Laboratory
4555 Overlook Avenue SW
Washington, DC 20375

Dr. Jerry A. Smith
Chemistry Division
Office of Naval Research
800 N. Quincy Street
Arlington, VA 22217

Dr. Albert D. Wood
Technology Programs
Office of Naval Research
800 N. Quincy St.
Arlington, VA 22217

Dr. H.W. Carhart
Combustion & Fuels
Naval REsearch Laboratory
Washington, DC 20375

Professor Allen Fuhs
Department of Aeronautics
Naval Post Graduate School
Monterey, CA 93943

Division Director
Engineering and Weapons
US Naval Academy
Annapolis, MD 21402

Mr. Francis J. Romano
Code 63R3
Naval Sea Systems Command
Washington, DC 20363

Mr. Norman D. Hubele
Fluidic Systems, MS 1301-RR
Garrett Pneumatic Systems Division
2801 East Washington St.
Phoenix, AZ 85034

Dr. Hugh H. Darsie
Advanced Technology Group
Substrand Energy Systems
4747 Harrison Avenue
Rockford, IL 61101

Dr. Daniel H. Kiely
Power & Energy Group
The Pennsylvania State University
Applied Research Laboratory
P.O. Box 30
State College, PA 16801

Professor Darryl E. Metzger
Department of Mechanical and
Aerospace Engineering
Arizona State University
Tempe, AZ 85281

Dr. Dae H. Cho
Reactor Analysis & Safety Division
Argonne National Laboratory
Argonne, IL 60439

Professor S.H. Chan
Department of Mechanical Engineering
The University of Wisconsin-Milwaukee
P.O. Box 784
Milwaukee, WI 53201

* One copy except as noted in parenthesis.

Professor George A. Brown
Department of Mechanical Engineering
and Applied Mechanics
University of Rhode Island
Kingston, RI 02881

Professor A. Murty Kanury
Department of Mechanical Engineering
Oregon State University
Corvallis, OR 97331

Professor Irvin Glassman
Department of Mechanical and
Aerospace Engineering
Engineering Quadrangle
Princeton University
Princeton, NY 08544

Professor Norman Chigier
Department of Mechanical Engineering
Carnegie-Mellon University
Pittsburgh, PA 15213

Professor George Janz
Cogswell Laboratory, R306
Department of Chemistry
Rensselaer Polytechnic Institute
Troy, NY 12181

Dr. Leonard Leibowitz
Chemical Technology Division
Argonne National Laboratory
9700 South Case Avenue
Argonne, IL 60439

Professor John Tarbell
104 Fenske Laboratory
Pennsylvania State University
University Park, PA 16801

Professor Thomas E. Daubert
104 Fenske Laboratory
Pennsylvania State University
University State Park, PA 16801

Dr. J. Braunstein
Research Division
Oak Ridge Operations
Department E
Oak Ridge, TN 37831

Mr. Robert Tompkins
Code 36621, Bldg. 126T
Naval Underwater Systems Center
Newport, RI 02841

Mr. Maurice F. Murphy
Code R33, Room 4-1711
Naval Surface Weapons, White Oak
Silver Spring, MD 20910

Dr. Kurt Mueller
Code R10
Energetic Materials Division
Naval Surface Weapons Center,
White Oak
Silver Spring, MD 20910

Dr. Earl Quandt, Jr.
Code 2704
David Taylor Naval Ship
Research and Development Center
Annapolis, MD 21402

Mr. Richard Bloomquist
Code 2752
David Taylor Naval Ship R&D Center
Annapolis, MD 21402

Dr. Lawrence P. Cook
High Temperature Processes Group
National Bureau of Standards
Washington, DC 20234

Dr. W. Lee
Research and Technology Department
Naval Surface Weapons Center
Silver Springs, MD 20703

END

DATE

FILMED

5-88

DTIC